

**DIGITAL SIGNAL ANALYSIS FOR DETECTION OF AIR BUBBLES ON
ARTIFICIAL THIGH VESSELS**

by

Andrés Saavedra Ruiz

A thesis submitted in partial fulfillment of the requirements for the degree of

MASTER OF SCIENCE

in

ELECTRICAL ENGINEERING

UNIVERSITY OF PUERTO RICO

MAYAGÜEZ CAMPUS

2015

Approved by:

Lizdabel Morales, PhD
Member, Graduate Committee

Date

Silvina Cancelos, PhD
Co-President, Graduate Committee

Date

Leyda León, PhD
President, Graduate Committee

Date

Raúl E. Torres Muñoz, PhD
Chairperson of the Department

Date

Paul A. Sundaram, PhD
Graduate Studies Representative

Date

Abstract of Dissertation Presented to the Graduate School
Of the University of Puerto Rico in Partial Fulfillment of the
Requirements for the Degree of Master of Science

**DIGITAL SIGNAL ANALYSIS FOR DETECTION OF AIR BUBBLES ON
ARTIFICIAL THIGH VESSELS**

By

ANDRES SAAVEDRA RUIZ

Chair: LEYDA LEON

Co-Chair: SILVINA CANCELOS

Major Department: ELECTRICAL ENGINEERING

ABSTRACT

Decompression sickness (DCS) occurs when divers rise to the surface exposing the body to sudden changes in pressure, generating nitrogen bubbles in tissues, causing serious bodily injury and even death. To prevent this risk, tables indicating divers' ascent rates, descent rates, and waiting time in between decompression stops have been developed. Even with the help of such tables, decompression sickness still occurs in individuals who follow the instructions in dive tables. Therefore, prevention of DCS may be viable with a method that detects the presence of bubbles in real time.

In this thesis, we show a new method for bubble detection using a simplified human thigh prototype constructed with a piezoelectric ring (PZT) placed around it. In order to test this new method, we use two high-speed cameras, to record the bubbles produced in a bubble generator system, and pill microphones (PM) to measure disturbances in the prototype when it is in resonance.

The electrical signals from the piezoelectric ring (PZT) and microphones (PM) are the inputs to a pattern recognition algorithm. In the classification stage of the pattern recognition, three classifiers are tested; the choice of classifiers are determined by the best accuracy. A neural network based classifier performed the best detection of bubbles for five classes of different diameter ranges. The detection accuracy was 98%.

Resumen de Disertación Presentado a Escuela Graduada
De la Universidad de Puerto Rico como requisito parcial de los
Requerimientos para el grado de Maestría en Ciencias

**ANÁLISIS DE SEÑAL DIGITAL PARA LA DETECCIÓN DE BURBUJAS
DE AIRE SOBRE VASOS SANGUÍNEOS DE UN MUSLO ARTIFICIAL**

Por

ANDRES SAAVEDRA RUIZ

Consejera: LEYDA LEON

Co-Consejera: SILVINA CANCELOS

Departamento: INGENIERIA ELECTRICA

RESUMEN

La enfermedad de descompresión (DCS) ocurre cuando los buzos ascienden a la superficie exponiendo el cuerpo a cambios bruscos de presión, generando burbujas de nitrógeno en los tejidos, causando serias lesiones en el cuerpo e incluso la muerte. Para evitar este riesgo, se han desarrollado tablas que indican diversas tasas de ascenso, las tasas de descenso y el tiempo de espera durante las paradas de descompresión. La frecuente aparición de ésta enfermedad es un problema que permanece en estudio, debido a que aún ocurre a buceadores que siguen las instrucciones de la tabla de buceo. Por lo tanto, la prevención de DCS podría ser viable con un método que detecte la presencia de burbujas en tiempo real.

En ésta tesis se describe un nuevo método para la detección de burbujas en un prototipo simplificado del muslo humano, por medio de un anillo piezoeléctrico (PZT) colocado alrededor de éste. En adición, utiliza dos cámaras de alta velocidad, que graban las burbujas provenientes del sistema generador de burbujas y también pequeños micrófonos (PM), que miden las perturbaciones dentro del prototipo cuando se encuentra en resonancia.

Las señales eléctricas provenientes del anillo piezoeléctrico (PZT) y de los micrófonos (PM), son las observaciones de entrada a un patrón de reconocimiento. En la etapa de clasificación del patrón de reconocimiento, tres clasificadores son probados; la elección de dichos clasificadores se determinó por la mejor precisión. El algoritmo de redes neuronales presentó la mejor detección de burbujas para cinco clases de rangos de diámetro distintos con una precisión de 98%.

Copyright © 2015

By

ANDRES SAAVEDRA RUIZ

To my family ...

To my mother, for her constant support, trust, and unconditional love which sustained me throughout my life. To my sister and my nephew, who always have provided me support during my studies. To my girlfriend for all her love and support.

ACKNOWLEDGEMENTS

I would like to acknowledge and give my utmost gratitude to my co-advisor Dr. Silvina Cancelos for her support during the development of this research. I would also like to give special thanks to my advisor Dr. Leyda León for her support and friendship. I would also like to thank Dr. Lizdabel Morales for her guidance and her suggestions on this research.

To my fellow graduate companions and laboratory partners, especially William García, for all the help I received from him.

In addition, I would like to thank a group of friends who have always been there to contribute with ideas and offer support: Pablo, Gilberto, Cristian, Carlos and Luis.

I would also like to thank my financial contributors including: the Department of Defense (DoD), and the Electrical Engineering Department.

TABLE OF CONTENTS

ABSTRACT.....	I
RESUMEN	III
DEDICATION.....	VI
ACKNOWLEDGEMENTS.....	VII
TABLE OF CONTENTS.....	VIII
LIST OF FIGURES	XIV
LIST OF TABLES.....	XIX
CHAPTER I.....	1
1 INTRODUCTION	1
1.1 Decompression Sickness	1
1.2 Problem Statement	4
1.3 Related work	5
1.4 Research Strategy and Objectives	6
1.5 Summary of the Following Chapters	7
CHAPTER II.....	9
2 THEORETICAL BACKGROUND.....	9
2.1 Acoustic Chambers	9
2.1.1 Piezoelectric Ring.....	10

2.2	Bubble Detection Methods.....	13
2.2.1	Ultrasound.....	13
2.2.2	Pulse-Echo Ultrasound.....	14
2.2.3	Doppler Ultrasound.....	15
2.2.4	Harmonic Ultrasound.....	16
2.2.5	Dual Frequency Ultrasound	18
2.3	Pattern recognition: definition.....	19
2.3.1	Sensor.....	20
2.3.2	Features extraction	20
2.3.2.1	The Root Mean Square	20
2.3.2.2	Discrete Fourier Transform	23
2.3.2.3	Cross-correlation	26
2.3.2.4	Summary.....	28
2.3.3	Classifier	29
2.3.3.1	Support vector machine	29
2.3.3.2	Artificial Neural Networks (NN).....	33
2.3.3.3	K-mean	37
CHAPTER III	40
3	METHODOLOGY	40

3.1	Artificial Thigh.....	40
3.2	Bubble Generating System.....	41
3.3	Degassing Protocol.....	44
3.4	Data Acquisition.....	45
3.4.1	Voltage divider.....	45
3.4.2	Frequency response.....	46
3.4.3	Data acquisition card.....	47
3.5	High Speed Cameras	53
3.6	Timing hub	56
3.7	Experimental Protocol.....	59
3.8	Implementation of Classifiers	61
3.8.1.1	Support vector machine	62
3.8.1.2	Artificial Neural Networks	63
3.8.1.3	K-mean	64
CHAPTER IV		65
4	EXPERIMENTAL RESULTS.....	65
4.1	Result obtained from the features extraction.....	65
4.1.1	Bubble in middle of the PZT ring.....	65
4.1.2	Bubbles located 1 cm from the PZT ring.....	69

4.1.3	Bubbles located 2 cm from the PZT ring.....	72
4.2	Bubble detection with 1 feature for 2 Classes.....	73
4.2.1	K-mean.....	73
4.2.2	SVM.....	75
4.2.3	NN.....	76
4.3	Bubble detection with 1 feature for 5 Classes.....	77
4.3.1	K-mean.....	78
4.3.2	SVM.....	80
4.3.3	NN.....	81
4.4	Bubble detection with 3 features for 2 classes.....	82
4.4.1	K-mean.....	82
4.4.2	SVM.....	84
4.4.3	NN.....	85
4.5	Bubble detection with 3 features for 5 classes.....	86
4.5.1	K-mean.....	87
4.5.2	SVM.....	88
4.5.3	NN.....	89
4.6	Overview and rate of convergence.....	90
4.7	Summary of the results and analysis.....	92

4.8	Further testing	96
CHAPTER V		99
5	CONCLUSION AND FUTURE WORK	99
5.1	CONCLUSION	99
5.2	FUTURE WORK	100
6	REFERENCES	102
7	APPENDIX	105
7.1	Algorithm setup bubble generating system	105
7.2	Algorithm setup frequency response	106
7.3	Algorithm setup acquisition signals	107
7.4	Algorithms current drop detecting	108
7.4.1	Method 1	108
7.4.2	Method 2	109
7.5	K-mean Algorithm and STD predictor	110
7.6	SVM Algorithm	112
7.7	Neural Network Algorithm	113
7.8	Rate of convergence	114

LIST OF FIGURES

Figure 1: Decompression Sickness type 1. Image taken from N Engl J Med 2010; 362:e67. Cutis Marmorata in Decompression Sickness. Used with the permission of Vasileios N. Kalentzos, M.D., M.P.H. URL of the website: http://www.nejm.org/doi/full/10.1056/NEJMicm0909444	2
Figure 2: Decompression sickness type 2. ‘© Scubadoc’s Diving Medicine Online, 1996-2009. Used with permission of Ernest Campbell, MD, FACS.	3
Figure 3: Diver table: No-decompression limits and group designation table. ‘© PADI 2013. Used with permission of DSAT and PADI.	4
Figure 4: Standing waves Harmonics.	9
Figure 5: The Van Dyke Model. Simplified equivalent RLC circuit	11
Figure 6: A. Echo ultrasound without bubbles. B. Echo ultrasound with bubble. Werner Sölken 2008 - 2015	14
Figure 7: Relationship between pressure amplitude and bubble radius. Taken from (Dee, 2011).	17
Figure 8: Dual frequency data of a target in the hip of an anesthetized swine before and after injection of microbubbles. Taken from (Buckey, et al., 2009).	19
Figure 9: Pattern recognition diagram.	19
Figure 10: The red circles are the RMS value from the Coqui Frog Song signal (blue line).	21
Figure 11: A. Captured 3 Phase voltage sag waveform. B. Captured 3 Phase voltage swell waveform.	23
Figure 12: A. Original signal from the Coqui Frog Song (CFS). B. FFT of the Coqui Frog Song (CFS).	25

Figure 13: A. Signal of the sensor 1 from the measured vibrations caused by a car as it crosses a bridge. B. Is the same signal measured in sensor 2 but it arrives at an earlier time than the signal from Sensor 1. Example from MathWorks. “xcorr Reference Page.” Accessed August 17, 2015. http://www.mathworks.com/help/signal/ref/xcorr.html	27
Figure 14: Cross correlation between sensor 1 and sensor 2. Example from MathWorks. “xcorr Reference Page.” Accessed August 17, 2015. http://www.mathworks.com/help/signal/ref/xcorr.html	28
Figure 15: An example of a linearly separable set.....	30
Figure 16: Non-linear neuron model.....	33
Figure 17: Threshold activation function.....	34
Figure 18: Sigmoid activation function	35
Figure 19: Hyperbolic tangent function	36
Figure 20: K-mean Block Diagram.....	38
Figure 21: Acoustic Chamber.	41
Figure 22: Bubble generator device.....	42
Figure 23: Bubble generator system.	43
Figure 24: Power converter diagram.....	43
Figure 25: Prototype scheme.	44
Figure 26: Voltage Divider A. implemented B. Electrical circuit.	45
Figure 27: Frequency response of the acoustic chamber.	46
Figure 28: Data acquisition card NI 6356.....	48
Figure 29: Method 1 for acquired data was used for this case.....	49

Figure 30: Electrical signal from the PZT. Method 2 for acquired data was used for this case. A- Signal current without bubble. B- Signal current with bubble.	51
Figure 31: Bubbles in the bubble generator. Images captured with camera 1.....	54
Figure 32: Images captured in the camera 2.	54
Figure 33: Histogram of the microbubbles from the needle.	55
Figure 34: Histogram of the microbubbles from the artery.	56
Figure 35: Timing hub device.....	56
Figure 36: Timing hub settings from Dynamic Studio.	57
Figure 37: Timing hub diagram.	58
Figure 38: Experimental setup #1.	59
Figure 39: Experimental setup #2.	60
Figure 40: Experimental set-up.....	61
Figure 41: Effect of bubble size measured in the PZT when it is actuated at the time the bubble reaches the PZT center. Number of samples =126.	65
Figure 42: Data obtained by measuring the voltage in a pill microphone located at the bottom edge of the PZT when the PZT was actuated when the bubble reached the PZT center. Number of samples = 63.	67
Figure 43: Data obtained by measuring the voltage in a pill microphone located 2cm from the bottom edge of the PZT when the PZT was actuated when the bubble reached the PZT center. Number of samples =63.....	68
Figure 44: Data obtained when the PZT was actuated when the bubble was located at 1cm from the PZT. Number of samples was 38.....	69

Figure 45: Data obtained from measuring the voltage in a pill microphone located at the bottom edge of the PZT when the PZT was actuated when the bubble was located at 1cm from the PZT. Number of samples =38..... 70

Figure 46: Data obtained from measuring the voltage in a pill microphone located at 1cm from the bottom edge of the PZT when the PZT was actuated when the bubble was located at 1cm from the PZT. Number of samples = 38..... 71

Figure 47: Data obtained from measuring the voltage in a pill microphone located 2cm from the bottom edge of the when the PZT was actuated when the bubble was located at 1cm from the PZT. Number of samples = 38..... 72

Figure 48: Data obtained when the PZT was actuated when the bubble was at 2cm below the PZT. Number of samples = 20..... 73

Figure 49: The prediction of the K-mean algorithm response with 100 data samples. 74

Figure 50: Results of the SVM algorithm with 100 data samples. 75

Figure 51: Results of the NN algorithm with 100 samples..... 76

Figure 52: The prediction of the K-mean algorithm was used when 100 data samples corresponding to the PZT were being actuated when the bubbles were at its center. 78

Figure 53: The prediction of the SVM algorithm was used when 100 data samples corresponding to the PZT were being actuated when the bubbles were at its center. 80

Figure 54: The prediction of the NN algorithm was used when 100 data samples corresponding to the PZT were being actuated when the bubbles were at its center. 81

Figure 55: Prediction of the K-mean algorithm response with 63 data samples. 83

Figure 56: Results of the SVM algorithm with 63 data samples. 84

Figure 57: Response of the NN algorithm with 63 data samples. 85

Figure 58: Prediction of the K-mean algorithm response with 63 data samples to 3 features and 5 classes.	87
Figure 59: The prediction of the SVM algorithm response with 63 data samples to 3 features and 5 classes.	88
Figure 60: Prediction of the NN algorithm response with 63 data samples to 3 features and 5 classes.	89
Figure 61: Predictor accuracy: A - is to 2 classes, the 3 first bins are the predictor results from 1 feature and the last 3 bins are the predictor results from 3 features. B is to 5 classes, the 3 first bins are the predictor results from 1 feature and the last 3 bins are the predictor results from 3 features.	93
Figure 62: A - indicates the time of convergence to predictors for 2 classes. B - indicates the time of convergence to predictors for 5 classes.	95
Figure 63: Pulse with modulator program in Labview.	105
Figure 64: Frequency response algorithm.....	106
Figure 65: Data acquisition program (Front Panel)	107
Figure 66: Block diagram for amplitude peaks detection. This algorithm was developed in MATLAB 2013.....	108
Figure 67: Block diagram for current drop detection. This algorithm was developed in MATLAB 2013.....	109
Figure 68: Algorithm to detect Current drop in relative value using "method 2"	110

LIST OF TABLES

Table 1: Setup for the high speed cameras.	53
Table 2: Example of the input data to classifiers.....	62
Table 3: Results from the k-mean prediction to 1 feature and 2 classes.....	74
Table 4: Results from the SVM prediction to 1 feature and 2 classes.....	76
Table 5: Results from the NN prediction to 1 feature and 2 classes.....	77
Table 6: Intervals obtained from the k-mean classification to 1 feature and 5 classes.....	78
Table 7: Results from the k-mean prediction to 1 feature and 5 classes.....	79
Table 8: Results from the SVM prediction to 1 feature and 5 classes.....	80
Table 9: Results from the NN prediction to 1 feature and 5 classes.....	82
Table 10: Results from the k-mean prediction to 3 feature and 2 classes.....	83
Table 11: Results from the SVM prediction to 3 feature and 2 classes.....	84
Table 12: Results from the NN prediction to 3 feature and 2 classes.....	86
Table 13: Intervals obtained from the k-mean classification to 3 features and 5 classes.	86
Table 14: Results from the k-mean prediction to 3 feature and 5 classes.....	87
Table 15: Results from the SVM prediction to 3 feature and 5 classes.....	89
Table 16: Results from the NN prediction to 3 feature and 5 classes.....	90
Table 17: Rate of convergence comparison for each algorithm	91
Table 18: Summary of the results.	92
Table 19: Confusion matrix for the k-mean algorithm with 4 features for the data points corresponding to the PZT actuated when the bubbles were at the center of the PZT and for bubbles that were located at 1cm away from the PZT when it was actuated.....	96

Table 20: Confusion matrix for the SVM algorithm with 4 features for the data points corresponding to the PZT actuated when the bubbles were at the center of the PZT and for bubbles that were located at 1cm away from the PZT when it was actuated. 97

Table 21: Confusion matrix for the neural network algorithm with 4 features for the data points corresponding to the PZT actuated when the bubbles were at the center of the PZT and for bubbles that were located at 1cm away from the PZT when it was actuated. 98

Table 22: Data acquisition program settings. 108

Table 23: Comparison of the time of convergence to classifiers in different hardware devices. 117

CHAPTER I

INTRODUCTION

1.1 Decompression Sickness

Diving is the action where an individual immerses himself in water (sea, lake or river) to carry out marine-related activities, rescue operations, structure repairs, among others. Like any other activity, there are risks. These risks can be present because of the complexity of the work, and others may be avoided by following certain safety rules. Nevertheless, diving in and of itself represents exposure to a dangerous disease called decompression sickness.

Decompression sickness (DCS) is a disease that occurs with the sudden loss of pressure which generates small bubbles. These bubbles (nitrogen bubbles), formed in blood and other tissues, are seen in divers who surface too quickly (Bookspan, 1997). DCS can occur when diving at approximate depths of 60 to 65 meters. As a safety precaution, a level of monitoring should be performed at a depth of 30-40 meters to identify the diver's condition and avoid unnecessary risks. Monitoring is important since DCS may cause temporary paralysis, permanent injury or death.

In 1878, a French scientist named Paul Bert, demonstrated the formation of bubbles in tissues and proposed the idea of a slow ascent to the surface (Bookspan, 1997). The symptoms associated with decompression can be divided into two types:

- Type I: is usually characterized by pain in the joints with mottling of the skin producing a red or purplish-blue tinge, fatigue, mood swings, and irritable behavior. Onset may be gradual and may be transient (Gilliam, 2012).



Figure 1: Decompression Sickness type 1. Image taken from N Engl J Med 2010; 362:e67. Cutis Marmorata in Decompression Sickness. Used with the permission of Vasileios N. Kalentzos, M.D., M.P.H. URL of the website: <http://www.nejm.org/doi/full/10.1056/NEJMicm0909444>.

- Type II: is characterized by central nervous system (CNS) spinal and cranial abnormalities often masked by pain distractions. In addition, some patients have symptoms such as: unusual fatigue, headache, and abdominal encircling (Gilliam, 2012). The location of the above symptoms are shown in Figure 2.

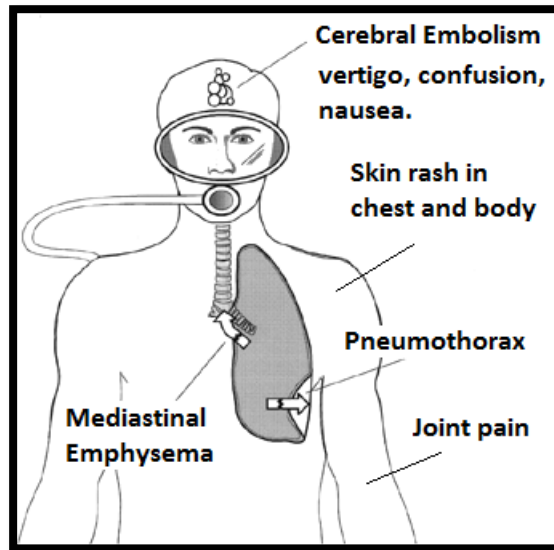


Figure 2: Decompression sickness type 2.
© Scubadoc's Diving Medicine Online, 1996-2009. Used with permission of Ernest Campbell, MD, FACS.

To avoid injury due to decompression sickness while diving, dive tables have been developed by the British biologist John Scott Haldane (Acott, 1999). These tables provide information about the speed of descent, ascent to the surface, and the waiting time for decompression stops, which allow bubbles formed to be dissolved. A typical diving table is shown in Figure 3.

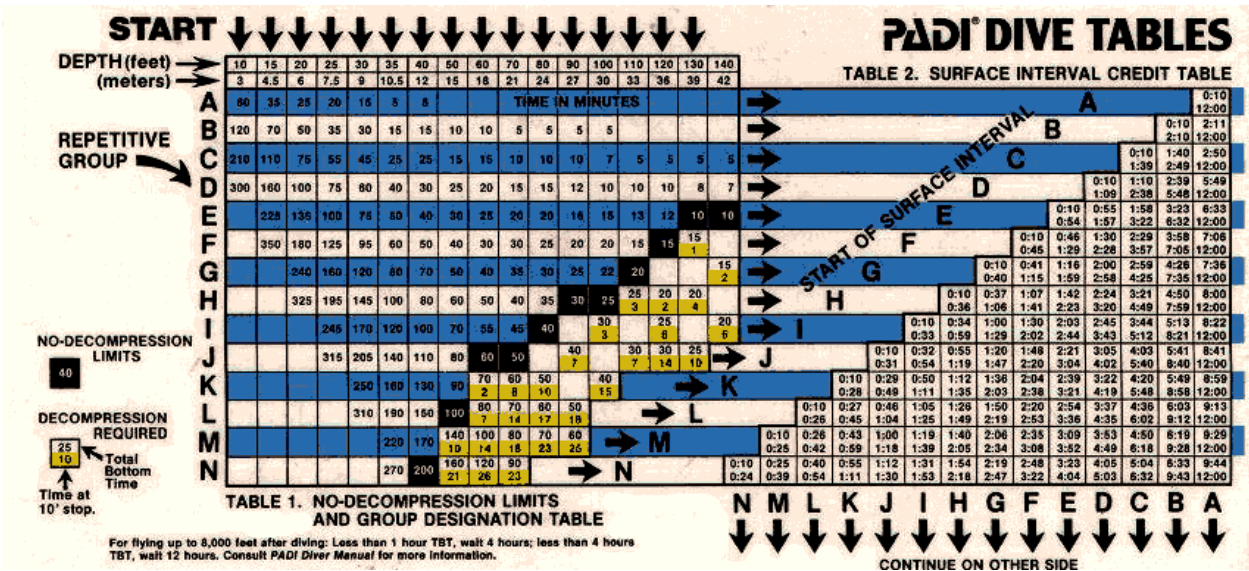


Figure 3: Diver table: No-decompression limits and group designation table. © PADI 2013. Used with permission of DSAT and PADI.

Since the occurrence of decompression sickness is correlated to bubble formation in tissues, researchers began studies on the detection of bubbles using different methods.

1.2 Problem Statement

The incidence of decompression sickness is a problem that continues to be studied since it is seen in divers that strictly follow dive tables. Research continues in order to determine the causes of decompression sickness; in this field, the main objective is the detection of bubbles. "All bubble detection techniques in some way fail to sample the entire population of bubbles that could potentially exist, for example, as a result of limits in sensitivity or resolution" (Leighton, 1994). One of the methods used to detect bubbles in this field of research is the Doppler method, mostly because the ease of operation and it's relatively reduce cost. Most other systems used today fail to

detect the size and number of micro-bubbles prior to the occurrence of the decompression symptoms (Valentin, 2012).

1.3 Related work

Some of the methods developed using ultrasound as a detection tool for the presence of bubbles are the following (Dee, 2011):

- *Pulse echo-ultrasound*: a technique in which pulses of ultrasound generated by a piezoelectric transducer are sent into the region to be studied (tissues), and echo signals resulting from scattering and reflection are detected and displayed. The depth of a reflective structure is inferred from the delay between pulse transmission and echo reception. Stephen Daniels in 1981 (Dee, 2011), used an integrating pulse-echo technique where the number of pulse echo-ultrasounds in a scan of the tissue are counted and recorded in a preselected time interval as a signal. The stationary bubbles would be seen as an increase to the echo count and the non-stationary ones would contribute to the variability in echo count, therefore, the echo count gives an estimate of gas volume in tissues.
- *Doppler ultrasound*: measures the shift in frequency of a continuous ultrasonic wave when the wave source and/or detector are in motion. Doppler is still the most sensitive technique available. In addition, a Doppler unit is far smaller and less expensive than most instruments required by other methods. The Doppler's ease of operation has aided in its popularity as a tool to examine divers after decompression.

- *Harmonic ultrasound*: technique based on the principle of exciting a bubble with a low frequency signal and comparing it to the bubble resonance frequency. If acoustic energy from the bubble is scattered, it can be detected. The excited bubble will oscillate in a non-linear manner, emitting a wave with a doubled frequency.
- *Dual frequency ultrasound*: uses a low frequency signal (“pump”) to excite bubbles with a known radius, which makes them resonate. A second high frequency signal (“image”) is emitted. When it is incident on the resonating bubbles, a non-linear mixing occurs. This non-linear mixing causes results in a signal with the frequency of the “image” plus or minus the “pump” frequency (Buckey, et al., 2009).

Techniques as pulse echo ultrasound, harmonic ultrasound and dual frequency ultrasound are under study. Doppler bubble detection is useful for deciding whether a diver needs to receive hyperbaric treatment.

1.4 Research Strategy and Objectives

In the bubble dynamics laboratory of the University of Puerto Rico Mayagüez Campus, a method for bubble detection in real time to prevent DCS has been proven to be feasible (Valentin, 2012). The technique was tested on a simulated simplified artificial thigh that acts as an acoustic chamber where the situation of decompression was created by introducing bubbles of known size. Electrical signals emitted by a piezoelectric (PZT) ring placed around the artificial leg indicate the presence of bubbles.

In order to use the above mentioned signals as a bubble detection method, signal analysis should be conducted to determine a relationship between the electrical signals and the presence of

stationary or non-stationary bubbles. Once this relationship was established, a pattern recognition algorithm was developed for the use of creating a data base in order to determine the size and amount of micro-bubbles present in the blood system that can potentially cause decompression sickness.

The main objective of this research is to implement a pattern recognition scheme to indicate the presence of micro-bubbles in a diver's bloodstream and in tissues. In order to achieve this goal, it is necessary to: (i) analyze the signals that are generated due to bubbles passing through the PZT ring, (ii) determine the size of the bubbles using image processing techniques of the images obtained from a high speed camera, and (iii) identify the relationship between the size of the bubbles and the PZT ring signals.

1.5 Summary of the Following Chapters

The thesis is distributed in six chapters:

Chapter I: INTRODUCTION

The introduction is based on the motivation for this research. In addition, it summarizes the strategy to provide a solution to the problem statement.

Chapter II: THEORETICAL BACKGROUND

The theoretical background makes an introduction to pattern recognition, explains the physics of sensors used in the pattern recognition, and the equations governing its classification.

Chapter III: METHODOLOGY

This chapter provides the methods used in pattern recognition such as cameras, sensors, acquisition systems, and software specifications. Also, it provides the experimental setup for pattern recognition.

Chapter IV: EXPERIMENTAL RESULTS

Experimental results describe the relationship found between current drop and the diameter of the bubbles, the bubbles classification through classifiers, and the choice of the best classifier due to their performance and rate of convergence.

Chapter V: CONCLUSIONS

In the concluding chapter the most effective pattern recognition analysis after a complete experimental test is presented; also includes future work aimed at possible improvements in pattern recognition.

CHAPTER II

THEORETICAL BACKGROUND

2.1 Acoustic Chambers

An acoustic chamber is a simple structure that consists of a glass cylinder with a piezoelectric (PZT) device glued around it (Cancelos, et al., 2005). They are made to generate large and controlled pressure oscillations. The excitation of the glass cylinder is caused by the motion of the PZT that deforms when a sinusoidal voltage is applied to it. The crystal contracts and expands at the same frequency at which the electrical current changes polarity. The piezoelectric deformation is transferred to the walls; this is the force that creates the standing acoustic pressure field in the liquid (Cancelos, et al., 2010).

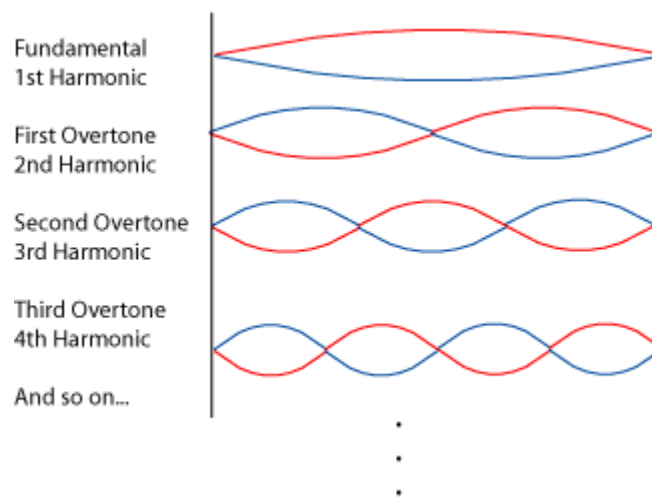


Figure 4: Standing waves Harmonics.

For all structures, there is an infinite number of natural vibration modes. Figure 4 shows the different standing waves harmonics, however, the greatest acoustic pressure obtained in the fluid occurs when an oscillating voltage with a frequency that matches the first resonance mode is applied. When the prototype works at the resonance condition, the sensitivity in the elastic properties of the medium become high. If a bubble is introduced in the acoustic chamber, it causes a change in the elastic properties of the fluid, also causing the electrical properties of PZT to change.

2.1.1 Piezoelectric Ring

The piezoelectric ring is a lead-zirconate-titanate ceramic, known by the acronym (PZT). This material has the property of generating an electric current when it is subjected to a mechanical stress, and vice versa when an electric field is applied to the material, it generates a mechanical deformation (Jordan, et al., 2001).

The analysis of the PZT and the interactions with an acoustic chamber is a multi-dimensional model of wave propagation in fluids (Cancelos, et al., 2005).

A simplified piezoelectric model can be explained as a constitutive equation, expressed as:

$$\vec{D} = d_1 \vec{T} + \epsilon^T \vec{E} \quad (2.1)$$

$$\vec{S} = s^E \vec{T} + d_2 \vec{E} \quad (2.2)$$

Where \vec{D} is the electric displacement, d_1 and d_2 are the piezoelectric charge coefficients, respectively for the direct piezoelectric effect and the inverse piezoelectric effect. \vec{T} is the mechanical stress, ϵ^T permittivity constant at constant stress, \vec{E} is the electric field, \vec{S} mechanical strain, and s^E is the mechanical compliance (Ledoux, 2011). Equations (2.1) and (2.2) constant temperature and linear coupling between electric field and strain were assumed. Equation (2.1) shows that part of an electrical field applied to material is converted into mechanical stress. Similarly, equation (2.2) shows that part of a mechanical strain applied to material is converted into an electrical field.

When a piezoelectric material is subjected to acoustic vibrations, it generates an electric field with the same frequency as the vibration. For some frequencies, the transfer of electrical-mechanical energy is maximum, but in other frequencies it is minimum. This behavior, allows the analogy between the piezoelectric and the RLC circuit to be made. The most common electrical circuit used to characterize a piezoelectric device is the Van Dyke Model (Kim, et al., 2008) shown in Figure 5.

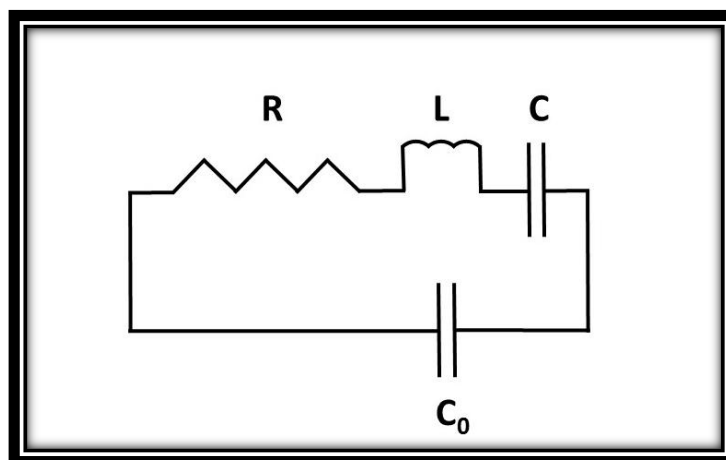


Figure 5: The Van Dyke Model. Simplified equivalent RLC circuit

The following equation shows the equivalent electrical admittance (Y_{eq}) of the circuit shown in Figure 5:

$$Y_{eq} = j\omega C_0 + \frac{1}{R + j(\omega L - \frac{1}{\omega C})} \quad (2.3)$$

In the above equation R , L and C represent the resistance, inductance and capacitance of the system respectively and C_0 is the real value of the measured capacitance of the PZT and it is often called blocked capacitance.

Finally, applying conjugate, and expanding equation (2.3), equation (2.4) can be obtained. The real part (left hand side of equation (2.4)) is called conductance and the frequency that maximizes this quantity corresponds to the mechanical resonance frequency of the system. In this work the electrical conductance will be measured to determine the mechanical resonance of the prototype.

$$Y_{eq} = \frac{R}{R^2 + \left(\frac{\omega^2 LC - 1}{\omega C}\right)^2} + j\omega C_0 + \frac{j\left(\frac{\omega^2 LC - 1}{\omega C}\right)}{R^2 + \left(\frac{\omega^2 LC - 1}{\omega C}\right)^2} \quad (2.4)$$

2.2 Bubble Detection Methods

This section presents some methods for the detection of bubbles such as: basics of ultrasound, pulse echo ultrasound, Doppler ultrasound, harmonic ultrasound, and dual frequency ultrasound.

The ultrasound term indicates sound waves of frequencies above 20 KHz. Frequencies between 1-30 MHz are used as diagnostic tools since they allow to capture images of internal body structures in a non-invasive manner (Lutz, et al., 2011).

2.2.1 Ultrasound

Ultrasound uses the reflection of sound waves off the boundaries between tissues of varying acoustic properties (Dee, 2011). “The acoustic properties of a medium are quantified in terms of its acoustic impedance, which is a measure of the degree to which the medium impedes the motion that constitutes the sound wave” (Lutz, et al., 2011). The acoustic impedance “ z ” is related as:

$$z = \rho c \tag{2.5}$$

Where “ ρ ” is the density of the medium and “ c ” is the velocity of sound. The sound reflection coefficient α at the boundary between two tissue types (z_1 and z_2) is calculated with equation (2.6):

$$\alpha = \left(\frac{z_2 - z_1}{z_2 + z_1} \right)^2 \tag{2.6}$$

As the acoustic impedance of a gas bubble is much lower than the impedance of any tissue in the body (Nishi, et al., 1986) this method can be used as a bubble detector.

2.2.2 Pulse-Echo Ultrasound

This method consists of a pulsed ultrasonic transmitter that sends a signal to scan a tissue region, and a detector that records echoes reflected from scanned tissue in a pre-selected time interval (Daniels, 1981).

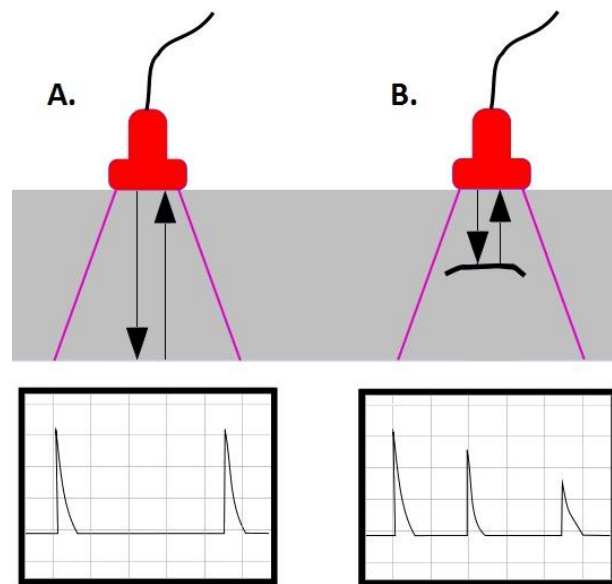


Figure 6: A. Echo ultrasound without bubbles. B. Echo ultrasound with bubble. Werner Sölken 2008 - 2015

The method has been used for stationary and non-stationary bubbles. Figure 6A shows echoes count without bubble and the Figure 6B shows for a stationary bubble, it generates an increase in the echoes counts (Dee, 2011).

The biggest problem with this method is the sensitivity to motion and when it is applied on a person in motion (as a diver) alteration in the echo are observed by increasing or decreasing the count and therefore it produces confusion in the bubble detection method.

2.2.3 Doppler Ultrasound

The Doppler effect is described as a change in the frequency of the wave due to relative motion between the source generating a wave and the observer receiving said wave (Dee, 2011).

The Doppler ultrasound has the wave source and the observer or receiver fixed, but there is a reflector that is in motion. The reflector can act as transmitter and receiver. Therefore the relationship between the frequency experienced by a source and a receptor when both are moving is shown in the equation (2.7):

$$f = f_o \left(\frac{v_s + v_r}{v_s - v_r} \right) \quad (2.7)$$

Where, “ f_o ” is the ultrasound frequency, “ v_r ” is the speed of the reflector, “ v_s ” is the speed of sound and “ f ” is the detected frequency.

When the Doppler effect is applied to the detection of microbubbles, the reflected ultrasound wave produces shifted frequencies. If “ v_s ” is larger than “ v_r ” and the angle between the transducer and the moving object is it considered, Doppler shift “ f_d ” can be computed as (Sande Eftedal, 2007):

$$f_d = \frac{-2f_o v_r \cos(\theta) \cos\left(\frac{\gamma}{2}\right)}{v_s} \quad (2.8)$$

With the angle “ θ ” being the bisector of the transmitter and receiver beams and the direction of movement. The angle “ γ ” is the angle between transmitter and receiver beams (Dee, 2011).

The Doppler shift is not observed in bubbles within tissues because they are stationary structures. On the other hand, the gas bubbles in the blood flow present strong reflections that can be distinguished (Sande Eftedal, 2007).

2.2.4 Harmonic Ultrasound

This method uses an acoustic field with a wavelength greater than the radius of the bubble. By inducing a bubble to said acoustic field, it will respond to changes in pressure and it will oscillate causing scattering in the acoustic energy and the bubble can be detected.

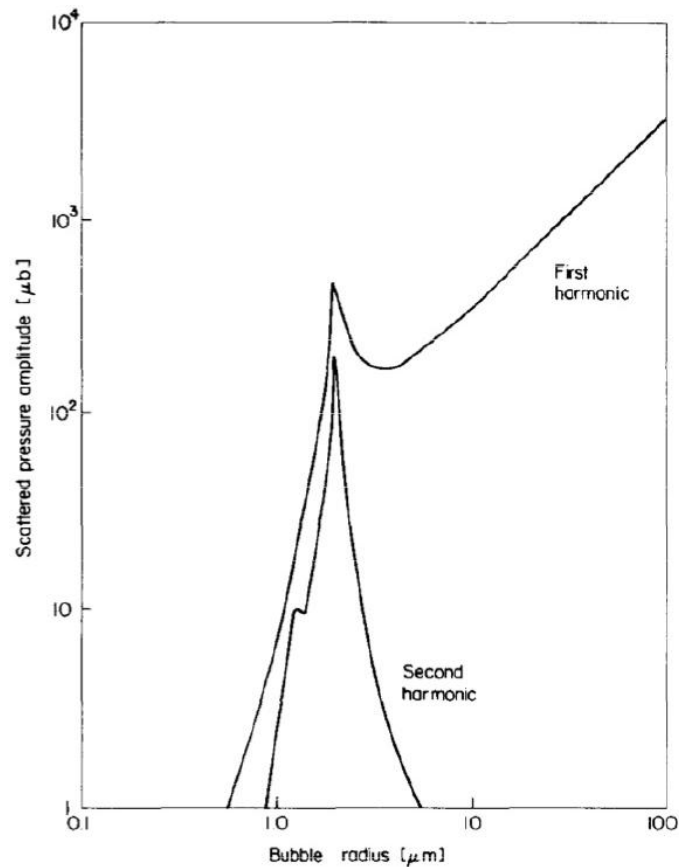


Figure 7: Relationship between pressure amplitude and bubble radius. Taken from (Dee, 2011).

(Brock-Fisher, 2004) measured the scattered pressure as a function of the bubble radius for the first and second harmonic. The results show that both harmonics have a linear response for bubble radius smaller than approximately 4 μm where both present a peak in pressure. However, as shown in Figure 7, the first harmonic continues showing a linear increase in pressure as the bubble radius increases, while the second harmonic doesn't. Moreover, the first harmonic can be measured for bigger bubble radius. This means that the largest bubbles produce the greatest first harmonic response. Otherwise, the second harmonic does not. By excluding the second harmonic, the bubble can be detected with the first harmonic (Dee, 2011).

2.2.5 Dual Frequency Ultrasound

This method applies two waves with different frequencies. The first wave is called “pump (f_p)”, and the second wave is called “image (f_i)”. The frequency range of the pump operation is between low KHz to low MHz. The pump frequency is adjusted to different bubble sizes, i.e, the pump frequency is adjusted to the resonance of the bubble’s target size. If a bubble with a resonance frequency equal to the pump frequency is present, then a wave with a frequency given by equation (2.9) is detected.

$$f_{DFU} = f_i \pm f_p \quad (2.9)$$

In an experimental study conducted by (Buckey, et al., 2009) the applicability of this method was proven to be feasible. They used a $f_i = 5$ MHz and the $f_p = 2.25$ MHz and the results they obtained are shown in Figure 8 where a received signal at 2.75 MHz, which is comparable with $f_i - f_p$ is observed indicating the presence of micro-bubbles with a mean diameter of 2 – 3 μm .

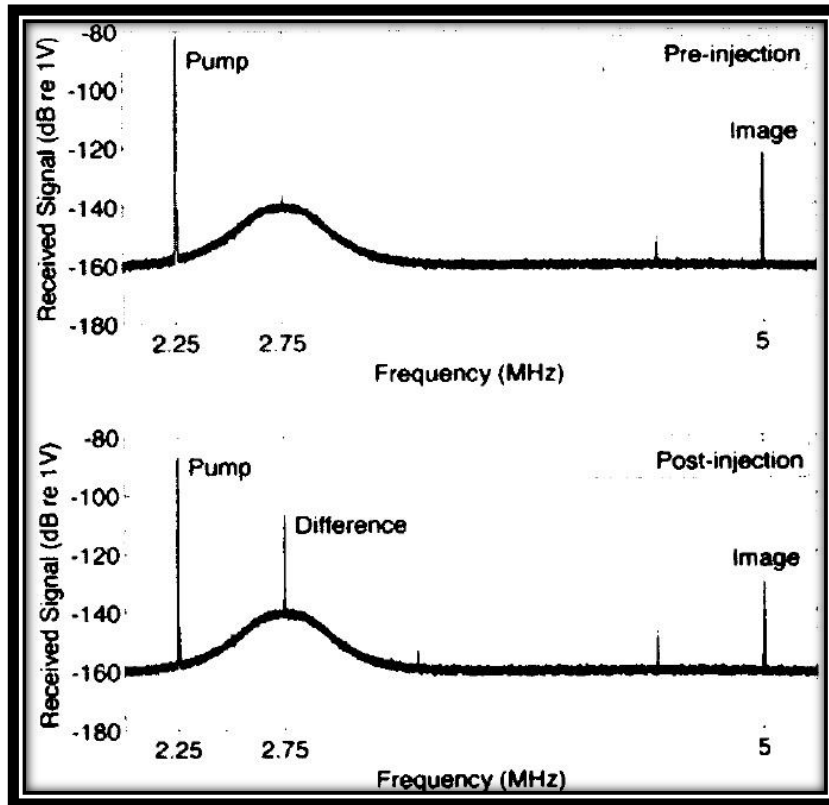


Figure 8: Dual frequency data of a target in the hip of an anesthetized swine before and after injection of microbubbles. Taken from (Buckey, et al., 2009).

2.3 Pattern recognition: definition

Pattern recognition is the act of taking in raw data and taking an action based on the “category” of the pattern (Duda, et al., 2000). A simplified process flow diagram of pattern recognition as proposed by (Webb, 2002) is illustrated in Figure 9.



Figure 9: Pattern recognition diagram.

2.3.1 Sensor

A *sensor* is a device capable of capturing information and transforming physical or chemical magnitudes into electrical magnitudes. In our case, the sensors are comprised of the piezoelectric ring, pill microphones, and high speed cameras.

2.3.2 Features extraction

Feature extraction is the process which determines the system variables that will be used as classifiers (Duda, et al., 2000). There are several techniques that are typically used on the row data to extract a useful variable. The most widely used techniques to process data are: the Root Mean Square (RMS), the Discrete Fourier Transform (DFT) and the Cross Correlation. The choice of technique will be based upon the type of change in the signal induced by the presence of the bubbles.

2.3.2.1 The Root Mean Square

When a signal has only amplitude changes, the common method to analyze this phenomenon is the root mean square (RMS). The RMS method takes a square of each point that represents the waveform (x_N^2), dividing it by the length of the waveform (N), and obtaining the mathematical average. The RMS is defined as:

$$X_{RMS} = \sqrt{\frac{(x_1^2 + x_2^2 + x_3^2 + \dots + x_N^2)}{N}} = \sqrt{\frac{1}{N} \sum_{i=1}^N x_i^2} \quad (2.10)$$

The RMS method is usually applied in power system measurements, because it is fast and it requires less memory than other methods. (Panagiotakis, et al., 2005), used the RMS method as a speech/music discriminator. Two signals were acquired: the first one was a speech signal (the total duration was 11328 sec) and the second one was a music signal (the total duration was 3131 sec). For both signals the RMS was computed and the next step was to calculate the histogram from both RMS values. The distributions obtained from the histograms (histogram of the speech signal and the histogram of the music signal) are almost non-overlapping, therefore, this method is adequate as a discriminator.

Figure 10, shows an example of the RMS method applied on the *coqui frog song* (CFS) signal.

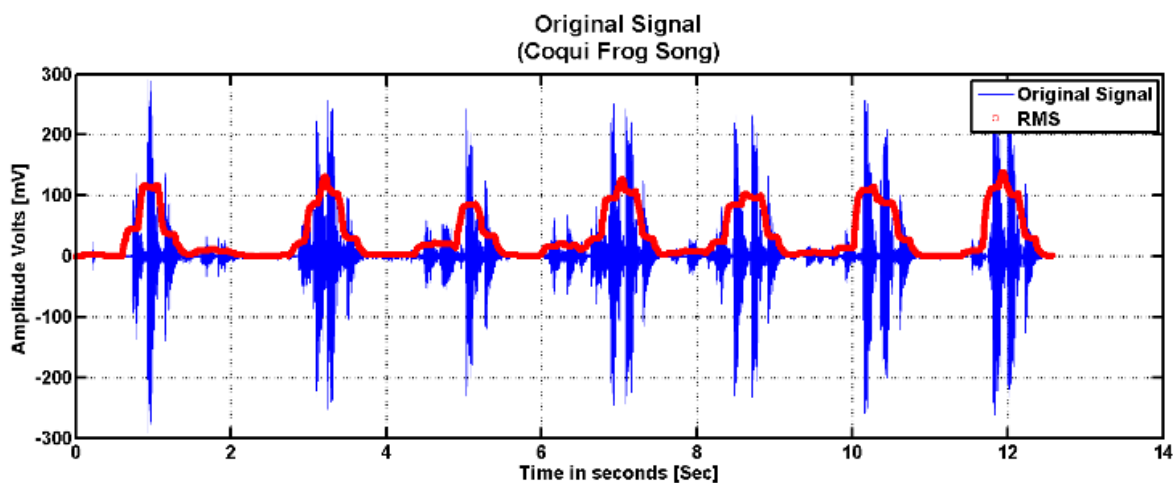


Figure 10: The red circles are the RMS value from the Coqui Frog Song signal (blue line).

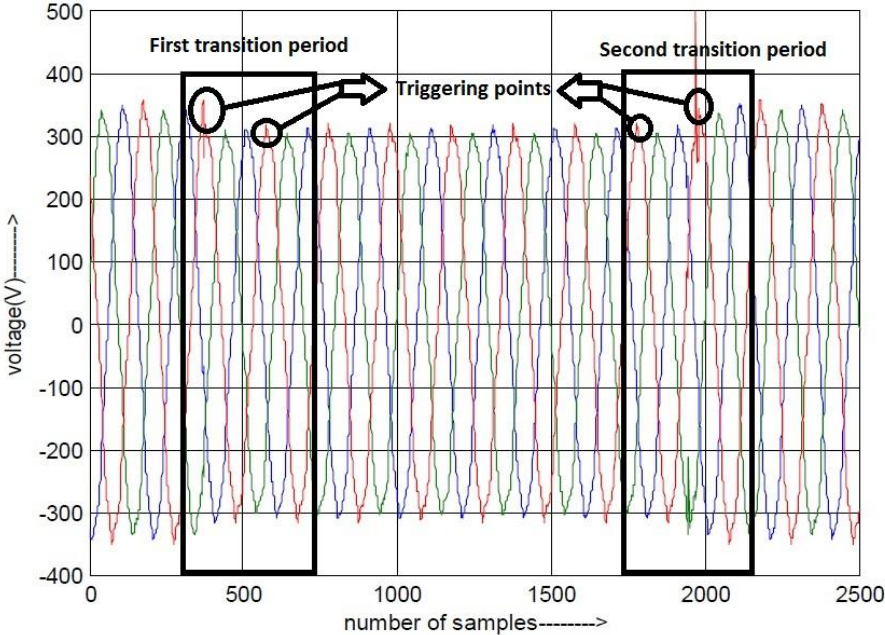
The RMS value increases according to the amplitude of the original signal. One problem with this method is shown with the above example; even though the signal comes from the same

frog, there are fluctuations. The RMS value requires similar conditions when used for signal detection, otherwise, it will generate false positives.

(Ingale, et al., 2013), used the RMS method as detection of power quality disturbances.

The RMS value was computed for 2 cases: sag waveform and swell waveform.

A.



B.

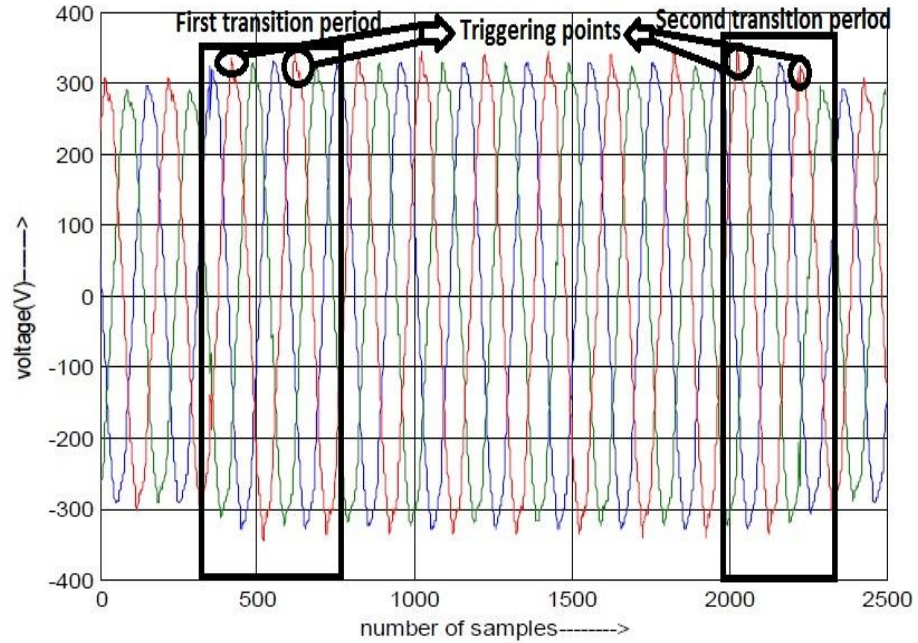


Figure 11: A. Captured 3 Phase voltage sag waveform. B. Captured 3 Phase voltage swell waveform.

Figure 11A shows a 3 phase voltage sag waveform with 2 transition periods and four triggering points. Triggering points refer to sudden changes on the voltage amplitude. When the RMS was computed, it detected 5 triggering points of the 4. A similar problem was found when the swell waveform was analyzed (Figure 11B). This method shows high sensitivity to changes in signal amplitude causing false positives for the triggering point's detection, but on the other hand, it is useful for the changes in amplitude detection.

2.3.2.2 Discrete Fourier Transform

The Discrete Fourier Transform (*DFT*) is a tool that, besides transforming the samples of signals from the time domain into the frequency domain, can be used in image compression,

interpolation, and in others tasks (Franchetti, et al., 2011). *DFT* is a modification of Fourier transform. The DFT is used, when the data are available as sampled time function form, and it were represented by a time series of amplitudes with fixed time intervals of limited duration. The DFT is calculated with the formula (Diniz, et al., 2010):

$$X_k = \sum_{i=0}^{N-1} x_i e^{-j2\pi i k / N} \quad (2.11)$$

Where N is the total amount of the data points, x_i refers to each point of the signal with $i = 0, \dots, N-1$, X_k is the amplitude of each frequency k , with $k = 1 .. N-1$.

The frequency resolution Δf is determined by:

$$\Delta f = \frac{f_s}{N} \quad (2.12)$$

With f_s as sample rate in samples per seconds.

The Fast Fourier Transform (FFT) is a faster version of the DFT. Therefore, the FFT algorithms such as Cooley-Tukey reduce the computational work and the rate of convergence. The DFT is not suitable for non-stationary signals, in which case the STFT should be applied. The STFT, splits the signal into intervals that are considered as stationary, and then the DFT is used in each partitions (Pérez, et al., 2006).

An example of the analysis of signals using FFT is shown in Figure 12. In this example the Coqui frog song was analyzed (Figure 12A). At first glance the different frequency components are not noticeable.

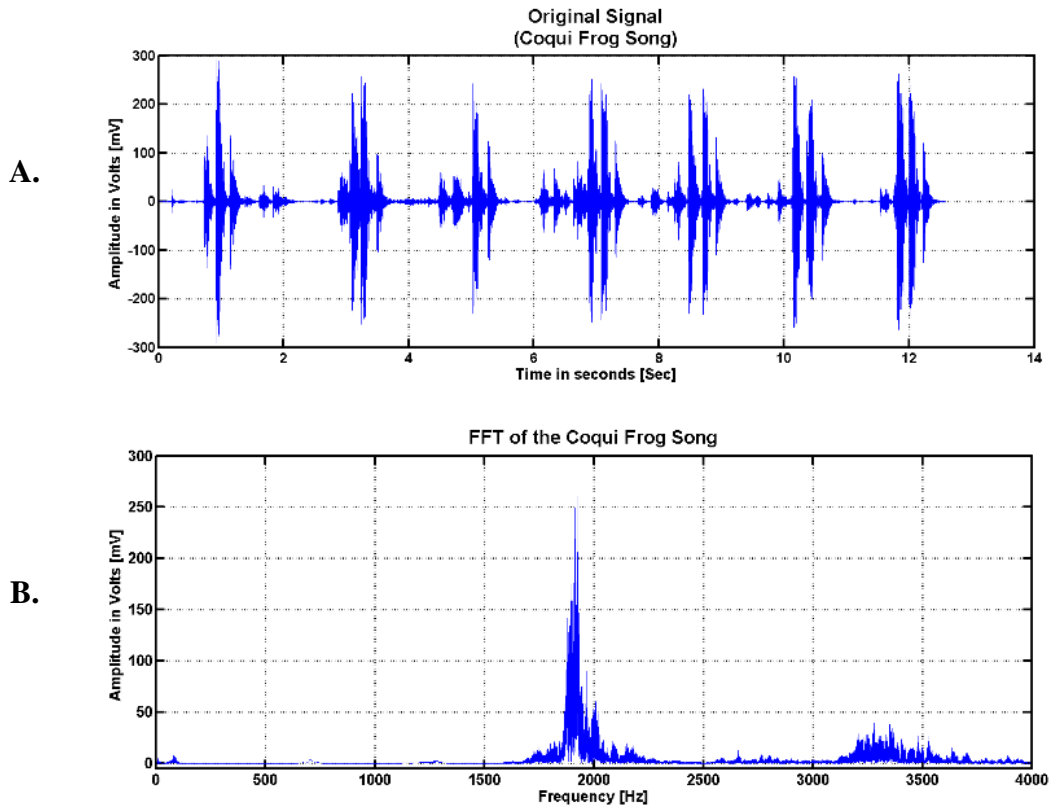


Figure 12: A. Original signal from the Coqui Frog Song (CFS). B. FFT of the Coqui Frog Song (CFS).

Figure 12B shows the frequency components of the CFS, the components between 1800-2100 Hz characterize the “Co” and the components between 3200-3500 Hz represents the “qui”. The use of the DFT in this case is capable of extracting the main features of the CFS.

2.3.2.3 Cross-correlation

The *auto-correlation* and *cross correlation* are used to analyze the similarity between signals. If the comparison of the signal is done with itself, it is called “*auto-correlation*”, and it is defined by equation (2.13) and equation (2.14) for the case of continuous and discrete signals respectively.

$$R_{xx}(\tau) = \int_{-\infty}^{\infty} x(t)x(t-\tau)dt \quad (2.13)$$

$$R_{xx}(m) = \sum_{-\infty}^{\infty} x(n)x(n-m) \quad (2.14)$$

The *cross correlation* between two signals is defined by equation (2.15) and equation (2.16) for continuous signals and discrete signal respectively.

$$R_{xy}(\tau) = \int_{-\infty}^{\infty} x(t)y(t-\tau)dt \quad (2.15)$$

$$R_{xy}(m) = \sum_{-\infty}^{\infty} x(n)y(n-m) \quad (2.16)$$

In equations (2.13) and (2.15) “ t ” is the time and “ τ ” is the time shift. $\tau = 0, \pm a_1, \pm a_2, \dots, a_{T-1}$, where “ T ” is the length of the analyzed signal and a_n refers to interval sections of the signal (smaller than the period of the signal). In the equations (2.14) and (2.16) “ x_n ” refers to each data

in the signal and “ m ” is the “lag” (Stein, 2000). “ m ” is defined as $0, \pm 1, \pm 2, \dots, N-1$, where N is the length of the sampled signal.

In the analysis of structures, autocorrelation is frequently used to determine for example the condition of bridges. An example is shown in Figure 13:

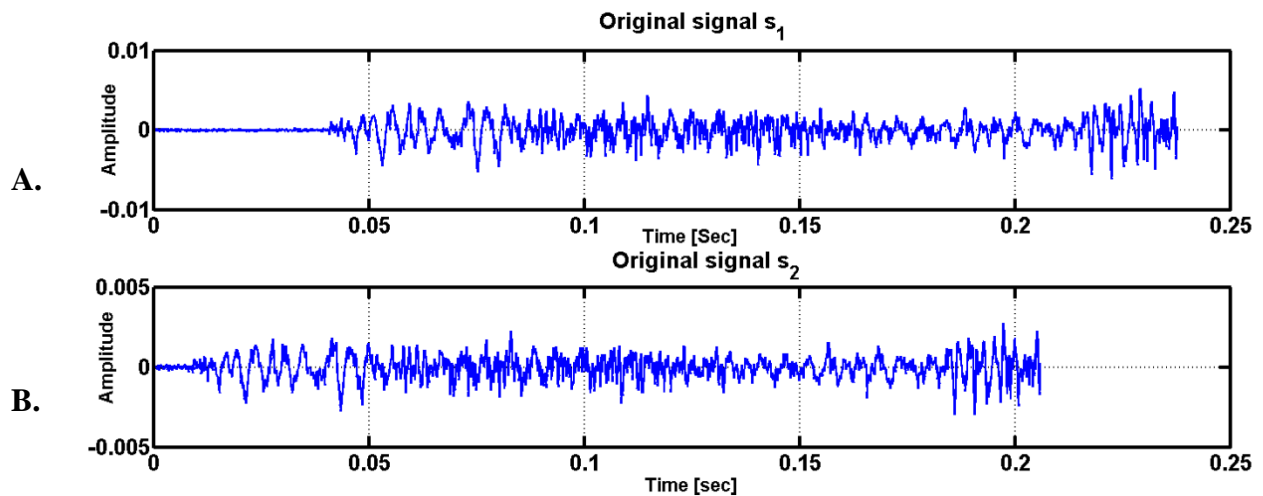


Figure 13: A. Signal of the sensor 1 from the measured vibrations caused by a car as it crosses a bridge. B. Is the same signal measured in sensor 2 but it arrives at an earlier time than the signal from Sensor 1. Example from MathWorks. “xcorr Reference Page.” Accessed August 17, 2015. <http://www.mathworks.com/help/signal/ref/xcorr.html>.

Figure 13A shows the vibrations measured by sensor 1 when a car crosses a bridge. Figure 13B shows a similar signal measured by sensor 2 but it arrives at an earlier time than the signal from Sensor 1.

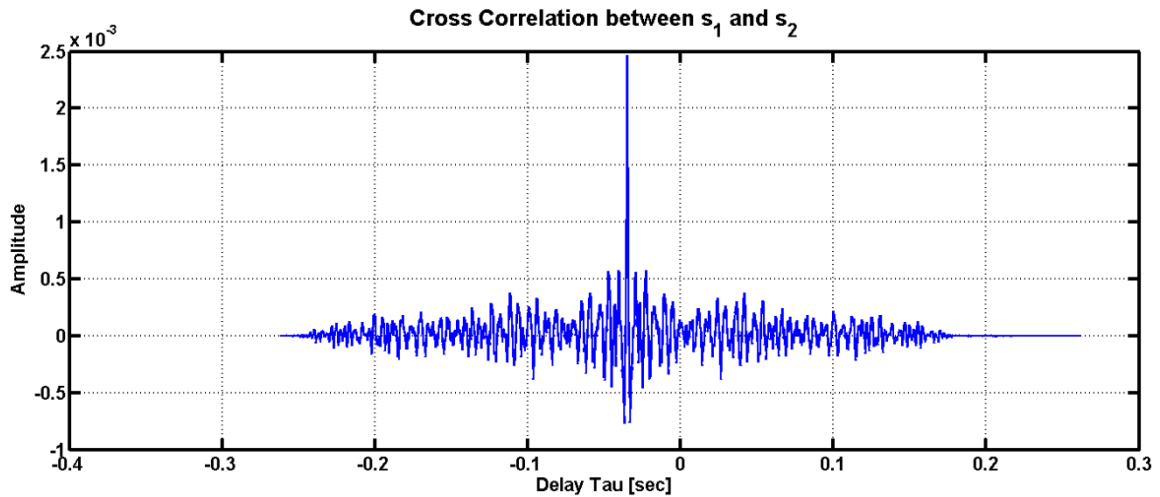


Figure 14: Cross correlation between sensor 1 and sensor 2. Example from MathWorks. “xcorr Reference Page.” Accessed August 17, 2015. <http://www.mathworks.com/help/signal/ref/xcorr.html>.

When the cross correlation was applied, the delay between the sensors 1 and 2 is clearly identified (see Figure 14). The absolute maximum of the cross correlation amplitude (is the same as the original signal) occurs for $\tau = 0.035 \text{ sec}$, which is coincident with the delay between the sensors. Therefore, the cross correlation indicates the similarity between signals (showing the maximum amplitude and comparing it with the original signal), and, it shows the delay between signals too.

2.3.2.4 Summary

The above mentioned methods should be used depending on the approach to extract information.

- The **RMS** is useful for extracting features related to changes in amplitude.
- The **DFT** is useful to extract features related to frequency.

- The **Cross correlation** is useful for extracting features related to changes in amplitude, in frequency and delays between signals.

2.3.3 Classifier

The main function of the *classifier* is to assign different characteristics to groups with largest similarity between them. The classifiers can be of two types: *supervised* or *unsupervised*.

The *supervised* classification is the essential tool used for extracting quantitative information. Using this method, the analyst has sufficient known data available to generate representative parameters for each class of interest. This step is called training. Once trained, the classifier is used to attach labels to all the data according to the trained parameters (Jain, et al., 1999). Among the most widely used supervised classifiers are the Neural Networks (NN) and Support Vectors Machine (SVM).

On the other hand, the *unsupervised* classification does not require a human to have the foreknowledge of the classes, and uses clustering algorithms to classify a set of data (Jain, et al., 1999). Among the most widely used unsupervised classifiers is the k-mean.

The choice of the best classifier depends on the application. For example, if clustering of data is needed, the unsupervised classifiers are the most appropriate, while if the detection for recognition is needed the supervised methods should be chosen.

2.3.3.1 Support vector machine

Support Vector Machines (SVM) are defined by kernel functions that analyze data and recognize patterns. The simplicity comes from the fact that Support Vector Machines apply a

simple linear method to the data but in a high-dimensional feature space on-linearly related to the input space. Given a training set, SVM takes a set of input data and predicts, for each given input, which of two possible classes forms the output, making it a non-probabilistic binary linear classifier (Karatzoglou, et al., 2006).

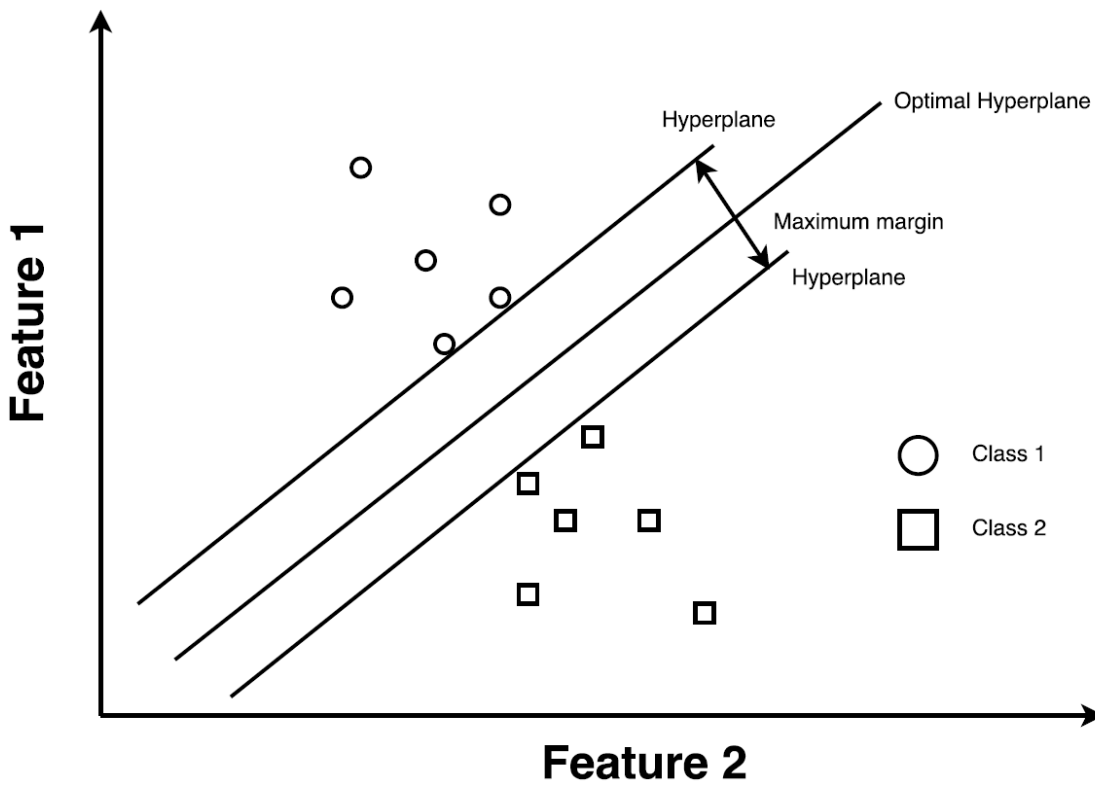


Figure 15: An example of a linearly separable set.

SVM designs a hyperplane to separate classes:

$$s_{(\vec{x})} = \vec{a}^T \vec{x} + b \quad (2.17)$$

Where a^T and b are real coefficients and \vec{x} is the input vector with the trained data.

The classification can be defined as follows:

$$Class = \text{sign}(\vec{a}^T \vec{x} + b) \quad (2.18)$$

Where the sign function determine if the $s_{(\vec{x})}$ is greater than zero, equal to zero or less than zero. The SVM algorithm is known for finding the maximum separation between classes. The decision for each points is given by:

$$Class\ 1 \rightarrow \vec{a}^T \vec{x} + b = 1 \quad (2.19)$$

$$Class\ 2 \rightarrow \vec{a}^T \vec{x} + b = -1 \quad (2.20)$$

The distance to origin is:

$$Hyperplane\ 1 \rightarrow \frac{|1 - b|}{\|w\|} \quad (2.21)$$

$$Hyperplane\ 2 \rightarrow \frac{|-1 - b|}{\|w\|} \quad (2.22)$$

The resulting margin is:

$$\frac{2}{\|w\|} \quad (2.23)$$

Minimizing “ w ” causes the maximization of the separability. This is an optimization problem, with the following solution (Karatzoglou, et al., 2006):

$$\vec{w} = \sum_{i=0}^N \alpha_i y_i \vec{x}_i \quad (2.24)$$

$$\sum_{i=0}^N \alpha_i y_i = 0 \quad (2.25)$$

(Guo, et al., 2015), used the supervised methods SVM and NN to identify muscle motion in humans. The information of the surface electromyography (sEMG) was obtained from six muscles of the upper-limb from 7 subjects. The RMS method was used to extract the feature as the sEMG detects changes amplitude. It was introduced in classifiers creating a pattern for muscle motion. The results showed that NN classifier produced the highest recognition accuracy rate. On the other hand, SVM took less time in training process than NN. SVM classifier is the most appropriate for real time applications.

2.3.3.2 Artificial Neural Networks (NN)

A neuron is a processing element with the capacity to receive and transmit information to another neighbor neuron. Artificial neural networks are a computational attempt at modeling the information processing capabilities of nervous systems (Rojas, 1996). A typical model of the NN is shown in Figure 16.

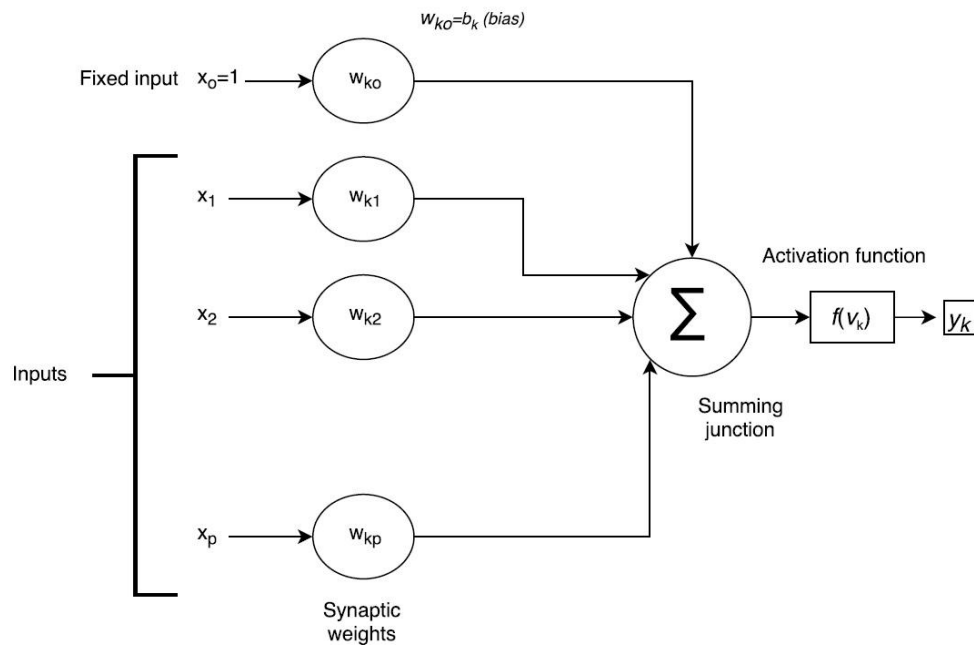


Figure 16: Non-linear neuron model

In the neuron model it is possible to identify three elements:

1. The synaptic weights indicate the strength of a connection between neurons.
2. Summing junction, is an added weight by the respective synapses of the neuron.
3. An activation function is used to limit the amplitude of the output neuron.

The mathematical model of a neuron can be written as (Hajek, 2005):

$$v_k = \sum_{i=0}^p w_{ki}x_i \quad (2.26)$$

With the output:

$$y_k = f(v_k) \quad (2.27)$$

The activation function determines the output associated with specific inputs. Different types of the activation function exist, some of them below:

1. Threshold activation function (McCulloch–Pitts model) is shown in Figure 17:

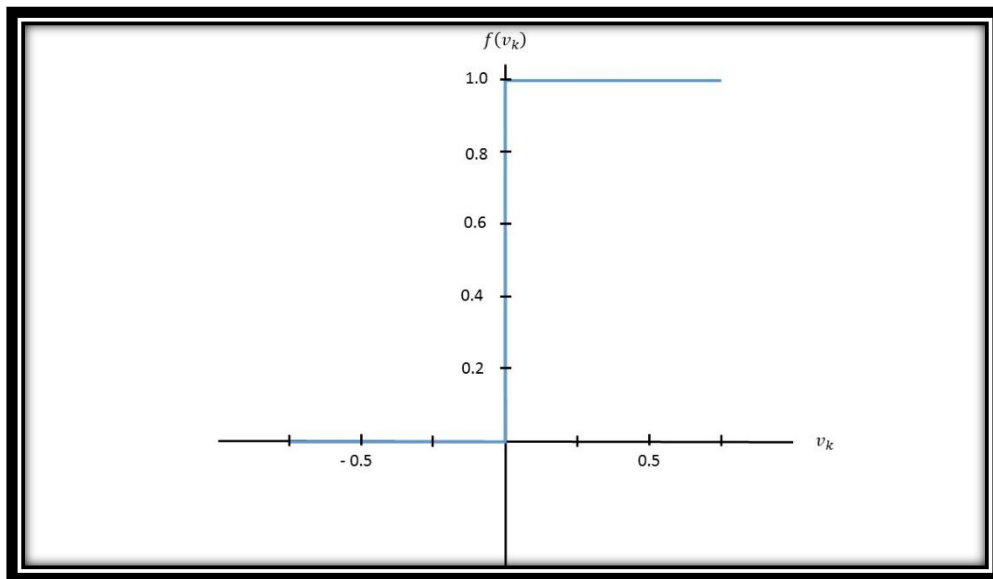


Figure 17: Threshold activation function

$$f(v_k) = \begin{cases} 1, & \text{if } v_k = \sum_{i=0}^p w_{ki}x_i \geq 0 \\ 0, & \text{otherwise} \end{cases} \quad (2.28)$$

2. Sigmoid activation function as illustrated in Figure 18:

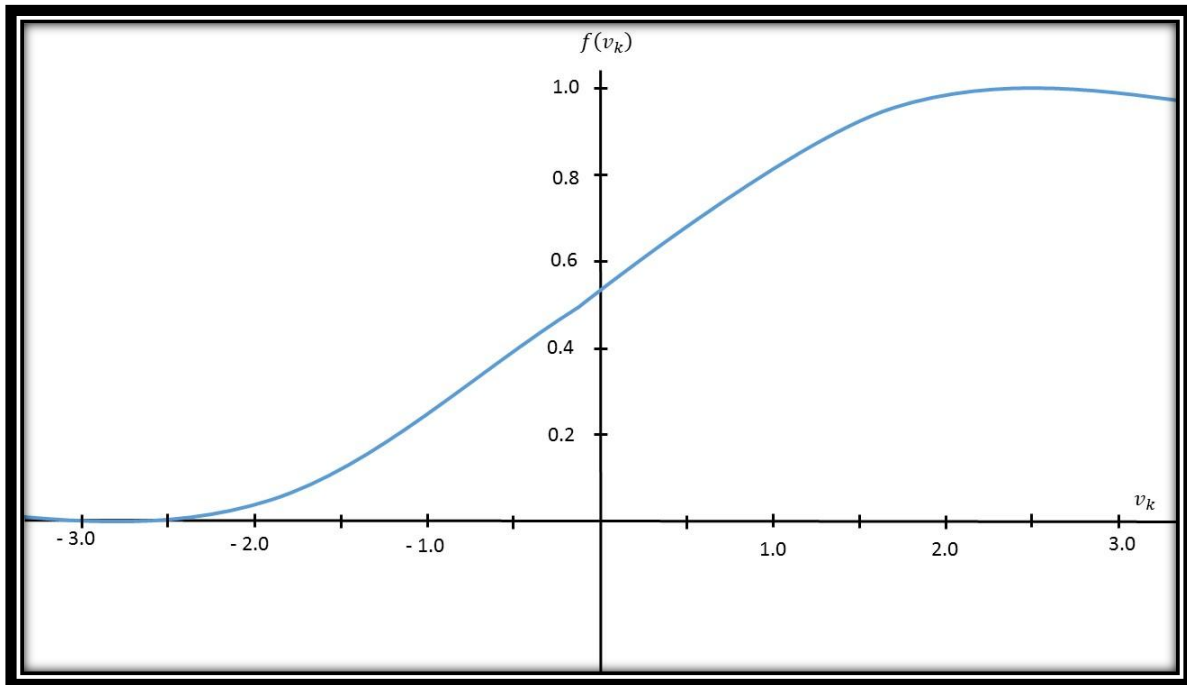


Figure 18: Sigmoid activation function

It is defined as:

$$f(v_k) = \frac{1}{1 + e^{-v}} \quad (2.29)$$

3. Hyperbolic tangent function

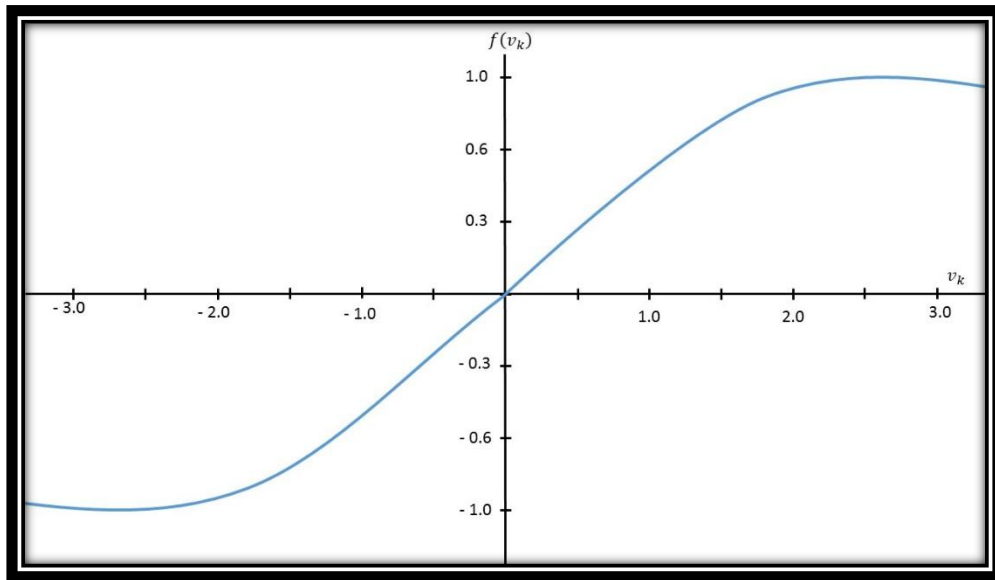


Figure 19: Hyperbolic tangent function

The definition of the hyperbolic tangent function is shown in equation (2.30). Equation (2.30) can be re-written as equation (2.31):

$$f(v_k) = \frac{e^v - e^{-v}}{e^v + e^{-v}} \quad (2.30)$$

$$f(v_k) = \frac{1 - e^{-2v}}{1 + e^{-2v}} \quad (2.31)$$

(Brandon Rhudy, 2008), used NN to differentiate impulsive events, such as artillery fire, and non-impulsive events, such as wind or aircraft noise. Cross correlation technique was implemented as feature extraction, and the NN algorithm was trained with different types of noise source as: tank main gun, mortar impact, hand grenade, wind noise, helicopter, etc. A total 2670 recordings were used. The result shows that NN produced a high precision to discriminate between impulsive events and non-impulse events. NN is an appropriate method when accuracy is more important than computational cost.

2.3.3.3 *K-mean*

K-mean is an algorithm to classify objects based on features into k number of clusters. The grouping is done by minimizing the sum of squares of distances between data and the corresponding cluster centroid (Teknomo, 2007). A simple algorithm for this classifier is shown in Figure 20:

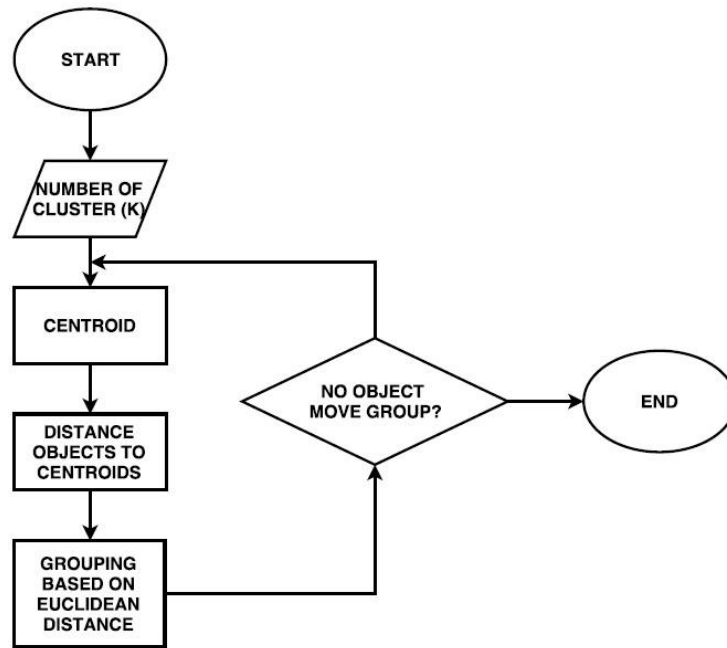


Figure 20: K-mean Block Diagram

1. The first step is to select the number of clusters "k".
2. Choosing the initial partition (centroids x_{si}, y_{si}) to classify "k" clusters data.
3. Compare each sample with the centroid of each cluster, the shortest distance indicated that belongs to that group. The Euclidean distance is used normally to determine the distances between pairs of the data. The Euclidean distance between to data points of the sampled signal (x_i and y_i) is defined as:

$$d_{(x,y)} = \sqrt{\sum_{i=1}^N (x_i - x_{si})^2 + (y_i - y_{si})^2} \quad (2.32)$$

4. When the clustering is done, the new centroid are determined with the average.

$$C_{k(x,y)} = \left(\frac{x_1 + x_2 + \dots + x_N}{N}, \frac{y_1 + y_2 + \dots + y_N}{N} \right) \quad (2.33)$$

Where $C_{k(x,y)}$ is the centroid of the k cluster, x_N are the values of the feature x , and y_N are the values of the feature y . N is the length of the data.

5. If the centroids value change, then repeat step 3.
6. If the centroids do not change, then done.

If the number of data points is less than the number of clusters, then we assign each data as the centroids of the clusters (Teknomo, 2007).

(Münz, et al., 2007), used the unsupervised K-mean method for the detection of anomalies in new monitoring data. The features used for clustering were: *the total number of packages, total number of bytes, and number of different source-destination*. These data were obtained of the flow records (2 minutes of recording) which are available in networks due to wide deployment of Cisco Netflow¹. In this case two clusters were created (k=2) normal traffic and anomalous traffic. The cluster creation process is called training. The next step is to take the new data, extract the features and by computing the Euclidean distance to each of the clusters centroid determine if it is a normal or anomalous traffic. The results show that K-mean algorithm can be used as detector for anomalous traffic and it has a low computational cost, therefore it can be implemented in real-time.

¹ Cisco IOS NetFlow efficiently provides a key set of services for IP applications, including network traffic accounting, usage-based network billing, network planning, security, Denial of Service monitoring capabilities, and network monitoring. NetFlow provides valuable information about network users and applications, peak usage times, and traffic routing. The information is available on: <http://www.cisco.com/c/en/us/products/ios-nx-os-software/ios-netflow/index.html>

CHAPTER III

METHODOLOGY

3.1 Artificial Thigh

With the main objective of detecting bubble size, an artificial thigh was built with a PZT ring placed around it, generating an acoustic chamber. The experimentally used acoustic glass chamber consisted of a Pyrex cylinder with 95 ± 0.4 mm OD and 300 ± 5 mm length (Pyrex 7740, Ace Glass, Vineland, NJ) and an inner cylinder with 20 mm OD and 300 mm in length made of a material that mimics human bone (3403-09, Sawbones, Vashon, WA). The vein and artery were vinyl tubes with (7.94 ± 0.16 mm and 6.35 ± 0.1 mm OD respectively). The PZT ring has the following specifications (BM400, Sensor Technology Ltd., Canada): was radially polarized with 110 ± 0.1 mm OD, 98 mm ID, and 25.07 ± 0.8 mm height. The BM400 material is equivalent to Navy PZT Type IV materials (Sensor Technology, Collingwood, ON, Canada). The PZT ring was placed to around the glass cylinder and was glued with Stycast 1264 (Emerson & Cumming, Billerica, MA) epoxy, cured at room temperature. Three piezoelectric discs (C-5400, Santa Barbara, CA), were glued to the glass cylinder to 0 cm, 1cm and 2 cm from the bottom edge of the PZT ring.

Using the simulated simplified human thigh, the objective was the detection, and characterization of the micro bubbles. The acoustic chamber was filled with distilled filtered water.

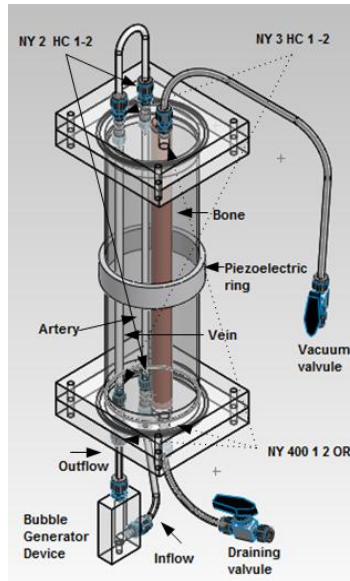


Figure 21: Acoustic Chamber.

The acoustic chamber (Figure 21) should be filled with degassed water while at vacuum pressures of approximately 5-6 Torr. This procedure prevents the formation of random bubble nucleation, allowing for a better characterization of the system (Valentin, 2012).

When the process is completed, a gas free acoustic chamber is ready for a frequency response analysis with the objective of determining its resonance frequency.

3.2 Bubble Generating System

A bubble generating system (Figure 22) is used to introduce bubbles in the artificial thigh and it is composed by 33 gauge needle with a point style number 3 (91033, Hamilton Company, Reno, NV) connected to a luer connector. Figure 22A shows a piece of acrylic that has a 120 mm length to drive bubbles into the artificial artery.

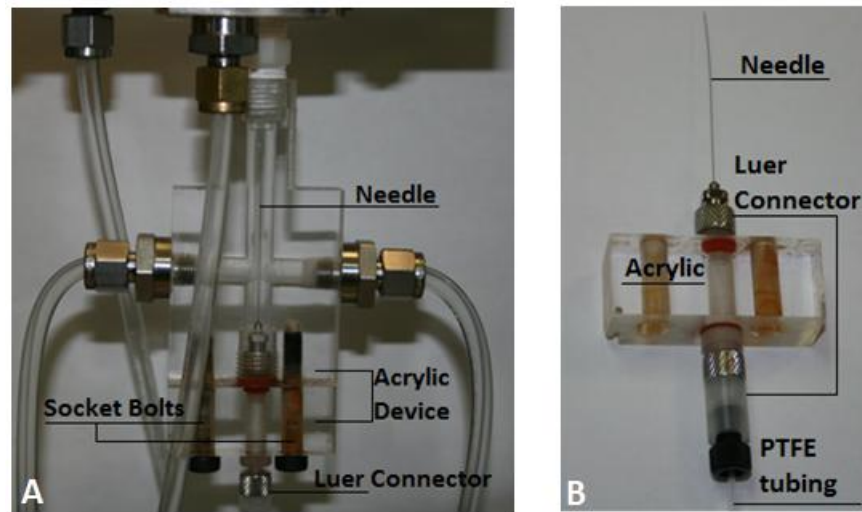


Figure 22: Bubble generator device.

Figure 22B shows the connections of the needle with the luer connector and a small piece of acrylic. Each piece is used such as convertor between luer connector to PTFE tubing. Each tubing is connected with a Valve (86580, Hamilton Company, Reno, NV).

An electro-valve that is a single solenoid 3 way 1 position, normally closed (EZ1GNBBG49A, Richland, MI), and syringe pump (NE-1000, Farmingdale, NY), were used such as a control system (see Figure 23) to manage the volume of the minimum air induced to create one bubble into the acoustic chamber.

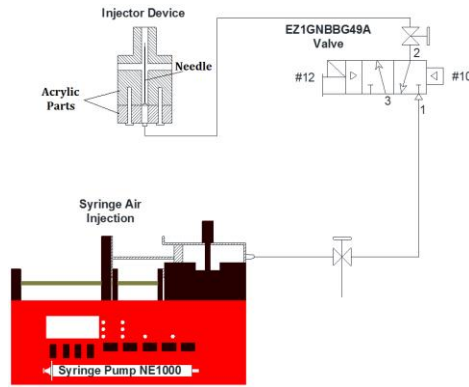


Figure 23: Bubble generator system.

The electro valve is controlled by a program developed in Labview. The Labview algorithm is illustrated in Appendix 7.1.

The voltage required to operate the solenoid is 24 VDC. However the 24 VDC cannot come from the NI6356 card port (Described in section 3.4). In the above, the solenoid must be controlled with a circuit to operate power systems with low voltage signals. The following diagram (Figure 24), which illustrated an integrated circuit "L293" (used as a power converter), was implemented.

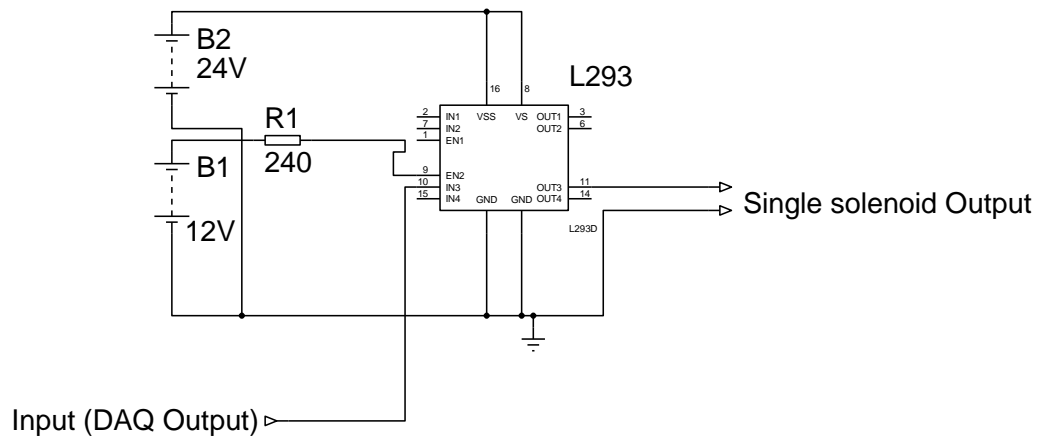


Figure 24: Power converter diagram.

3.3 Degassing Protocol

Initially, three liters of filtered deionized (Milli-Di, EMD Millipore, Merck KGaA, Germany) water in Erlenmeyer flask were magnetically stirred (11-100-100S Isotemp, Fisher Scientific, Waltham, MA) to promote off-gassing while a continuous vacuum that was applied by a vacuum pump (8890A, Welch, Niles, IL) for 45 minutes. Before filling the prototype, it is necessary to apply vacuum. Vacuum pressure was measured with a digital pressure gauge (68936-80,760 torr, Cole Parmer, USA). The Erlenmeyer was previously coupled to a closed valve named inlet 1 in Figure 25, it valve connect the artificial thigh with the Erlenmeyer. When the degassing it's done, the valve inlet 1 is open to fill the prototype.

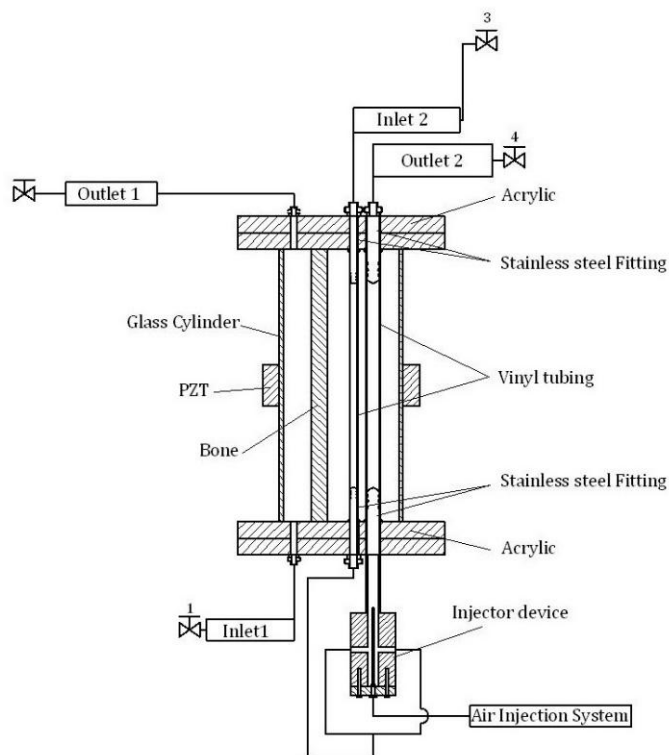


Figure 25: Prototype scheme.

Finally, the prototype was filled with approximately 2 liters. The next step was to close the inlet 1, and the connections of the Erlenmeyer's output were connected to inlet 2. The vacuum flask was removed, and the vein and artery were filled with the leftover water.

3.4 Data Acquisition

3.4.1 Voltage divider

A signal generator (3312A, Hewlett Packard Company, Palo Alto, CA) was connected to a PZT amplifier (EPA102, Piezo Systems Inc., Cambridge, MA).; the voltage from this device was 10 Volts peak to peak (Vpp) . When the signal passed through the amplifier, it was amplified 20 times, making the signal transmitted to the PZT ring 200 Vpp. Through a voltage divider, which attenuated the signal 10.09 times (Figure 26), the voltage (20 Vpp) and current (250-270 milli-amperes peak to peak (mApp)) signals were displayed on the oscilloscope.

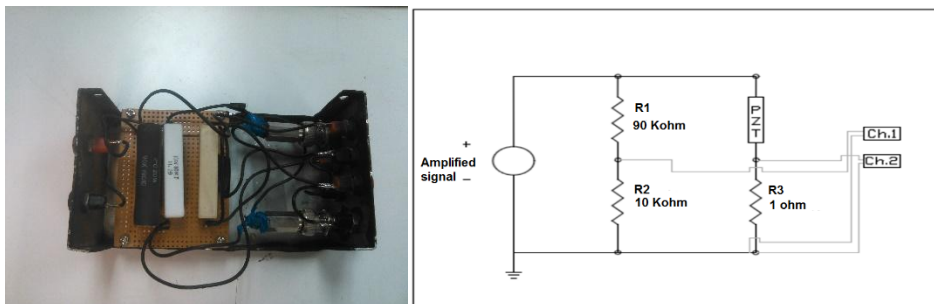


Figure 26: Voltage Divider A. implemented B. Electrical circuit.

The oscilloscope (54615B, Hewlett Packard Company, Palo Alto, CA) and signal generator were connected via a GPIB² (488.1, NI, Austin, TX) device to a computer.

3.4.2 Frequency response

A program developed in Labview was used to measure the frequency response (Appendix 7.2); this program acquired current and voltage signals from the PZT and computed the electrical admittance of the PZT ring as a function of frequency.

Electrical admittance is a complex quantity; its real part corresponds to the conductance of the PZT ring, the maximum conductance coincides with the mechanical resonance (Cancelos, et al., 2005).

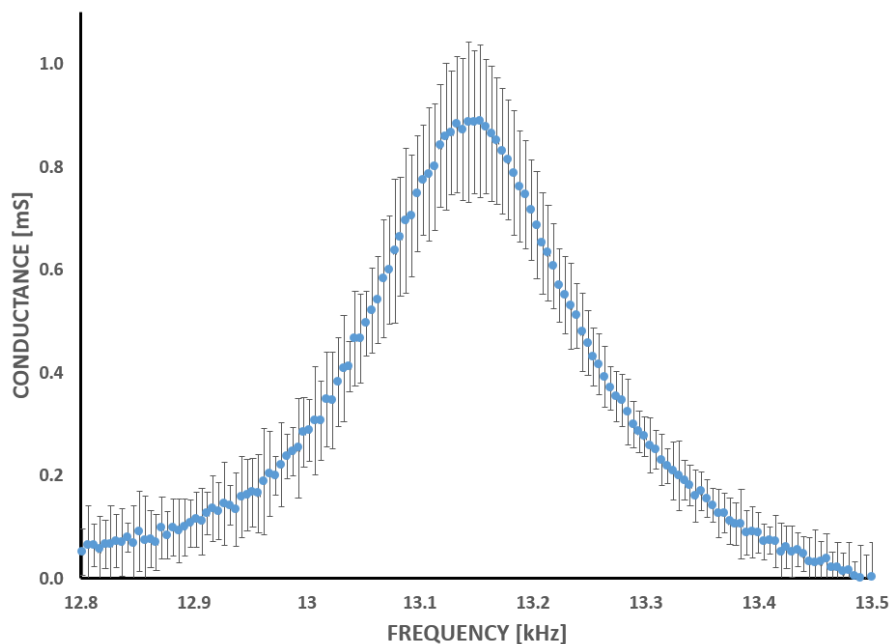


Figure 27: Frequency response of the acoustic chamber.

² GPIB: (General Purpose Instrumentation Bus), transforms any computer with a USB port into a full function, plug and play IEEE 488.2 controller for up to 14 programmable GPIB instruments.

A typical frequency response is shown in Figure 27, where the resonance frequency was $(13,158 \pm 40)$ Hz. The frequency response should always be found prior to performing the experiment because it changes with environmental conditions.

With the measured resonance frequency, the signal generator was configured to generate a sinusoidal signal at this frequency, resulting in the formation of a standing wave in the acoustic chamber. When the acoustic chamber was excited with a frequency that matched its first resonant mode, any minor disturbance in this medium was a measurable response through the PZT ring. Disturbances in this acoustic chamber were associated with the bubbles that were introduced into the system.

3.4.3 Data acquisition card

The data acquisition card (NI 6356, National Instruments Corporation, Austin, TX) is a device capable of operating its eight analog channels at a sampling frequency of 1.25 MHz (National Instruments, 2009-2010). It also has two output analog channels and twenty-four digital channels of input and output (inputs and outputs are controlled by software). This device was configured to receive signals from the PZT ring using 5 analog channels. A picture of the DAQ is shown in Figure 28.

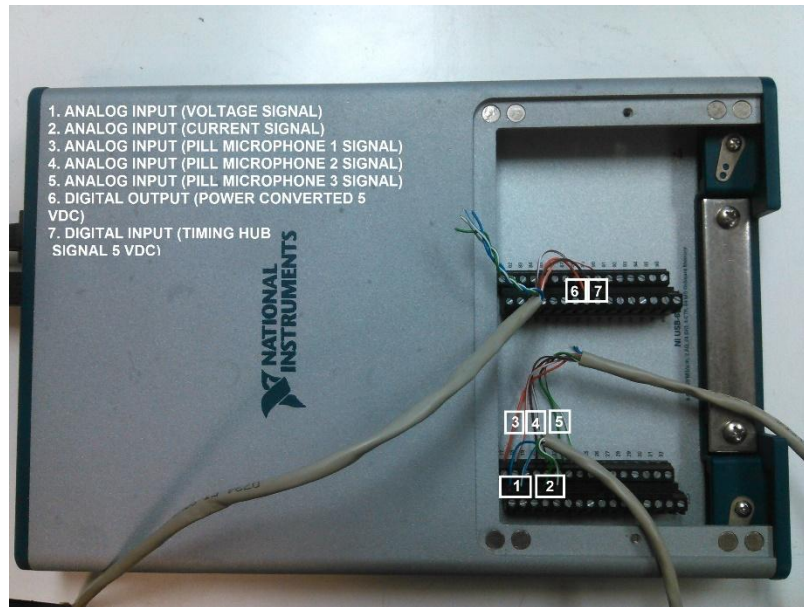


Figure 28: Data acquisition card NI 6356.

Figure 29 shows a typical electrical current measured from the PZT and the effect of a passing bubble through it. Two different methods were used to analyze the electrical signals acquired from the PZT. In “method 1” the PZT was activated continuously while the bubbles were introduced into the system. The sample rate used to acquire data was 1 MHz, and the total time recorded was 20 seconds (20 Million sample data), initially capturing the first 10,000 samples of the signal which has no bubbles. In this data set, the absolute value and then the value of maximum amplitude of each semi cycle is obtained (see the Figure 66, Appendix 7.4.1).

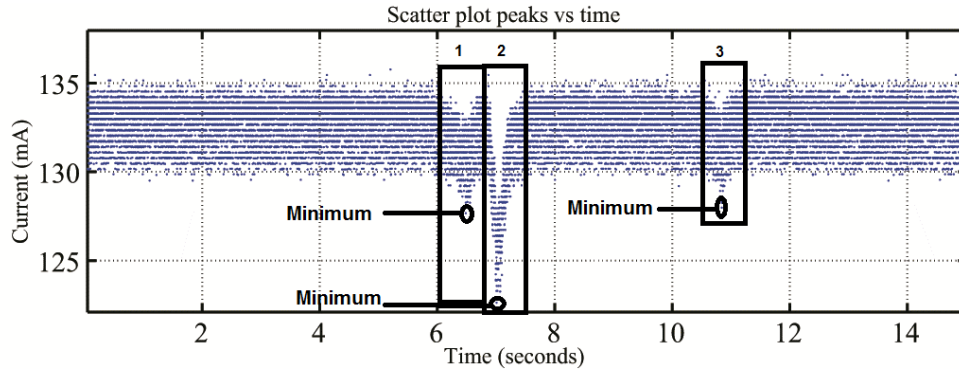


Figure 29: Method 1 for acquired data was used for this case.

In order to find the current drop, an algorithm was developed to determine the minimum peak when the current drops due to the presence of a bubble crossing the PZT ring (see the Figure 67, Appendix 7.4.1).

The operation of the algorithm is:

1. From the peaks obtained in the algorithm of the Figure 66, the “ $z_{[n]}$ ” variable is created with samples than: $y_{[n]} < threshold$. The goal is obtain only peaks from the signal.
2. The threshold is determined with the following equation:

$$Threshold = \overline{y_{[n]}} - \sigma_{y_{[n]}} \quad (3.1)$$

With,

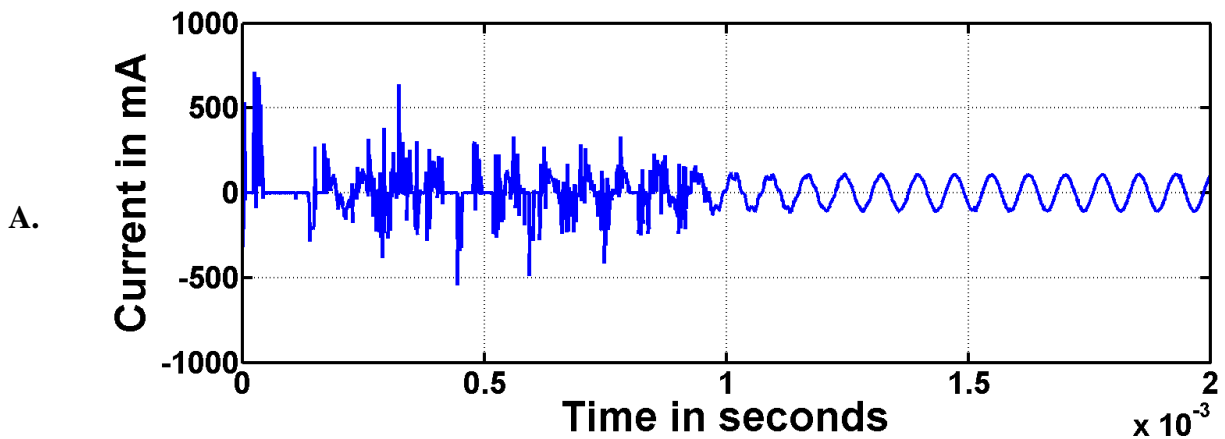
$$\overline{y_{[n]}} = \left(\frac{1}{10000} \sum_{i=1}^{10000} Amplitude_max_i \right) \quad (3.2)$$

$$\sigma_{y[n]} = \sqrt{\frac{1}{(9999)} \sum_{i=1}^{10000} (y_i - \overline{y[n]})^2} \quad (3.3)$$

3. When the samples from “ $y[n]$ ” is: $y[n] > threshold$, the minimum value of the variable “ $z[n]$ ” is calculated.
4. Calculate current drop as:

$$Current_drop_{(n)}[\%] = \frac{|y(n) - Amplitude_min_{(n)}|}{y(n)} (100\%) \quad (3.4)$$

However, when the PZT was turned on, some bubbles were broken into smaller ones, whereas in some cases, they coalesced and in other cases, they continued oscillating close to the PZT without crossing it. From the above it was necessary to keep the PZT off in order to allow the bubbles to reach the middle of the acoustic chamber. After assuring this, the PZT is turned on. This permitted the control of the measurement of the bubble, the above method is called “method 2”.



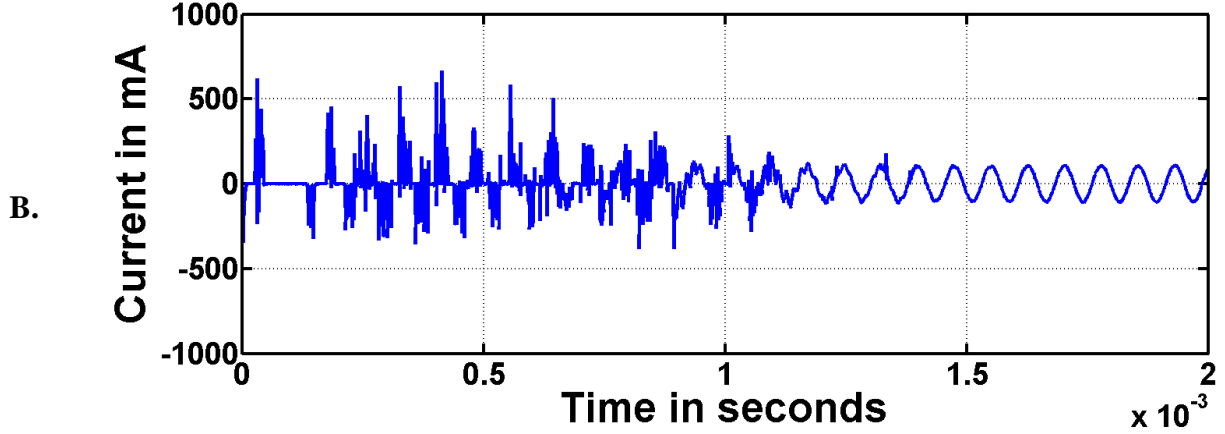


Figure 30: Electrical signal from the PZT. Method 2 for acquired data was used for this case. A- Signal current without bubble. B- Signal current with bubble.

In method 2, it is necessary to acquire a reference signal as illustrated in Figure 30A (signal current without bubbles inside the acoustic chamber), and then acquire the current signal with induced bubbles into the acoustic chamber (Figure 30B).

Experimentally, it was observed that the transient signal was between 9.5 ms to 10.8 ms. if the sampling frequency is 1 MHz; it means that approximately the first 10000 data points contain the transient part of the signal. Typically, signals in telecommunications are composed of the signal that carries the information, and the noisy signal (Borrion, 2006). In our case, the electrical signals from the PZT “ $S_B(n)$ ” are shaped by the transient “ $t_{SB}(n)$ ”, and stationary signal “ $s(n)$ ”.

$$S_{B(n)} = t_{SB(n)} + s(n) \quad (3.5)$$

Experimentally, a stationary signal without bubble “ $S_{NB}(n)$ ” and a stationary signal with bubble “ $S_B(n)$ ” were processed without finding any difference in them. Both signals (with and without bubbles) have the same amplitude. These signals can be expressed as:

$$S_{B(n)} = t_{SB(n)} + s(n) \quad (3.6)$$

$$S_{NB(n)} = t_{SNB(n)} + s(n) \quad (3.7)$$

When equation (3.6) is subtracted from equation (3.7), the differential between electrical signals with bubble and without bubble is:

$$S_{NB(n)} - S_{B(n)} = t_{SNB(n)} - t_{SB(n)} \quad (3.8)$$

This deduction indicates that the difference between the signals with $S_{B(n)}$ and $S_{NB(n)}$ is given by the transient signals. In order to identify the above difference between $S_{B(n)}$ and $S_{NB(n)}$, the root mean square was used for both signals and compared using the relative value. The equation for this process is:

$$Relative\ value\ [\%] = \frac{|SNB_{RMS(n)} - SB_{RMS(n)}|}{SNB_{RMS(n)}} (100\%) \quad (3.9)$$

The algorithm developed for method 2 is shown in Appendix 7.4.2.

3.5 High Speed Cameras

To perform a comparison between the electric signals on the PZT and the bubbles that were introduced into the system, two high-speed cameras (Speed Sense 9040 and Speed Sense 9090, Dantec Dynamics, Skovlunde, Denmark, DK-2740), hereafter called camera 1 and camera 2, Speed Sense 9040 and Speed Sense 9090 respectively, were implemented in the process. Additionally, two LEDs (19 LED constellation systems and constellation 120, Tallahassee, FL) called LED 1 and LED 2, respectively, were used. The image of the bubble leaving the bubble generation device provided the size of the bubble (camera 1), and the image of the bubble about to cross the PZT (camera 2) allowed the identification of the current drop associated with the particular bubble studied. The settings for the cameras recording were:

	CAMERA 1	CAMERA 2
	(9040)	(9090)
SAMPLE RATE	100	100
NUMER OF THE IMAGE	2000	2000
RESOLUTION IN AXIS X	800	1200
RESOLUTION IN AXIS Y	600	800
PIXEL DEPTH	8	8

Table 1: Setup for the high speed cameras.

Three bubbles of the bubble generating system are shown below:

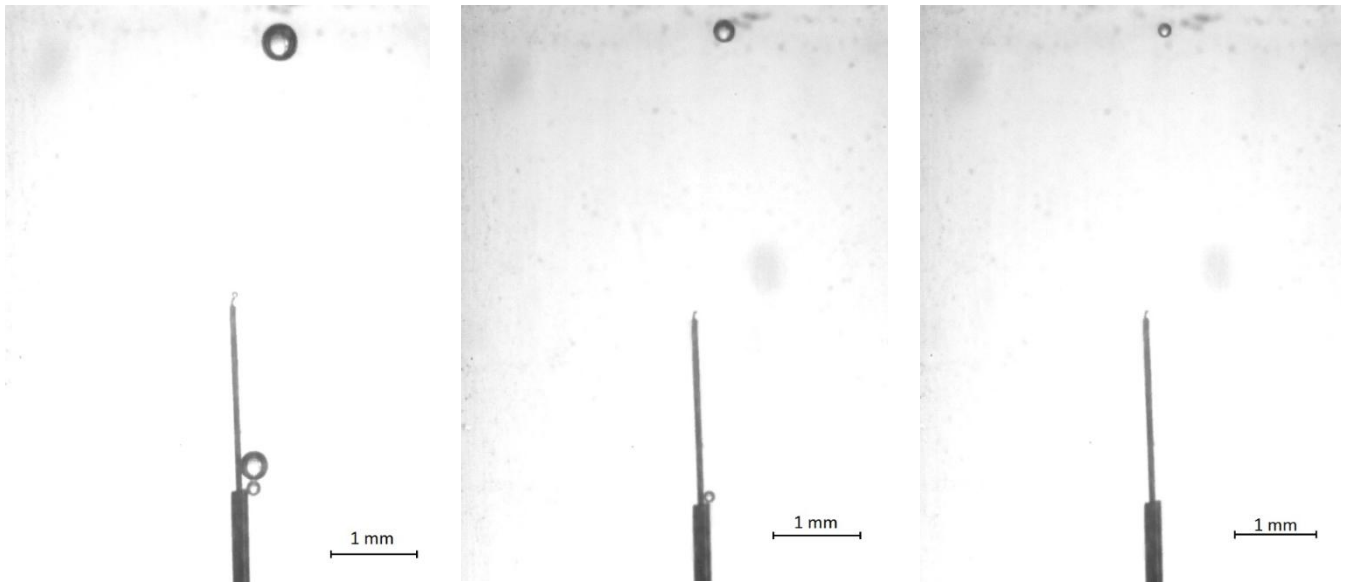


Figure 31: Bubbles in the bubble generator. Images captured with camera 1.

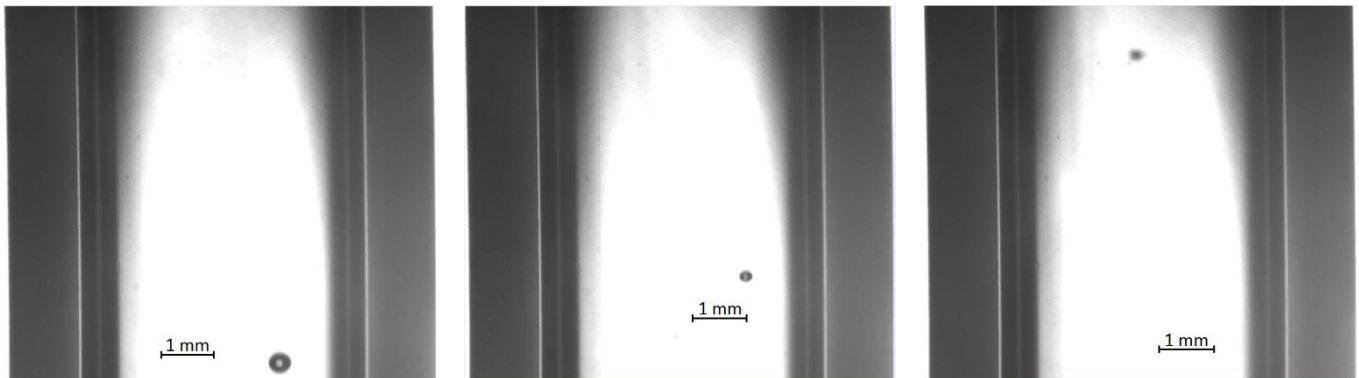


Figure 32: Images captured in the camera 2.

The images in Figure 31 and Figure 32, are images of the camera 1 and 2, respectively. Through *Dynamic Studio* software, the image processing was performed by the shadow processing function. Through it, the bubble diameter recorded throughout the video was determined. Figure 33 shows the histogram of micro bubbles upon activation of the bubble generator system:

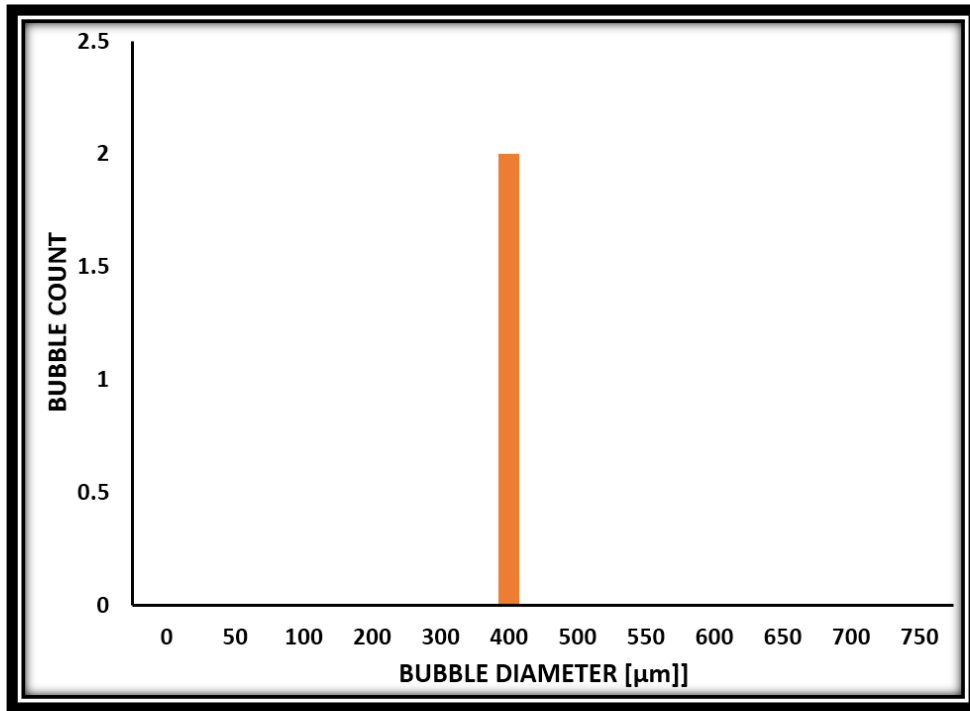


Figure 33: Histogram of the microbubbles from the needle.

Usually the generation of micro bubbles produced a population between 4-6 micro bubbles, the first to rise being the biggest bubble due to highest buoyancy. This bubble was the one used as a guide to enable the PZT. The Figure 34 shows the histogram from the artery.

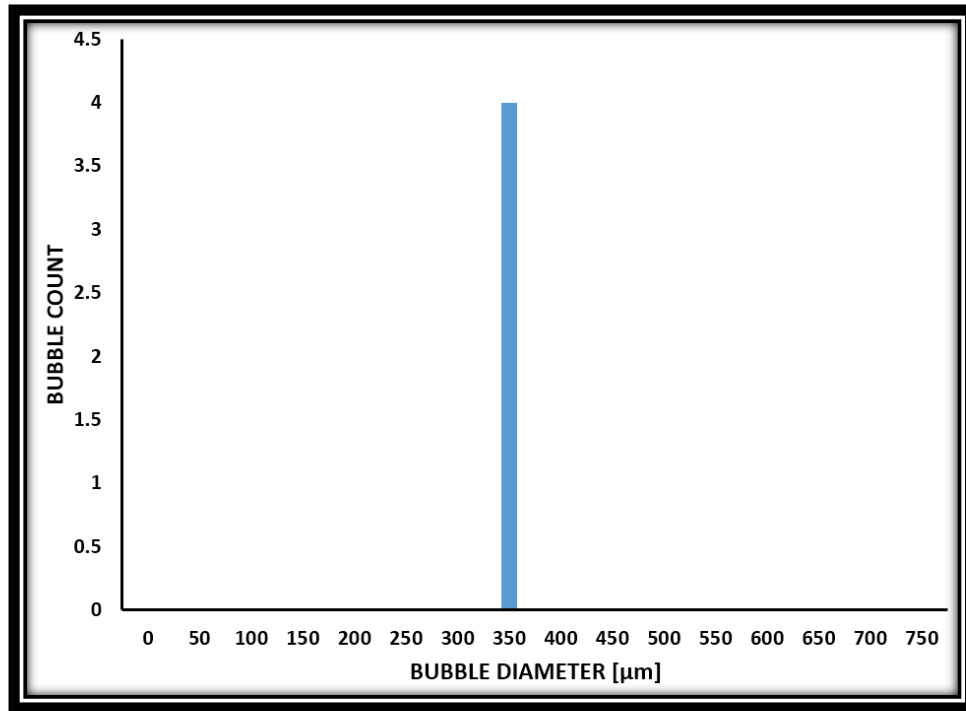


Figure 34: Histogram of the microbubbles from the artery.

3.6 Timing hub

The high speed cameras were synchronized with the NI6356 card, since both devices were needed to estimate a relationship between the images of bubbles saved and the signals detected through the PZT ring.



Figure 35: Timing hub device.

The synchronization of the devices previously mentioned (NI 6356, high speed cameras and LEDs) was performed with the timing hub (Figure 35). This device used external or internal inputs as triggers. The timing hub had eight output ports. The configurations of the input and output ports (Figure 36) were performed through *Dynamic Studio* (Version 3.14.35, Dantec Dynamics, Skovlunde, Denmark).

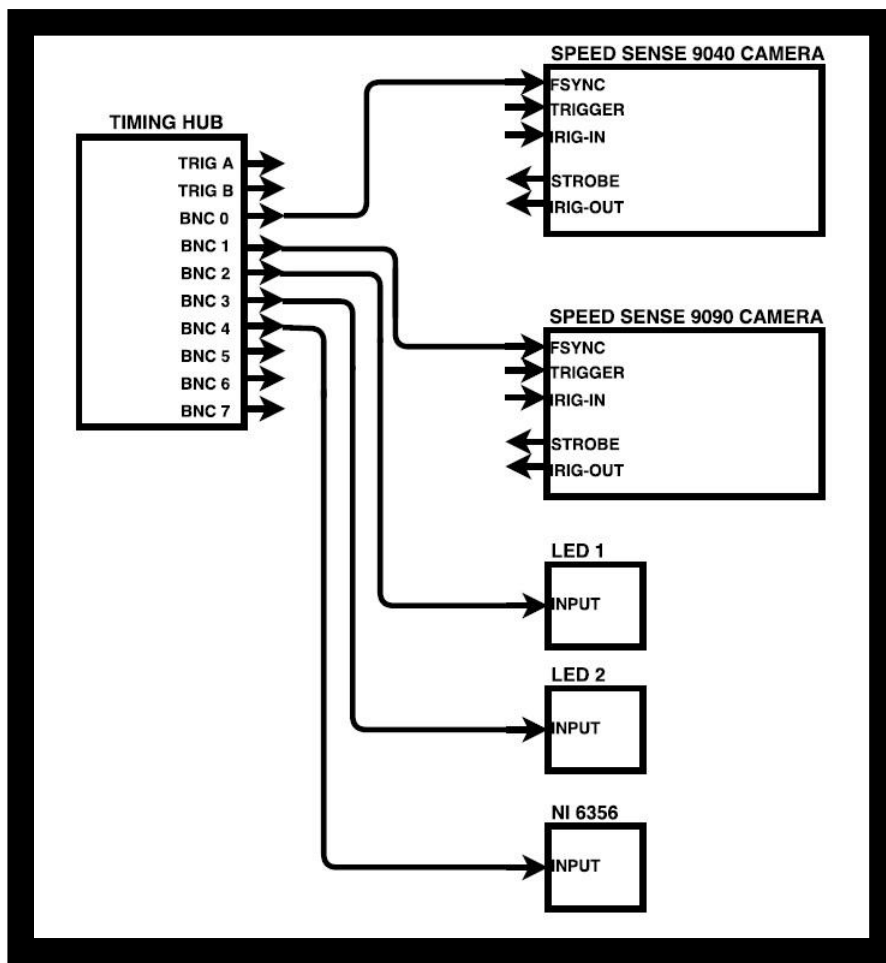


Figure 36: Timing hub settings from Dynamic Studio.

The synchronization signal sent through the timing hub was 5 VDC (Figure 37); this is a square signal, and the frequency can be controlled using an external device as a signal generator (manual mode), or the frequency signal can be emitted from the timing hub (automatic mode). Both options can be chosen in the *DynamicStudio software*. The first signal emitted was a rising edge to the output port.

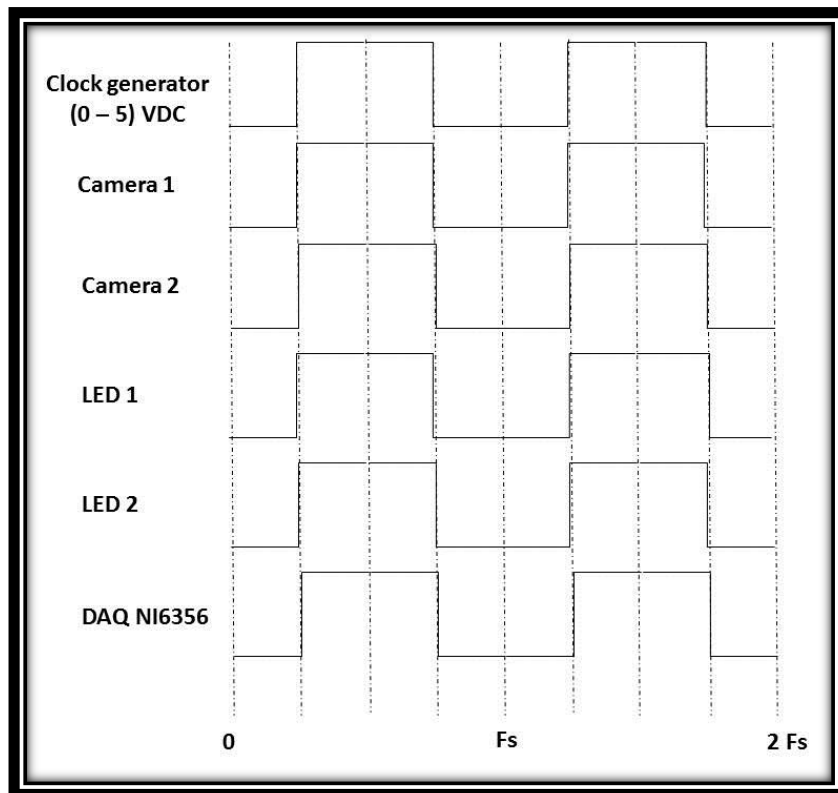


Figure 37: Timing hub diagram.

3.7 Experimental Protocol

A wave generated a signal that was induced into the prototype. This signal was observed by the oscilloscope. Both devices were connected via GPIB. The interface connection between computer, signal generator, and the oscilloscope were connected via GPIB by USB.

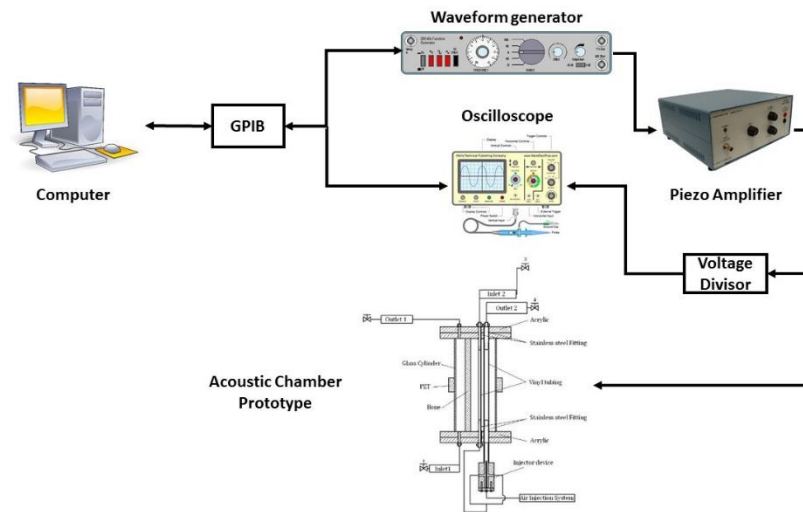


Figure 38: Experimental setup #1.

When the frequency response was found (with the experimental setup #1, see Figure 38), the waveform generator was tuned to the resonance frequency.

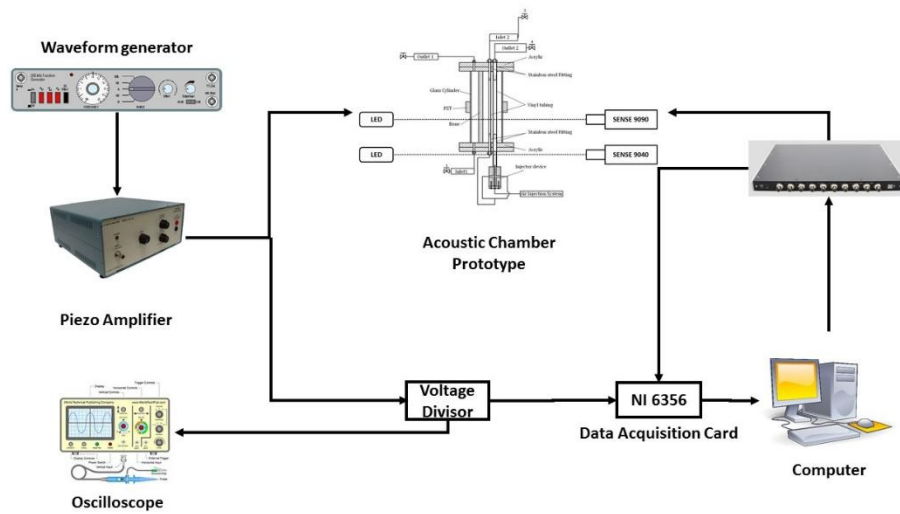


Figure 39: Experimental setup #2.

The next step to activate the bubble generator system to recreate decompression sickness in the prototype. When activated, the timing hub started recording using the high-speed cameras and the data acquisition card (Figure 39). When the bubble was close to the PZT, the PZT was activated.



Figure 40: Experimental set-up.

Figure 40 shows the real devices used for bubble detection in the Bubble Dynamics Laboratory.

3.8 Implementation of Classifiers

From section 3.6, the relationship between current drop and bubble diameter was obtained. These samples (electrical signals from PZT, MP1, MP2 and MP3) are the inputs to classifiers, and the samples of the high speed cameras are the references to determine the range of the classes. The following table shows the input data which is read by the classifier algorithm:

Relative value [x]	Target [y]
4.3	0
6.4	0
3.2	0
4.3	1
2.1	0
3.7	0
1.2	0
4.3	0
0.6	0
3.2	0
5.5	0
7.5	1
6.3	1
5.6	1
5.5	1
3.5	0
2.4	0
6.4	1
4.9	0

Table 2: Example of the input data to classifiers.

3.8.1.1 Support vector machine

The training step begins when the relative values are induced as features “x” of the equation (2.17) to determine the hyperplanes. To find the margin, equation (2.23) is used. Finally, the weights “w” must be minimized to maximize the separability between the classes “y” (equation (2.24)).

The algorithm was implemented with MATLAB software (Appendix 7.5). The toolbox used in MATLAB applied kernel functions. The linear kernel was implemented, expressed as:

$$k(x_i, x_j) = x_i^T x_j \quad (3.10)$$

In order to determine the classification for the new data, the sum of similarities is computed:

$$Predict = \operatorname{sgn} \sum_{i=1}^N w_i y_i k(x_i, x_j) \quad (3.11)$$

With,

Predict ; kernel classifier predict label to unlabeled inputs.

sgn ; it is an odd mathematical function that extracts the sign of a real number.

w_i ; weights obtained from the training data.

y_i ; the targets obtained from the training data.

3.8.1.2 Artificial Neural Networks

Table 2 is an example of the input data in which neural networks algorithm receive for processing. The NN toolbox of the *MATLAB software* was used (Appendix 7.6). Initially, the inputs are used as training data, with inputs and targets known. The weights and bias (the initial value of the bias “b” is zero) are detected, to which the error between update targets and estimate targets is zero. The expression to calculate the weights is:

$$weight_{new(i+1)} = weight_{old(i)} + y_i * x_i \quad (3.12)$$

The output expression when the update has been induced can be shown as:

$$output_i = weight_{new(i)} * x_i \quad (3.13)$$

The iteration is done if the calculated error between the “ $weight_{new(i+1)}$ ” and “ $weight_{old(i)}$ ” do not change.

3.8.1.3 K-mean

The relative value of the bubble diameter was used because this method generates data clustering. When the cluster has been determined, an algorithm was developed (Appendix 7.7) to predict the new samples. Each sample is joined to each cluster. The standard deviation is calculated also for each cluster, the minimum variation indicates which said sample belongs to these clusters.

CHAPTER IV

EXPERIMENTAL RESULTS

4.1 Result obtained from the features extraction

4.1.1 Bubble in middle of the PZT ring

The relative values obtained from the equation (3.9) in the section 3.4.3 and bubble size diameter obtained in the section 3.5 from bubbles crossing the PZT ring generate a relationship shown below in Figure 41.

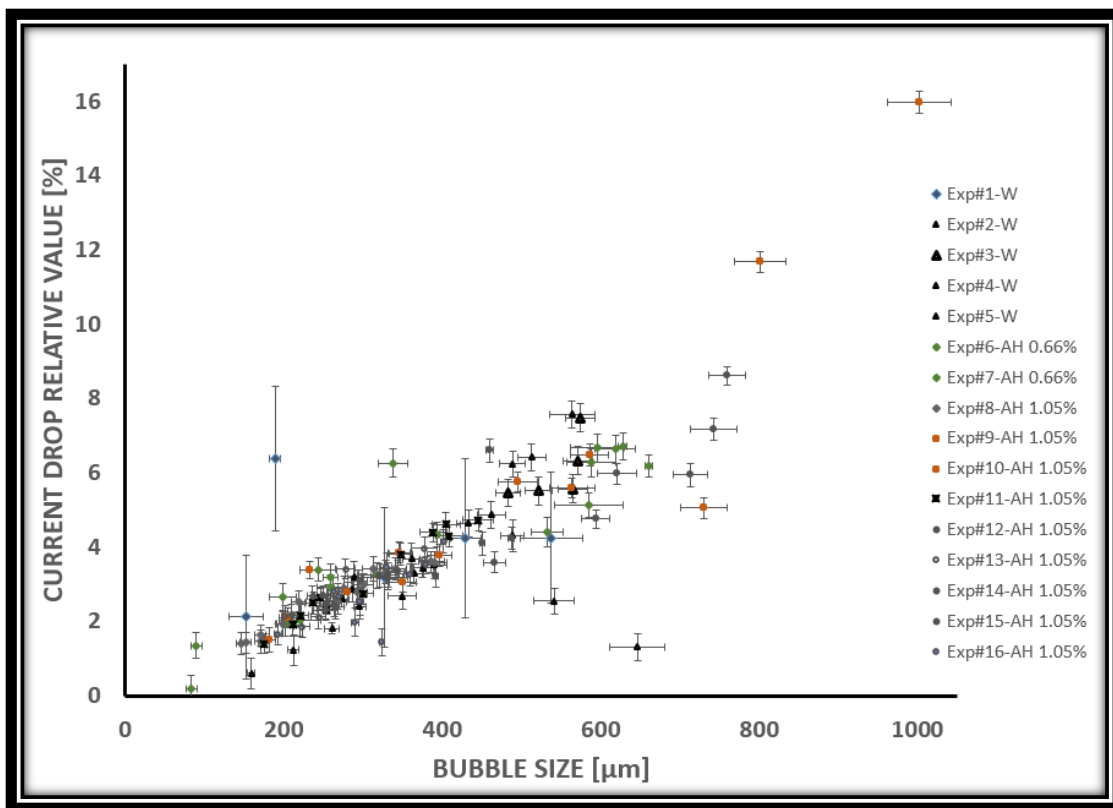


Figure 41: Effect of bubble size measured in the PZT when it is actuated at the time the bubble reaches the PZT center. Number of samples =126.

The error bars were computed, based on the DAQ card precision and the error propagation of the relative value of the difference in root mean square.

Not having a linear relationship, the next step was divide the curve of the Figure 41 into different intervals. Initially, this curve was divided into two ranges: bubbles larger than 500 microns and small bubbles under than 500 microns. In others word, the step “one” has a setup as: interval’s range is 500 μm and the number of ranges is 2. The second step is changing the range intervals to 200 μm , which increases the number of ranges to 5 (The K-mean algorithm was used to determine the number of classes). In order to compare the accuracy and error of the algorithms to find the best in the bubble detection, the confusion matrix was implemented.

In order to take advantage of other observations and improve the estimate in the detection of bubbles, the signals captured by the microphones were also processed obtaining relative value from the voltage microphone and bubble diameter as shown in Figure 42:

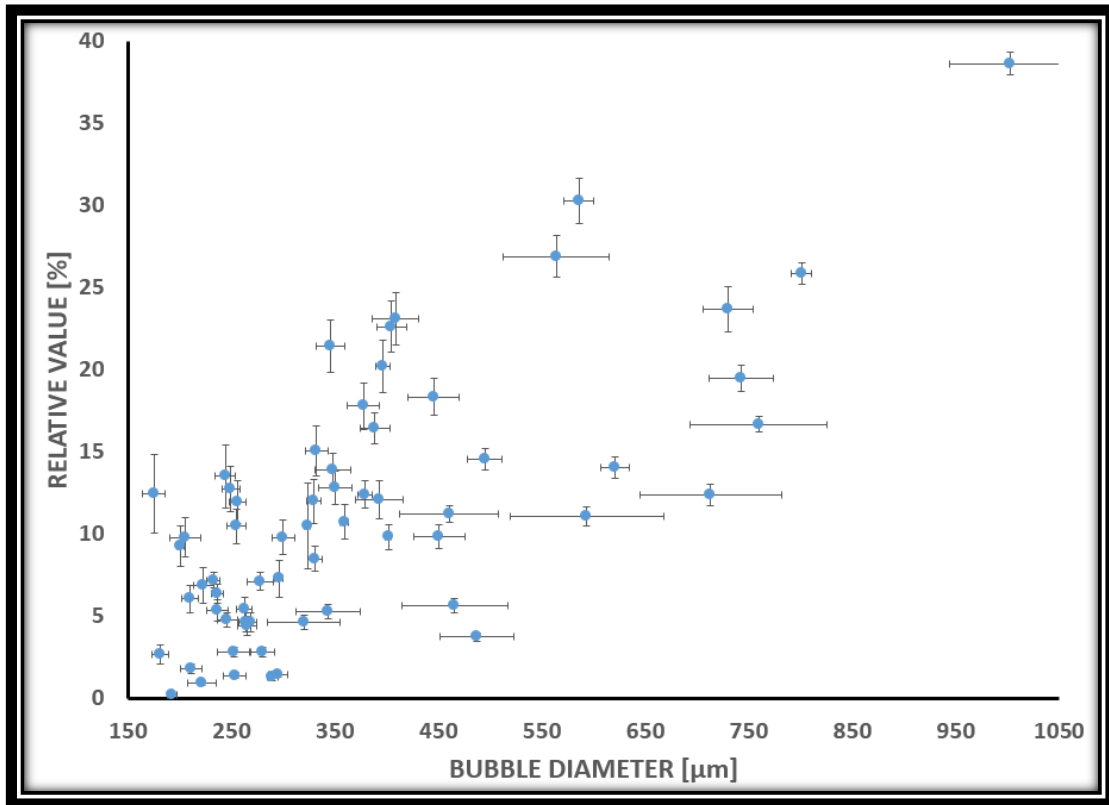


Figure 42: Data obtained by measuring the voltage in a pill microphone located at the bottom edge of the PZT when the PZT was actuated when the bubble reached the PZT center. Number of samples = 63.

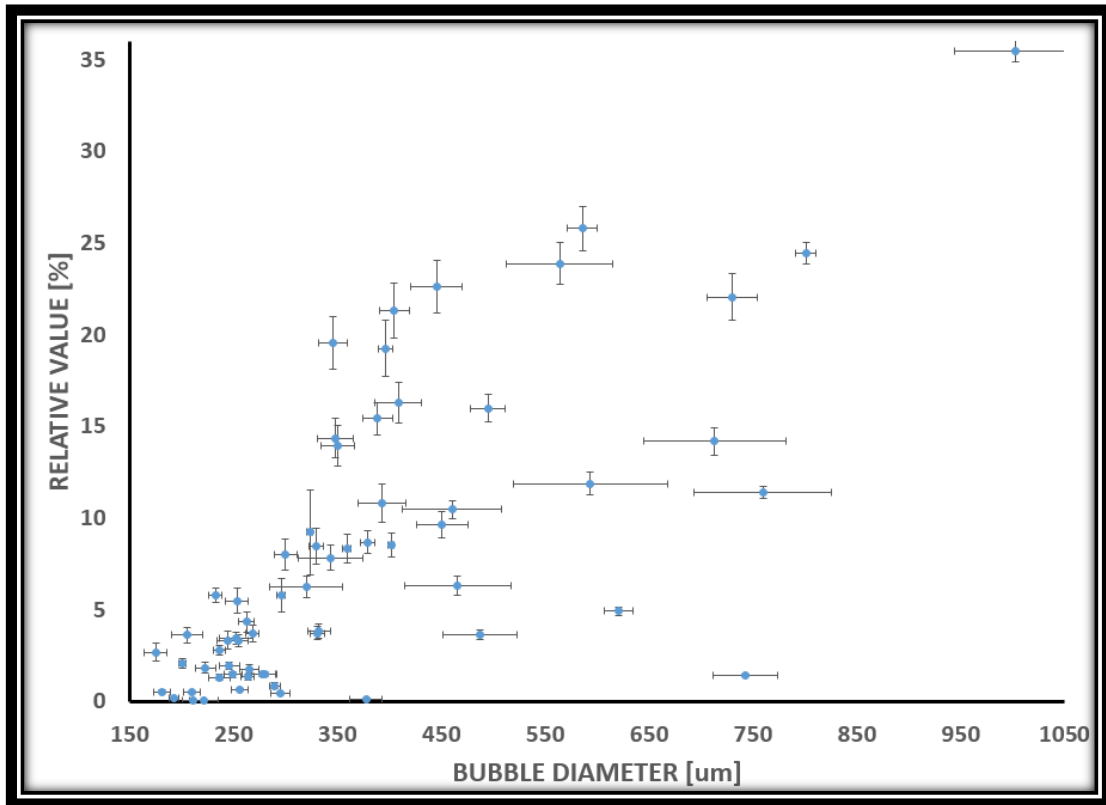


Figure 43: Data obtained by measuring the voltage in a pill microphone located 2cm from the bottom edge of the PZT when the PZT was actuated when the bubble reached the PZT center. Number of samples =63.

In summary, the data obtained when the bubble crosses through the PZT are:

- Electrical signal from PZT ring with 126 samples.
- Electrical signal from "MP1" with 63 samples
- Electrical signal from "MP2" with 38 samples.
- Electrical signal from "MP3" with 63 samples.

The differences are due to the fact that some tests were carried out with microphones at 0 cm, 2 cm and 4 cm from bottom edge of the PZT, while others were changed to 0 cm, 1 cm and 2 cm. When it was observed that the PZT bubbles were not detected beyond 2 cm (Figure 48), the

microphone signal acquired at 4 cm was suppressed. However, the microphones signals common for all test are PZT, MP at 0 cm and MP at 2 cm.

4.1.2 Bubbles located 1 cm from the PZT ring

When thinking about applying the "Method 2", it is important to consider a new condition. If the system will detect the bubbles by operating the PZT randomly, is necessary to determine the minimum distance for bubble detection. In order to find the PZT ring sensitivity, some tests were performed actuating the PZT to 1 cm from its bottom edge. Figure 44 shows the relative value ratio and bubble diameter from the PZT ring:

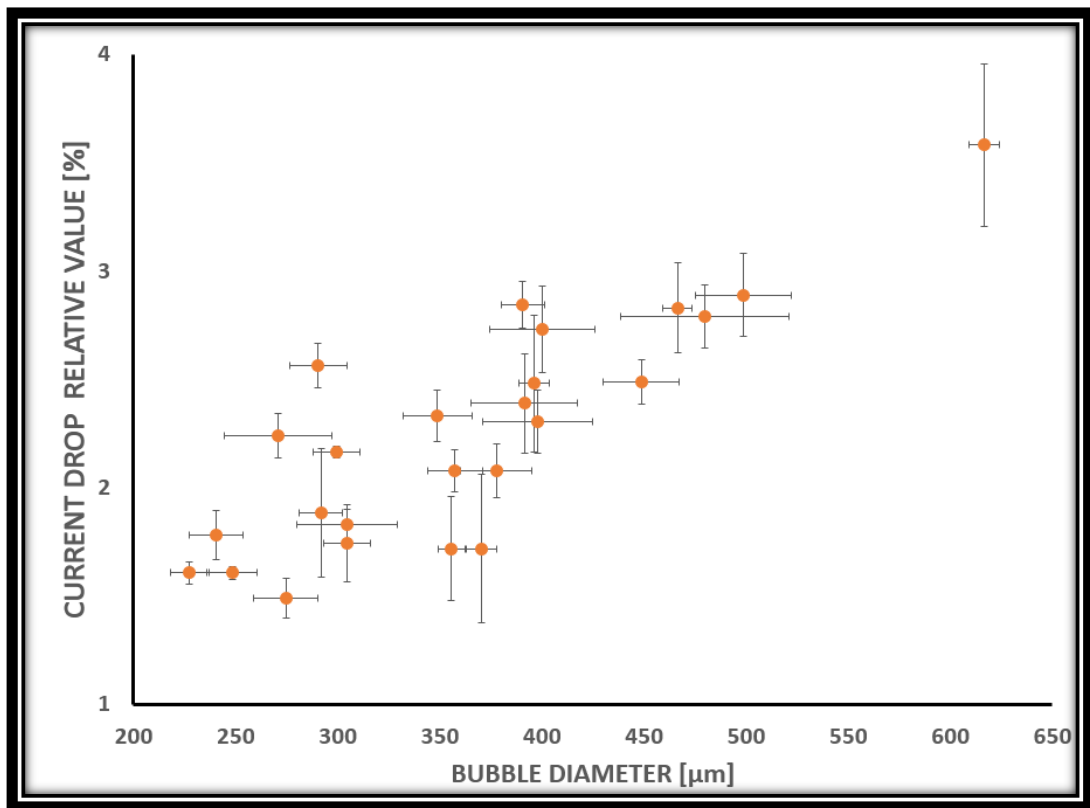


Figure 44: Data obtained when the PZT was actuated when the bubble was located at 1cm from the PZT. Number of samples was 38.

Information was also acquired from microphones at 0 cm (Figure 45), 1 cm (Figure 46) and 2 cm (Figure 47) from the bottom edge of ring PZT.

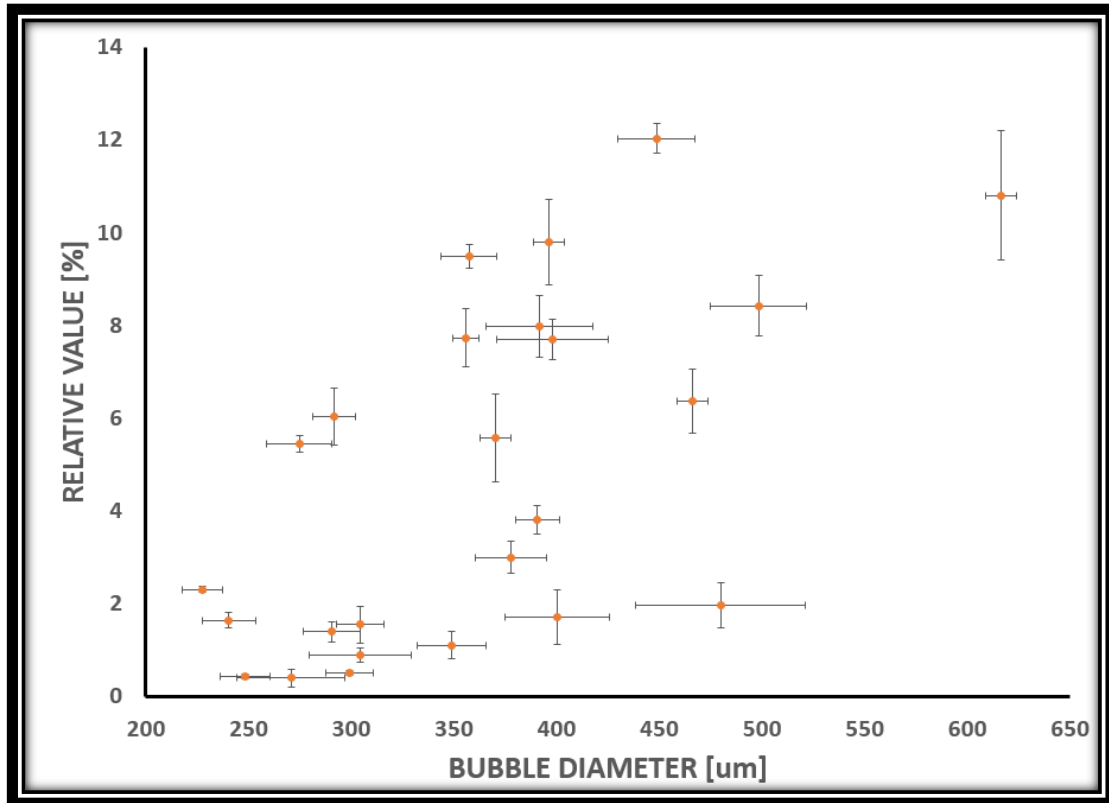


Figure 45: Data obtained from measuring the voltage in a pill microphone located at the bottom edge of the PZT when the PZT was actuated when the bubble was located at 1cm from the PZT. Number of samples =38.

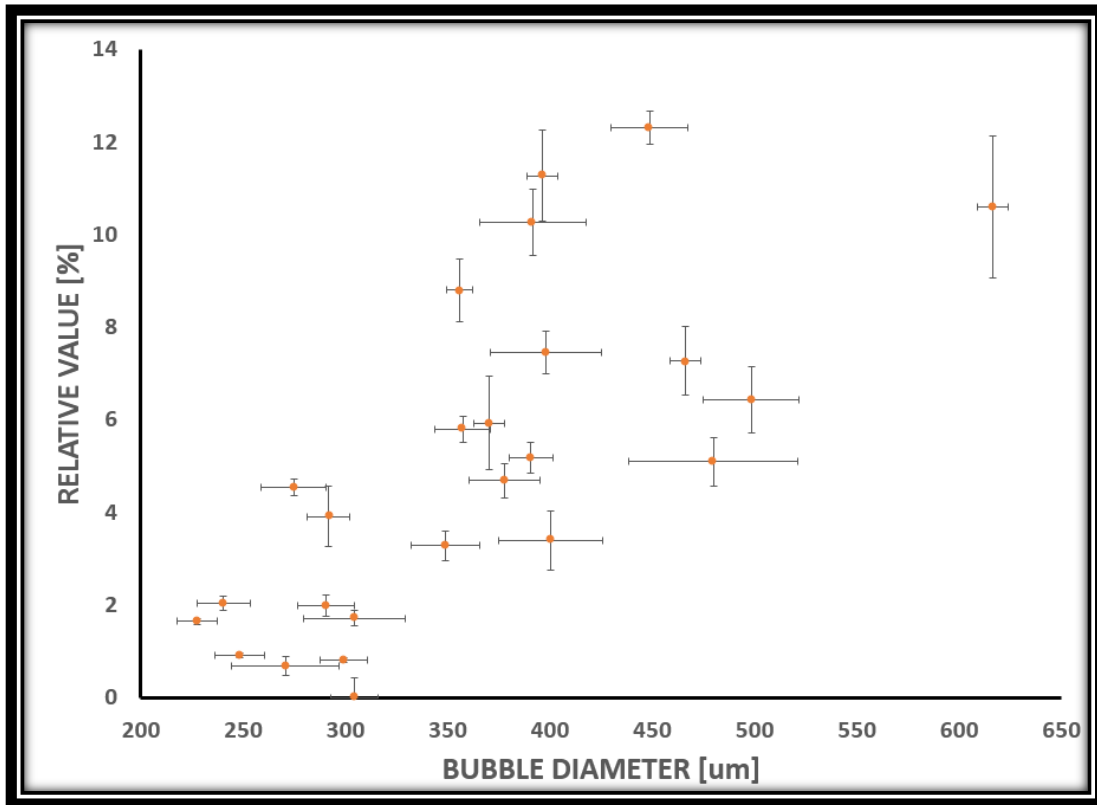


Figure 46: Data obtained from measuring the voltage in a pill microphone located at 1 cm from the bottom edge of the PZT when the PZT was actuated when the bubble was located at 1 cm from the PZT. Number of samples = 38.

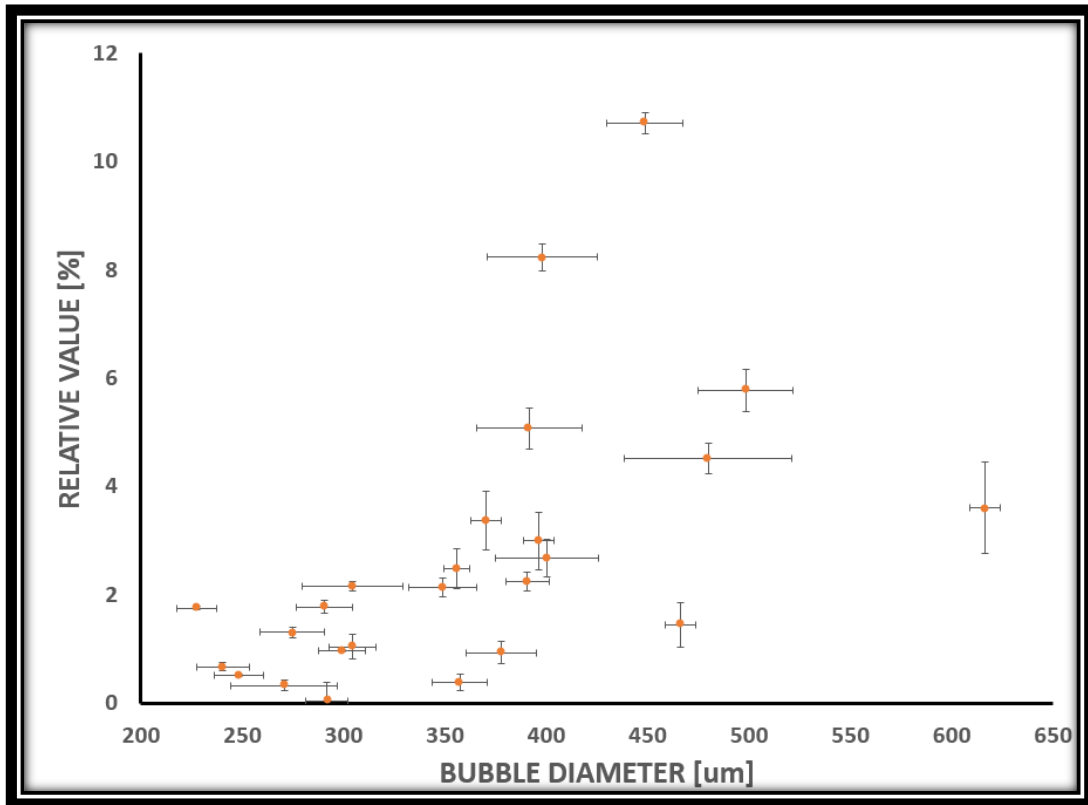


Figure 47: Data obtained from measuring the voltage in a pill microphone located 2cm from the bottom edge of the when the PZT was actuated when the bubble was located at 1cm from the PZT. Number of samples = 38.

4.1.3 Bubbles located 2 cm from the PZT ring

From the data in Figure 48 it can be concluded that if bubbles are further away than 2cm from the PZT, the system cannot detect them.

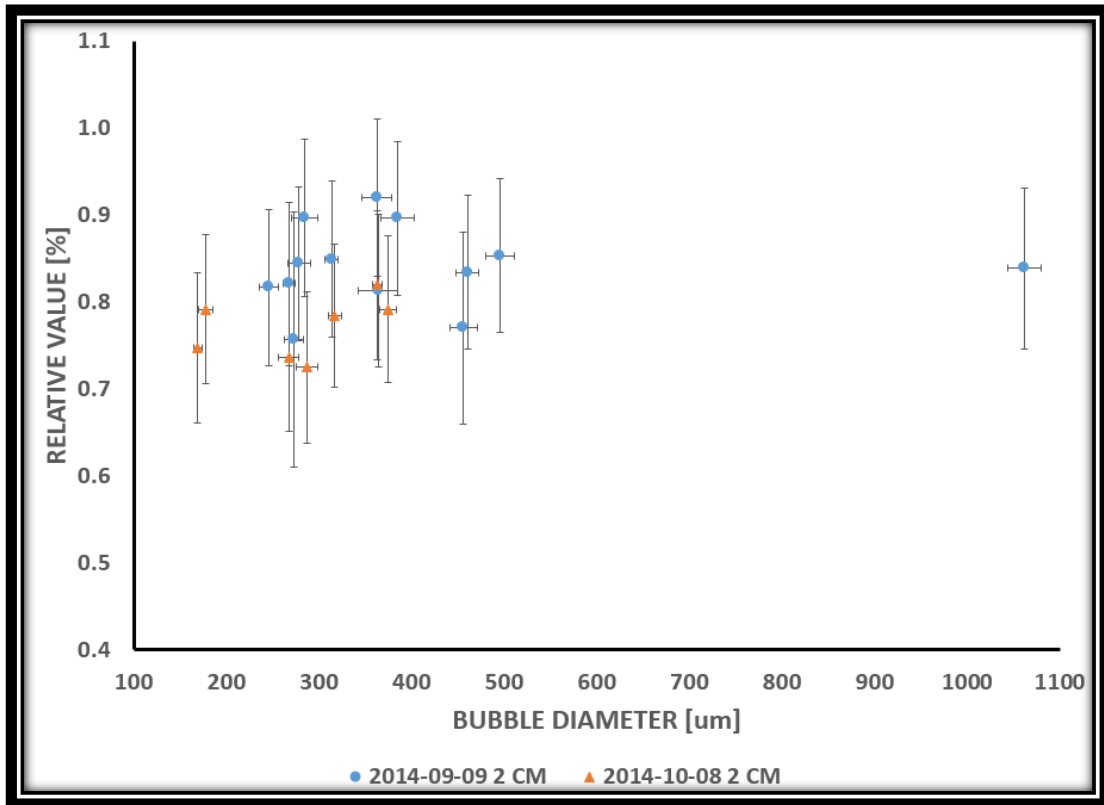


Figure 48: Data obtained when the PZT was actuated when the bubble was at 2cm below the PZT. Number of samples = 20.

4.2 Bubble detection with 1 feature for 2 Classes

Initially, the relationship between relative value vs bubble size diameter was classified into 2 types. The class “o” indicates the bubbles with a diameter less than 500 μm and the class “x” are bubbles larger than 500 μm . For the training data 3 different classifiers were used. The training step was developed for the three classifiers.

4.2.1 K-mean

Prediction of the K-mean algorithm (added STD predictor, see Appendix 7.7) was used when 100 data samples corresponding to the PZT were being actuated when the bubbles were at

its center. “0” represents bubbles predicted to have a size smaller than 500 μm and “1” represents bubbles bigger than 500 μm (Figure 49):

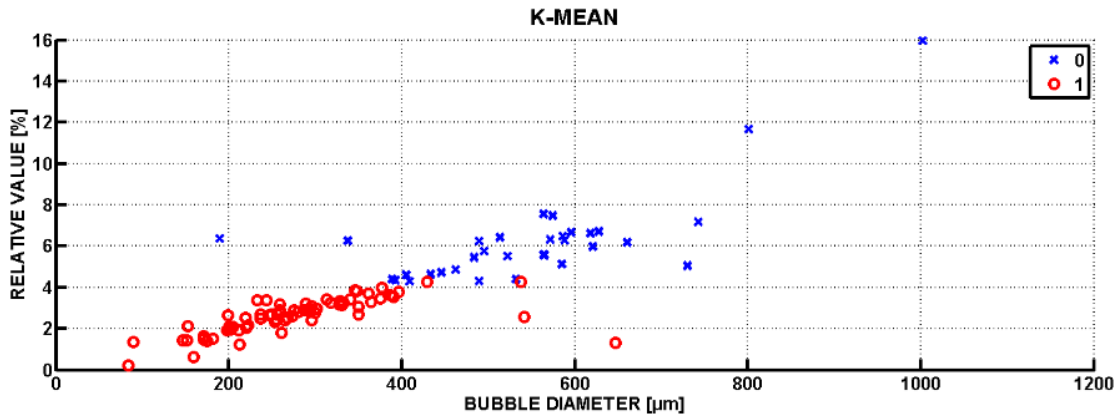


Figure 49: The prediction of the K-mean algorithm response with 100 data samples.

Table 3 indicates the real data (vertically), and the data detected by the K-mean algorithm (horizontally).

		Real		
		0	1	Total
K-mean	0	64	3	67
	1	13	20	33
	Total	77	23	100

Table 3: Results from the K-mean prediction to 1 feature and 2 classes.

The accuracy and error in bubble detection are:

$$Accuracy = \frac{84}{100} = 0.84$$

$$Error = \frac{16}{100} = 0.16$$

4.2.2 SVM

Predicted results of the SVM algorithm were used when 100 data samples corresponding to the PZT were being actuated when the bubbles were at its center (see Figure 50). “0” represents bubbles predicted to have a size smaller than 500 μm and “1” represents bubbles bigger than 500 μm.

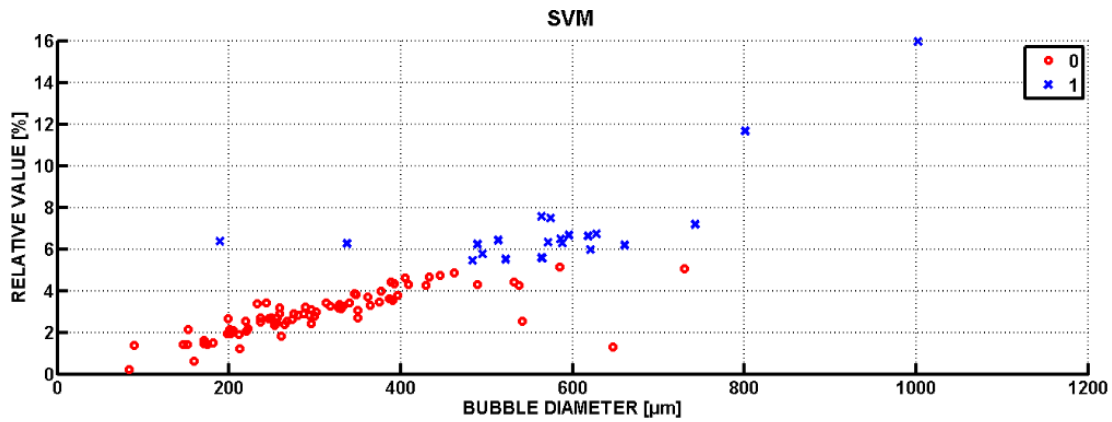


Figure 50: Results of the SVM algorithm with 100 data samples.

The following table shows the real data samples (vertically), with the data detected by the SVM algorithm (horizontally).

		Real		
		0	1	Total
SVM	0	72	6	78
	1	5	17	22

	Total	77	23	100
--	--------------	----	----	-----

Table 4: Results from the SVM prediction to 1 feature and 2 classes.

The accuracy and error in bubble detection are:

$$Accuracy = \frac{89}{100} = \mathbf{0.89}$$

$$Error = \frac{11}{100} = \mathbf{0.11}$$

4.2.3 NN

Figure 51 shows the predicted results of the NN algorithm when 100 data samples corresponding to the PZT being actuated when the bubbles were at its center was used. “0” represents bubbles predicted to have a size smaller than 500 μm and “1” represents bubbles bigger than 500 μm.

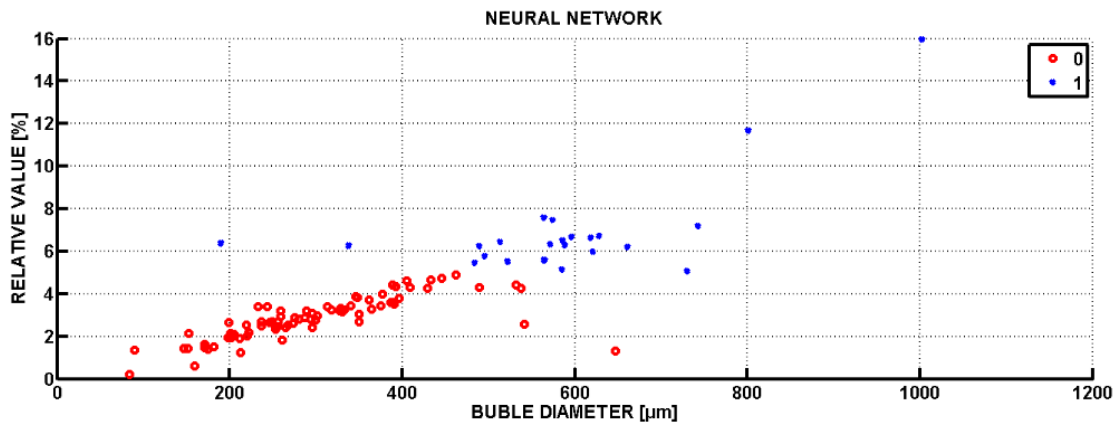


Figure 51: Results of the NN algorithm with 100 samples.

The following table shows the real data (vertically), with the data detected by the NN algorithm (horizontally).

		Real		
		0	1	Total
NN	0	72	4	76
	1	5	19	24
	Total	77	23	100

Table 5: Results from the NN prediction to 1 feature and 2 classes.

The accuracy and error in bubble detection are:

$$Accuracy = \frac{91}{100} = \mathbf{0.91}$$

$$Error = \frac{9}{100} = \mathbf{0.09}$$

4.3 Bubble detection with 1 feature for 5 Classes

The detection of the bubbles in this section has been performed using the current signal and bubble diameter information divided into 5 classes. The 5 classes have been determined using the K-mean as reference. The K-mean classification was:

Label	Interval
0	bubbles smaller than 220 μm

1	220 μm and 330 μm
2	330 μm and 480 μm
3	480 μm and 660 μm
4	bubbles bigger than 660 μm

Table 6: Intervals obtained from the K-mean classification to 1 feature and 5 classes.

4.3.1 K-mean

Figure 52 shows the prediction of the K-mean algorithm when 100 data samples were used.

The Table 6 indicated the intervals in which predictor K-mean algorithm detected bubbles.

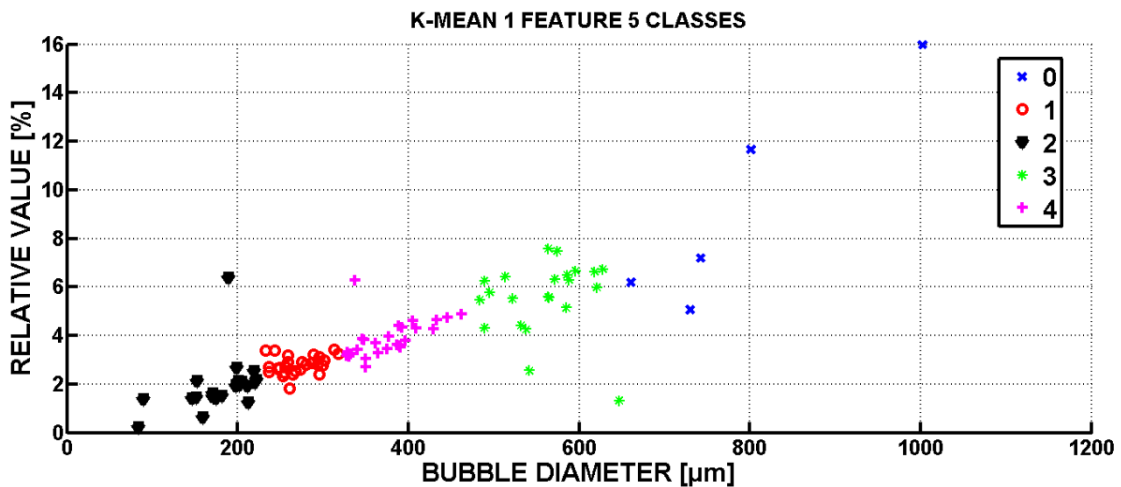


Figure 52: The prediction of the K-mean algorithm was used when 100 data samples corresponding to the PZT were being actuated when the bubbles were at its center.

		Real					Total
		0	1	2	3	4	
KMEAN	0	9	3	0	1	0	13
	1	2	25	4	0	0	31
	2	0	3	26	4	0	33

	3	1	1	2	15	0	19
	4	0	0	1	1	2	4
	Total	11	34	28	24	3	100

Table 7: Results from the K-mean prediction to 1 feature and 5 classes.

The accuracy and error in bubble detection are:

$$Accuracy = \frac{77}{100} = \mathbf{0.77}$$

$$Error = \frac{23}{100} = \mathbf{0.23}$$

The poor performance of this algorithm is due to which data on the edges of each cluster can affect the variance of several clusters similarly, and the algorithm associate the new data to the wrong cluster.

4.3.2 SVM

The SVM algorithm detected four classes of 5 (Figure 53). This algorithm depends on the stage of training and not detecting class 5 may be due to the lack of observations to find optimal separability between classes.

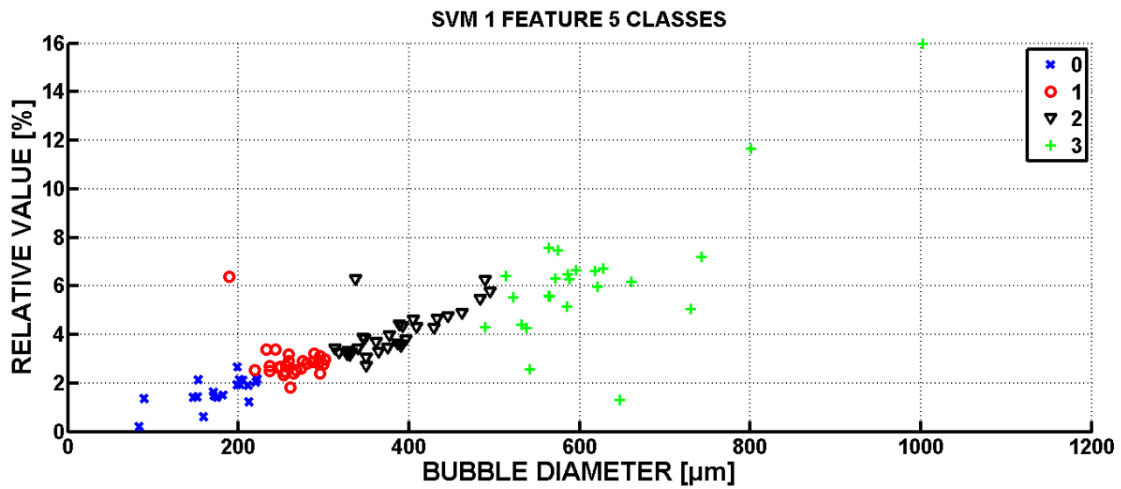


Figure 53: The prediction of the SVM algorithm was used when 100 data samples corresponding to the PZT were being actuated when the bubbles were at its center.

		Real					Total
		0	1	2	3	4	
SVM	0	12	7	0	0	0	19
	1	1	24	1	0	0	26
	2	0	0	31	0	0	31
	3	0	0	1	19	4	24
	4	0	0	0	0	0	0
	Total	13	31	33	19	4	100

Table 8: Results from the SVM prediction to 1 feature and 5 classes.

The accuracy and error in bubble detection are:

$$Accuracy = \frac{86}{100} = 0.86$$

$$Error = \frac{14}{100} = 0.14$$

The performance dropped by 3% in accuracy with respect to detection of two classes. It is good because it could further increase the number of intervals, and the accuracy lost is under 5%, considering that an accuracy lost larger than 5% is relevant.

4.3.3 NN

The procedure was similar to SVM training, i.e. training was used for the current signal only.

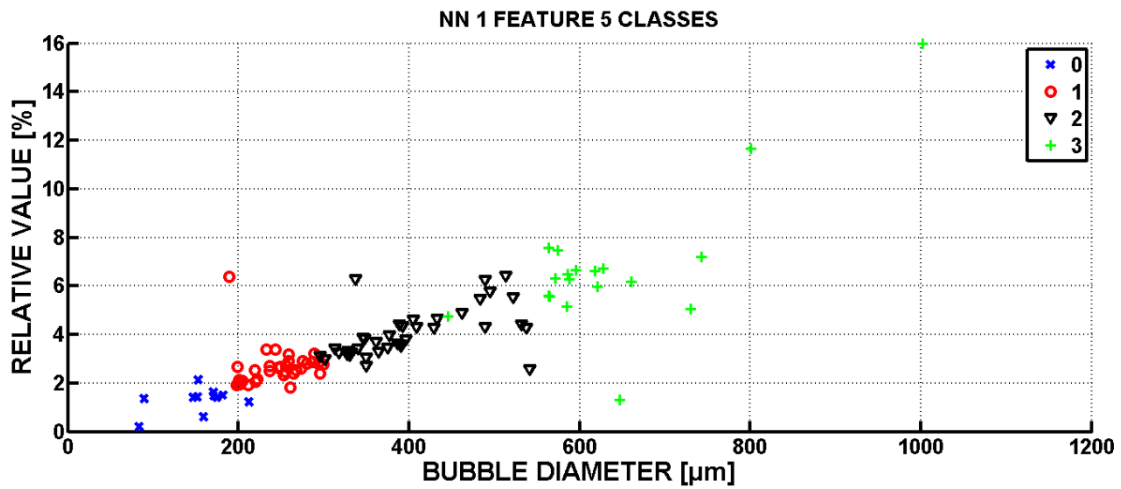


Figure 54: The prediction of the NN algorithm was used when 100 data samples corresponding to the PZT were being actuated when the bubbles were at its center.

		Real					Total
		0	1	2	3	4	
NN	0	10	1	0	0	0	11
	1	3	29	0	0	0	32
	2	0	1	33	5	0	39
	3	0	0	0	14	4	18

	4	0	0	0	0	0	0
	Total	13	31	33	19	4	100

Table 9: Results from the NN prediction to 1 feature and 5 classes.

The accuracy and error in bubble detection are:

$$Accuracy = \frac{86}{100} = \mathbf{0.86}$$

$$Error = \frac{14}{100} = \mathbf{0.14}$$

The NN algorithm accuracy lost 5% due to increase the number of classes.

4.4 Bubble detection with 3 features for 2 classes

The input data for detection algorithms were: current signal from the PZT ring signal, voltage signal from the MP1 (0 cm) and voltage signal from the MP2 (2 cm). This set of inputs was selected because, as mentioned in section 3.6.2, these three devices are common to 63 data samples. On the other hand, only half the data would have been used for testing.

4.4.1 K-mean

“0” represents bubbles predicted to have a size smaller than 400 μm and “1” represents bubbles bigger than 400 μm.

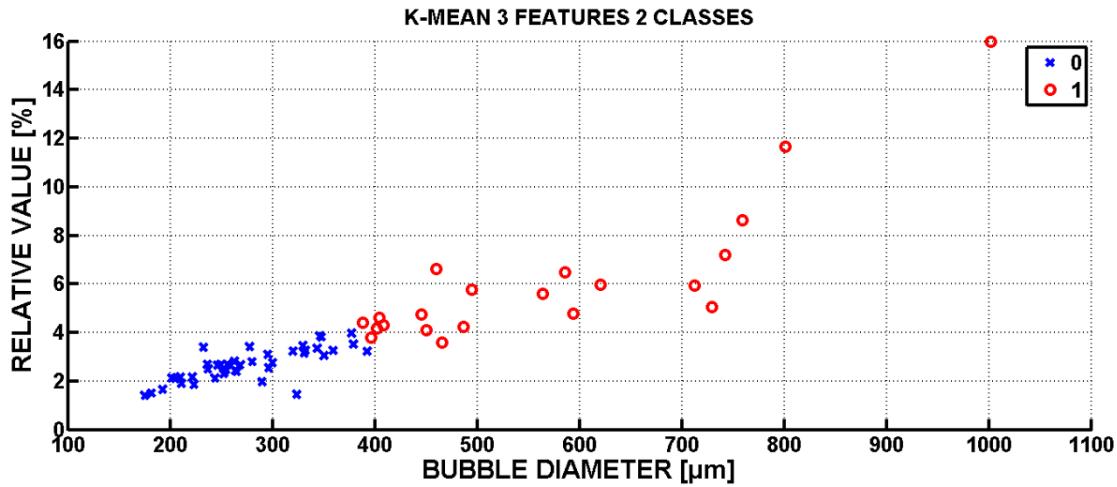


Figure 55: Prediction of the K-mean algorithm response with 63 data samples.

The first test is to detect bubbles again for 2 classes. Figure 55 shows the plot of relative value against bubble diameter. The response of the algorithm is summarized in the legend, that is, the grouping of the cluster "0" and the cluster "1".

		Real		Total
		0	1	
K-mean	0	39	3	42
	1	0	21	21
	Total	39	24	63

Table 10: Results from the K-mean prediction to 3 feature and 2 classes.

The accuracy and error in bubble detection are:

$$Accuracy = 0.95$$

$$Error = 0.05$$

It should be noted that the number of data decreased from 100 samples to 63 samples. Also, signals from the microphones were also implemented. Thus, prediction accuracy improved by 10%.

4.4.2 SVM

This algorithm training was conducted as: “0” represents bubbles predicted to have a size smaller than 400 μm and “1” represents bubbles bigger than 400 μm (Figure 56).

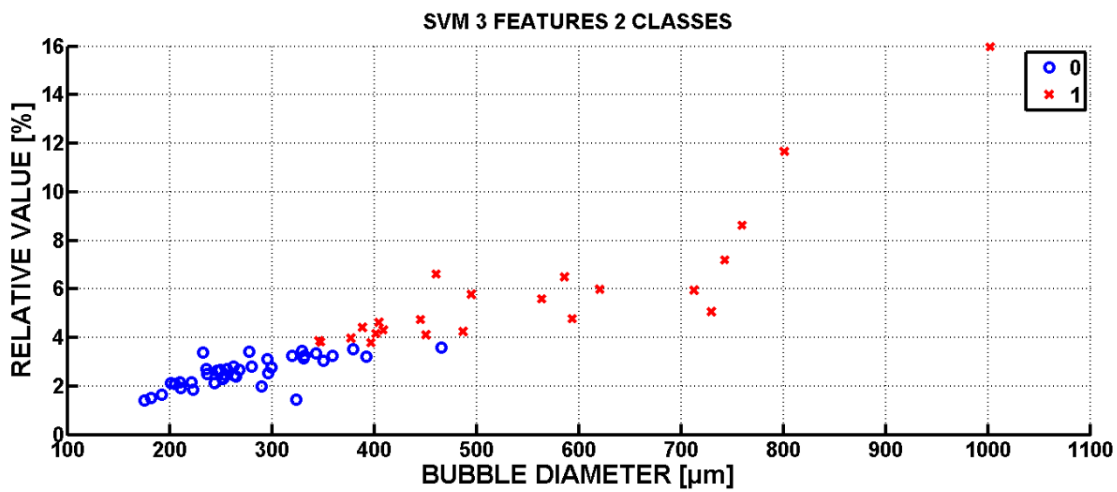


Figure 56: Results of the SVM algorithm with 63 data samples.

		Real		Total
		0	1	
SVM	0	37	3	40
	1	2	21	23
	Total	39	24	63

Table 11: Results from the SVM prediction to 3 feature and 2 classes.

The accuracy and error in bubble detection are:

Accuracy = 0.92

Error = 0.08

The SVM algorithm as K-mean algorithm, also improved with respect to the detection of two classes only using the current signal. For this SVM algorithm, the accuracy improved over the previous result by 3%.

4.4.3 NN

The NN algorithm as SVM algorithm was trained with: “0” represents bubbles predicted to have a size smaller than 400 μm and “1” represents bubbles bigger than 400 μm (Figure 57).

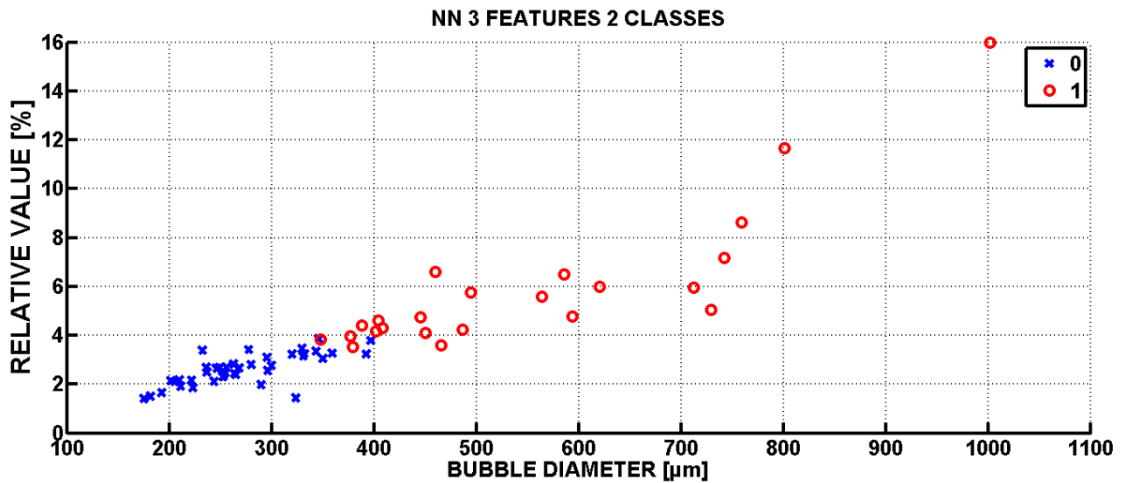


Figure 57: Response of the NN algorithm with 63 data samples.

		Real		Total
		0	1	
NN	0	38	1	39
	1	2	22	24

	Total	40	23	63
--	--------------	----	----	----

Table 12: Results from the NN prediction to 3 feature and 2 classes.

The accuracy and error in bubble detection are:

$$Accuracy = 0.95$$

$$Error = 0.05$$

The NN algorithm improved its accuracy by 4% using microphones information with respect to the detection of bubbles using only current information from the PZT ring.

4.5 Bubble detection with 3 features for 5 classes

For this step the curve for relative value against bubble diameter was divided into 5 classes in the same manner as in section 4.2. The labels are:

Label	Interval
0	bubbles smaller than 290 μm
1	290 μm and 360 μm
2	360 μm and 490 μm
3	490 μm and 620 μm
4	bubbles bigger than 620 μm

Table 13: Intervals obtained from the K-mean classification to 3 features and 5 classes.

4.5.1 K-mean

The prediction of the K-mean algorithm was used when 63 data samples corresponding to the PZT being actuated when the bubbles were at its center was used. Table 13 shows the intervals for the detection of the bubbles.

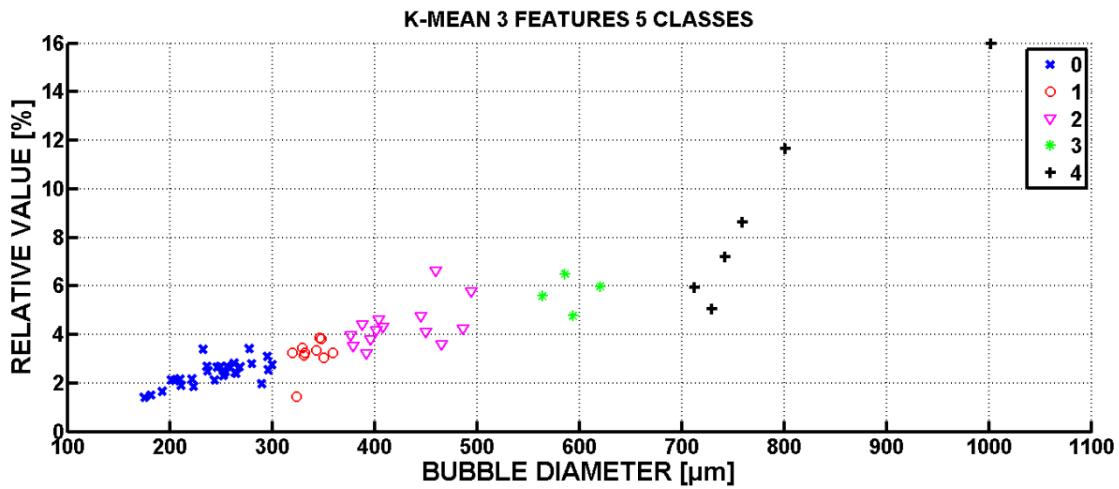


Figure 58: Prediction of the K-mean algorithm response with 63 data samples to 3 features and 5 classes.

		Real					TOTAL
		0	1	2	3	4	
KMEAN	0	13	0	0	0	1	14
	1	0	6	0	0	0	6
	2	0	0	10	0	0	10
	3	0	0	3	26	0	29
	4	0	0	0	0	4	4
	Total	13	6	13	26	5	63

Table 14: Results from the K-mean prediction to 3 feature and 5 classes.

The accuracy and error in bubble detection are:

$$Accuracy = 0.94$$

$$Error = 0.06$$

The loss of precision was 1% compared to the detection of bubbles for 2 classes shown in section 4.3.1. It is due to the problem of edges in the detection mentioned above.

4.5.2 SVM

The detection of the SVM algorithm when 63 data samples corresponding to the PZT being actuated when the bubbles were at its center was used. The Table 13 indicated the intervals in which predictor SVM algorithm detects bubbles.

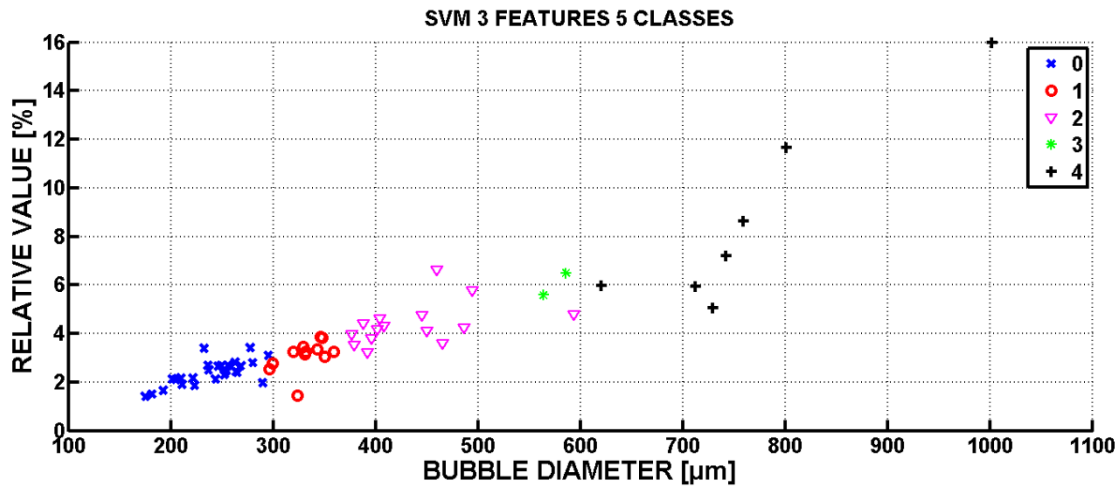


Figure 59: The prediction of the SVM algorithm response with 63 data samples to 3 features and 5 classes.

		Real					Total
		0	1	2	3	4	
SVM	0	13	0	0	0	0	13
	1	0	6	0	0	0	6
	2	0	0	12	1	0	13

	3	0	0	0	26	0	26
	4	2	1	0	0	2	5
	Total	15	7	12	27	2	63

Table 15: Results from the SVM prediction to 3 feature and 5 classes.

The accuracy and error in bubble detection are:

$$Accuracy = 0.94$$

$$Error = 0.06$$

The accuracy of the SVM algorithm improved by 2% with respect to the detection of two classes using 3 features. This means that observations from the microphones are a significant contribution to this detection algorithm.

4.5.3 NN

The NN algorithm as SVM algorithm was trained with data from the Table 13.

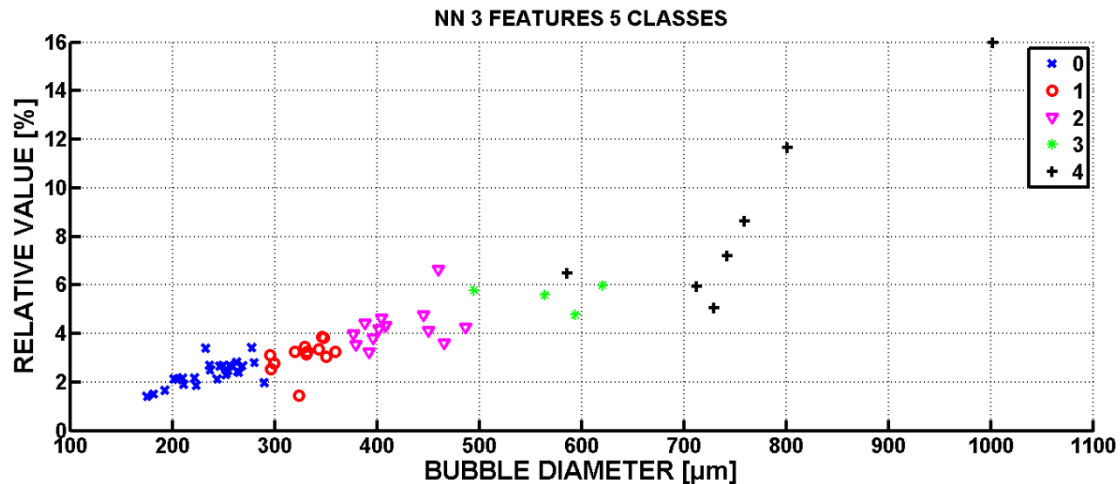


Figure 60: Prediction of the NN algorithm response with 63 data samples to 3 features and 5 classes.

		Real					Total
		0	1	2	3	4	
NN	0	13	0	0	0	0	13
	1	0	6	0	0	0	6
	2	0	0	13	0	0	13
	3	0	0	0	26	0	26
	4	0	1	0	0	4	5
	Total	13	7	13	26	4	63

Table 16: Results from the NN prediction to 3 feature and 5 classes.

The accuracy and error in bubble detection are:

$$Accuracy = 0.98$$

$$Error = 0.02$$

The NN algorithm improved the accuracy by 3% compared to the detection of two classes using 3 features. The NN algorithm is more accurate in comparison to SVM and K-mean.

4.6 Overview and rate of convergence

The algorithm analysis in the previous sections, were performed based on the accuracy and error in the bubbles detection. In this section, the iterations and rate of convergence are detected.

For the comparison, a laptop with a processor “Intel(R) Core(TM) i7-2670QM CPU @ 2.20GHz” was used. The priority configuration for MATLAB software was changed to real time in the computer. The “TALKLIST” command was called to determine the processes of the computer (see Appendix 7.8). The total CPU process is **368192**. The specification for the computer to millions instructions per seconds (MIPS) is **128300**. This establishes that the time count for each

generating MATLAB algorithm presents additional time of about **3 μ sec**. If the algorithms are being used by the computer, it would be negligible. However, there is no guarantee that the processing time of the algorithm is exactly from it. From the above, convergence time for each algorithm was defined in the following table:

Algorithm	Features	Classes	Iterations	Time of convergence
K-mean	1	2	4	0.14
SVM	1	2	14	1.20
NN	1	2	22	1.76
K-mean	1	5	5	0.16
SVM	1	5	29	1.84
NN	1	5	19	1.78
K-mean	3	2	8	0.15
SVM	3	2	21	1.34
NN	3	2	34	1.83
K-mean	3	5	7	0.16
SVM	3	5	27	1.84
NN	3	5	133	2.03

Table 17: Rate of convergence comparison for each algorithm

From the above table, the K-mean algorithm with STD predictor is the faster in convergence because their operations are simple, i.e. getting Euclidean distances and standard deviations. SVM and NN algorithms are methods which use decomposed matrices to solve optimization problems; this generates more computational resources, and causes a delay.

4.7 Summary of the results and analysis

The following table associates previous results in accuracy, iterations and convergence time for each algorithm in the respective condition as: characteristics and classes.

Algorithm	Samples	Features	Classes	Iterations	Time of convergence [seconds]	Accuracy
K-mean	100	1	2	4	0.14	84
SVM	100	1	2	14	1.20	89
NN	100	1	2	22	1.76	91
K-mean	100	1	5	5	0.16	77
SVM	100	1	5	29	1.84	86
NN	100	1	5	19	1.78	86
K-mean	63	3	2	8	0.15	95
SVM	63	3	2	21	1.34	92
NN	63	3	2	34	1.83	95
K-mean	63	3	5	7	0.16	94
SVM	63	3	5	27	1.84	94
NN	63	3	5	133	2.03	98

Table 18: Summary of the results.

Note that the addition of new features to all predictor's algorithms improves accuracy. The next image can better show this statement:

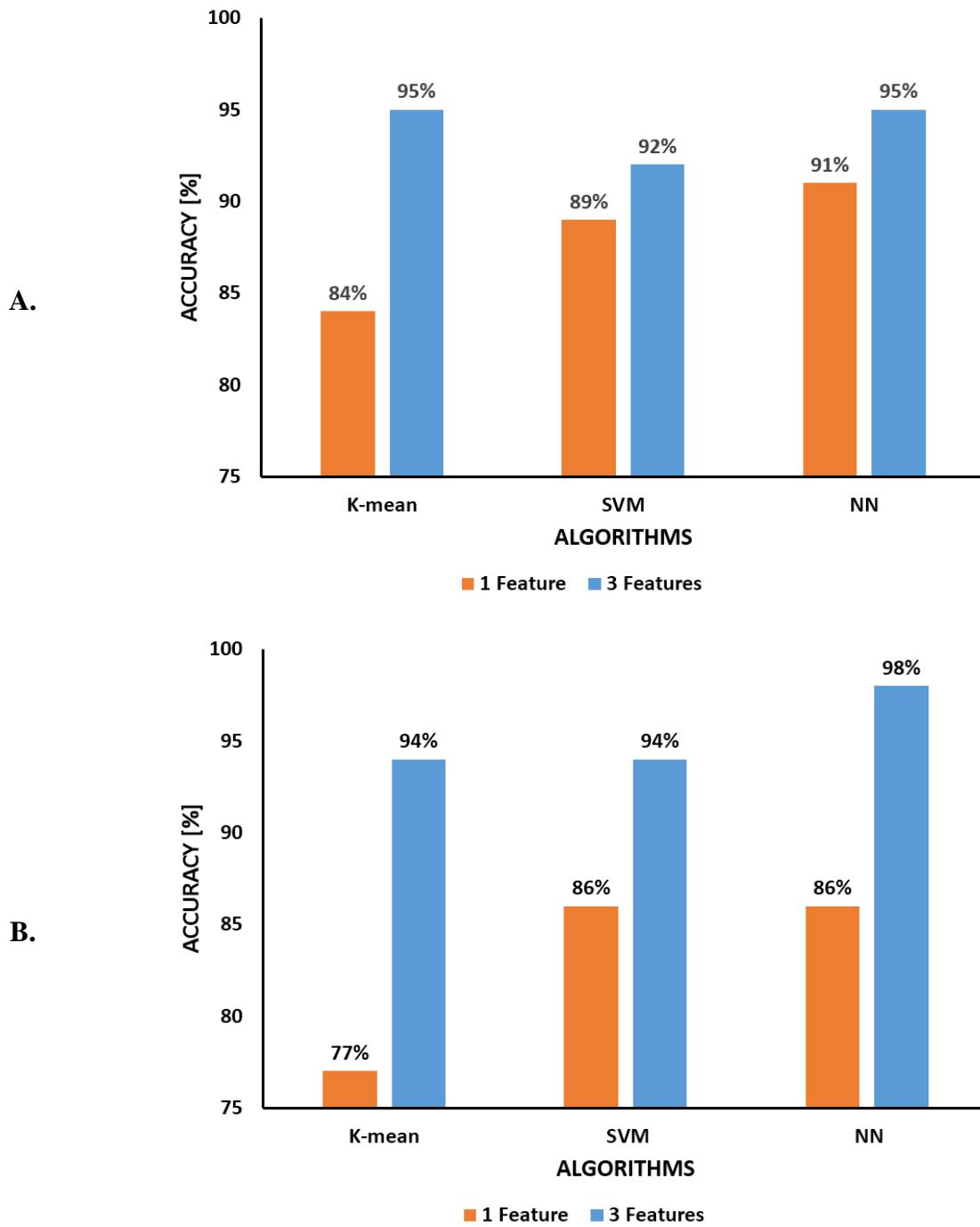
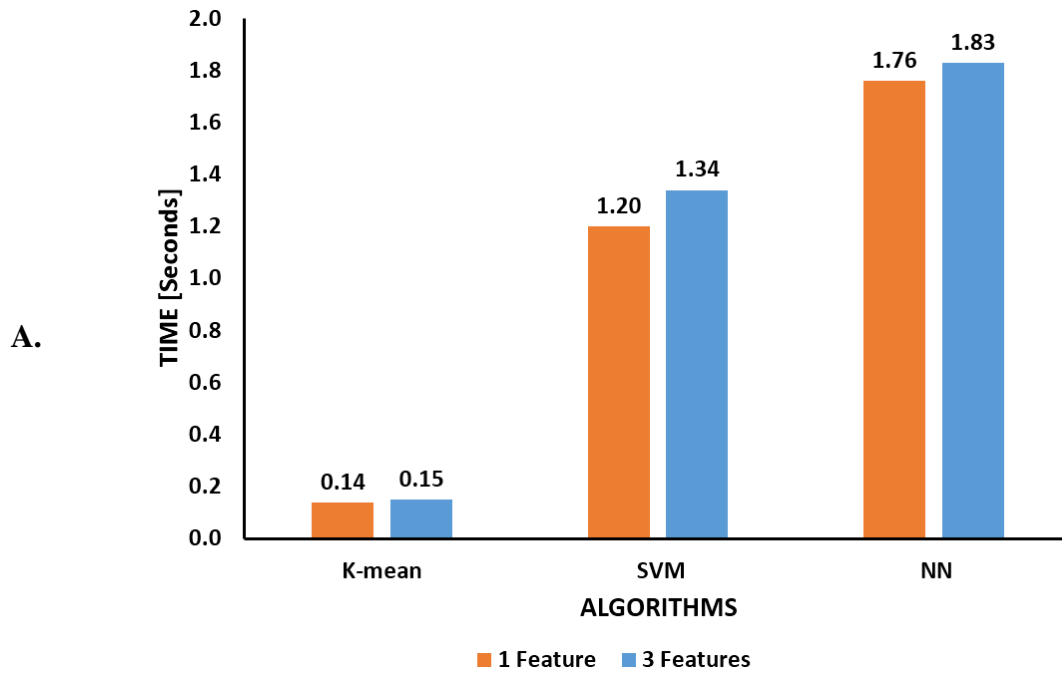


Figure 61: Predictor accuracy: A - is to 2 classes, the 3 first bins are the predictor results from 1 feature and the last 3 bins are the predictor results from 3 features. B is to 5 classes, the 3 first bins are the predictor results from 1 feature and the last 3 bins are the predictor results from 3 features.

Figure 61 demonstrates that increasing the amount of characteristics, leads to an increase in the accuracy.



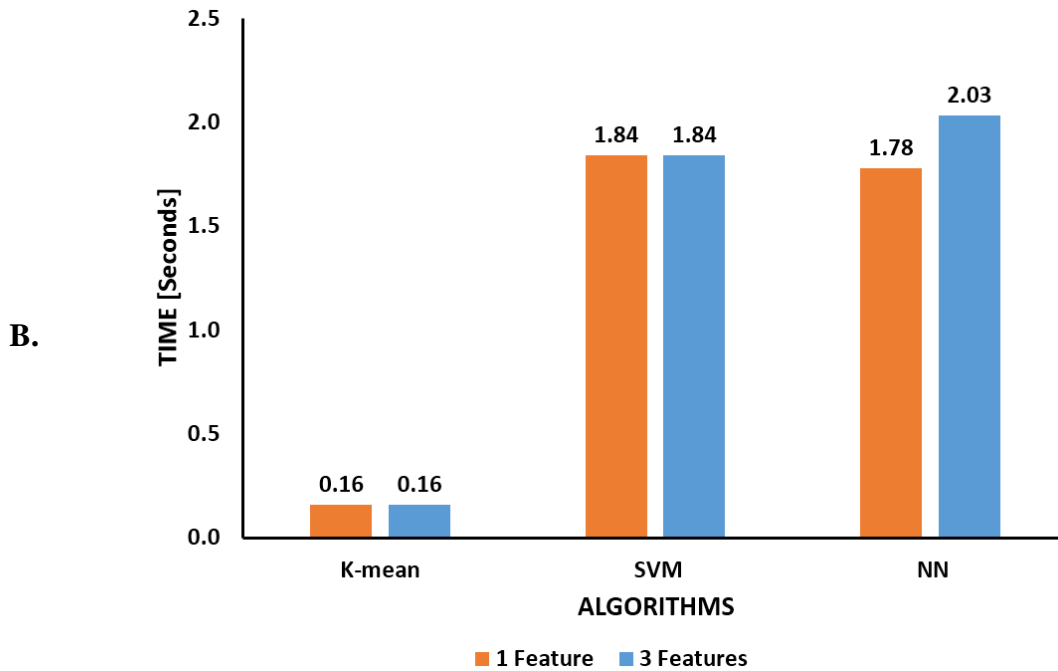


Figure 62: A - indicates the time of convergence to predictors for 2 classes. B - indicates the time of convergence to predictors for 5 classes.

Convergence times of the algorithms show which supervised algorithm takes more time to converge due to the simplicity in calculating geometric distances, compared to solving optimization problems as noted in section 4.5.

Among choices for most accurate algorithm for bubbles detection, the neural network would be appropriate choice of considering the accuracy from the Table 18. On the other hand, based on the choice of the faster algorithm for bubbles detection, the answer is K-mean with STD predictor.

Analyzing the disadvantages, it is important to remember that the election of targets for the training stage was made by the K-mean. This favors the high precision of K-mean and STD predictor.

Another important point is the number of iterations when the features and classes are increased in neural networks. On a computer with the technical features that were used, it is not relevant; but when the implementation is in a microcontroller, FPGA or DSP hardware device the convergence time would increase considerably.

4.8 Further testing

Section 3.6.2 showed results for bubbles detection at 1 cm from the edge bottom of the PZT ring.

Assuming the sensor works in a pulsated manner, and bubbles are present in the blood stream, then if the bubbles moving along the artery are further away than 2cm from the PZT the system will not detect them. If the bubble are between 0-1cm from the PZT the system will detect them.

The question is: will our sensor be able to distinguish a small bubble that might be at the center of the PZT when the PZT is actuated, from a big bubble that is at 1cm from the PZT when the PZT is actuated? Based on the obtained results, the answer to that question, is that it will. The results are shown in Table 19, Table 20 and Table 21.

		Real		
		0	1	Total
K-mean	0	33	3	36
	1	2	25	27
	Total	35	28	63

Table 19: Confusion matrix for the K-mean algorithm with 4 features for the data points corresponding to the actuated PZT when the bubbles were at the center of the PZT and for bubbles that were located at 1cm away from the PZT when it was actuated.

The accuracy and error of the K-mean and STD predictor algorithm are:

$$Accuracy = \frac{58}{63} = \mathbf{0.92}$$

$$Error = \frac{5}{63} = \mathbf{0.08}$$

		Real		
		0	1	Total
SVM	0	31	10	41
	1	4	18	22
	Total	35	28	63

Table 20: Confusion matrix for the SVM algorithm with 4 features for the data points corresponding to the actuated PZT when the bubbles were at the center of the PZT and for bubbles that were located at 1cm away from the PZT when it was actuated.

The accuracy and error of the SVM predictor algorithm are:

$$Accuracy = \frac{49}{63} = \mathbf{0.78}$$

$$Error = \frac{14}{63} = \mathbf{0.22}$$

		Real		
		0	1	Total
NN	0	33	1	34
	1	2	27	29

	Total	35	28	63
--	--------------	----	----	----

Table 21: Confusion matrix for the neural network algorithm with 4 features for the data points corresponding to the actuated PZT when the bubbles were at the center of the PZT and for bubbles that were located at 1cm away from the PZT when it was actuated.

The accuracy and error of the NN predictor algorithm are:

$$Accuracy = \frac{60}{63} = \mathbf{0.95}$$

$$Error = \frac{3}{63} = \mathbf{0.05}$$

CHAPTER V

CONCLUSION AND FUTURE WORK

5.1 CONCLUSION

The present study using an artificial thigh prototype with a piezoelectric ring, has shown feasibility in the bubble detection. For the purpose of this study, the addition of the individual components as pill microphones to improve the accuracy of the algorithms have been experimentally studied.

In section 3.3.3 of this work, the different features extractions methods to determine the relationship between relative value (from the current signals) and the bubbles diameter were discussed. Method 2 was effective because it allows for control between the induction of the bubble in the prototype, and also in the measurement of the bubble across the PZT.

In section 4.1.3 of the thesis, the maximum distance for the detection of the bubbles; in our case at 2 cm, was determined. Thus, the focus of the experiments was with the PZT actuated when the bubble at a distance less than 2 cm from the bottom edge of the PZT.

In section 4.7, the information obtained from the features extraction stage as inputs. Initially, the setup was 1 feature with 2 classes (detecting 2 bubbles sizes), were applied. Eventually, the amount of classes implemented in the algorithm increased to 5, in which the accuracy decreased up to a maximum of 5%. Thus, the next step was to increase the amount of features to 3 (PZT, MP1 and MP2) with 2 classes. In comparison with the previous result of using 1 feature and 2 classes, the accuracy of the algorithm increased by 11%, 3% and 4% to K-mean, SVM and NN,

respectively. Given this improvement in accuracy which was achieved by implementing more features, the next step consisted of incrementing the amount of classes up to 5. The results showed high performance in accuracy (over 90%) for all algorithms when the amount of the features and classes were increased.

In chapter four of the thesis, the pattern recognition methods with classifiers (K-mean, SVM and NN) having an accuracy of 94%, 94%, and 98%, respectively for bubble detection, were presented. The results showed that the best algorithm for the detection of bubbles for the combinations of classes and features being tested was the NN (98%). However, the computational cost of using this method (133 iterations) is a problem when compared to the efficiency of the K-mean with STD predictor (94% in accuracy and 7 iterations) which is a good choice for randomized clustering.

5.2 FUTURE WORK

In this thesis, the main objective was to implement a pattern recognition scheme to indicate the presence of micro-bubbles in a diver. Prior to implementing the developed algorithm, a more complicated prototype that simulates the human thigh was implemented in order to obtain results as close as possible to the real conditions. To continue the work presented here the following suggestions are presented:

- Considering the “features” obtained from the microphones, the accuracy of the bubble detection can be improved by increasing the number of microphones around the acoustic chamber.

- The classifiers can be tested by adding more classes in order to answer to the question: What is the maximum number of classes that the algorithms can identify while maintaining an accuracy over 90%?

- Establish a relationship between the void fraction and bubble population. This relationship would contribute to the design of an estimator for determining the possible number of bubbles in the bubble population.

REFERENCES

Acott Chris JS Haldane, JBS Haldane, L Hill and a Siebe: A brief resume of their lives [Journal] // SPUMS Journal. - 1999. - pp. 163-164.

Altera Corporation FPGA Stratix 10 Datasheet. - 2015.

Bookspan Jolie Diving Physiology in Plain English [Book]. - San Francisco : Undersea & Hyperbaric Medical Society, 1997.

Borrion Hervé Study of processing techniques for radar non-cooperative target recognition. - London : [s.n.], September 2006.

Brandon Rhudy Matthew Real Time Implementation of a Military Impulse Noise Classifier. - Pennsylvania : [s.n.], 2008.

Brock-Fisher George A. Ultrasound device to detect Caisson's disease [Patent]. - USA, 23 2, 2004.

Buckey J. C. [et al.] Dual-frequency ultrasound detection of stationary microbubbles in tissue [Journal] // Undersea & Hyperbaric Medicine. - 2009. - 2 : Vol. 36. - pp. 1041-1047.

Cancelos S. [et al.] The effect of acoustically induced cavitation on the permeance of a bullfrog urinary bladder. [Journal] // J Acoust Soc Am. - 2010. - pp. 2726-38.

Cancelos Silvina [et al.] The Design of acoustic chamber for bubble dynamics research [Journal] // Multiphase Science and Technology. - 2005. - 3 : Vol. 17. - pp. 257-291.

Corporation Altera FPGA Stratix 10 Datasheet. - 2015.

Daniels Stephen. Decompression Bubble Detectors [Patent] : 4290432. - United States, 1981.

Dee Ryan Looking for bubbles: Bubble detection methods for predicting decompression illness in divers. // Looking for bubbles: Bubble detection methods for predicting decompression illness in divers.. - February 2, 2011.

Diniz Paulo S, Da Silva Eduardo A. B and Netto Sergio L. Digital Signal Processing: System analysis and design [Book]. - New York : Published in the United States of America by Cambridge University Press, 2010.

Duda Richard O, Hart Peter E and Stork David G. Pattern Classification [Book]. - New York : Wiley-interscience, 2000. - 10158-0012.

Franchetti Franz and Púsehel Markus. Fast Fourier Transform to Discrete Fourier Transform. - Pittsburgh : Department of Electrical and Computer Engineering Carnegie Mellon University Pittsburgh, 2011.

Gilliam Bret. Decompression Sickness: theory and treatment [Journal]. - 2012. - 8. - pp. 3-20.

Guo Shuxiang [et al.] Comparison of sEMG-Based Feature Extraction and Motion Classification Methods for Upper-Limb Movement [Journal] // Sensors. - 2015. - 15. - pp. 9022-9038.

Hajek Milan Neural Networks [Book]. - KwaZulu-Natal : University of KwaZulu-Natal, 2005.

Ingale Rajesh and Tawade Laxman. Detection and Comparison of Power Quality Disturbances using Different Techniques [Journal] // International Journal of Computer Applications. - Latur : International Journal of Computer Applications, 2013. - 18 : Vol. 75. - pp. 0975–8887.

Jain Anil K, W Duin Robert P. and and Mao Jianchang. Statistical Pattern Recognition: A Review [Conference]. - Michigan : [s.n.], 1999.

Jordan R and Ounaies Z. Piezoelectric Ceramics Characterization [Conference]. - Hampton : NASA Langley Research Center, 2001.

Karatzoglou Alexandros, Meyer David and Hornik Kurt Support Vector Machines in R [Journal] // Journal of Statistical Software. - 2006. - 9 : Vol. 15.

Kim Jina [et al.] Electrical Modeling of Piezoelectric Ceramics [Journal]. - Atlanta : IEEE Sensors Applications Symposium, 2008.

Ledoux Antoine Theory of Piezoelectric Materials and their applications in Civil engineering. - Paris : Ecole Centrale Paris, 2011.

Leighton T.G. The Acoustic Bubble [Book]. - San Diego : Academic Press, 1994.

Lutz Harald and Buscarini Elisabetta Manual of The Diagnostic Ultrasound [Journal] // World Health Organization. - 2011. - 208 : Vol. 1. - pp. 3-5.

Microchip Microchip Technology Inc. PIC 18F452 Datasheet.. - 2002.

Münz Gerhard, Li Sa and Carle Georg. Traffic anomaly detection using k-means clustering [Conference]. - Hamburg, Germany. : University of Tuebingen, Germany, 2007.

National Instruments Corporation NI 6356/6358 Specifications [Report]. - Austin, TX : National Instruments Corporation, 2009-2010.

Nishi R. Y and Eatock B. C. PROCEDURES FOR DOPPLER ULTRASONIC MONITORING OF DIVERS FOR INTRAVASCULAR BUBBLES [Conference] // Defence and Civil Institute of Environmental Medicine. - Ontario, Canada : Rubicon Research Repository , 1986.

Panagiotakis C and Tziritas G. A speech/music discriminator based on rms and zero-crossings [Journal] // IEEE Transactions on Multimedia. - 2005. - 1 : Vol. 7. - pp. 155-156.

Pérez Enrique and Barros Julio. Voltage Event Detection and Characterization Methods: A Comparative Study [Conference]. - Venezuela : IEEE, 2006.

Research Vision Speed Sense 9040-9090 specification.. - 2010.

Rojas Raúl Neural Networks A Systematic Introduction [Book]. - Berlin : Springer-Verlag, 1996.

Sande Eftedal Olav. Ultrasonic detection of decompression induced vascular microbubbles. - Trondheim : Norwegian University of Science and Technology, 2007.

Stein Jonathan Y. Digital Signal Processing: A Computer Science Perspective [Book]. - [s.l.] : John Wiley & Sons, Inc., 2000.

Teknomo Kardi K-Means Clustering Tutorial [Online]. - 07 2007. - 02 14, 2013. - <http://people.revoledu.com/kardi/tutorial/kMean/>.

TI DSP TMS320DM647 Datasheet. - Texas : Texas instruments , 2012.

Valentin Francisco An acoustic method for real time air bubble detection in simulated blood vessels [Report]. - Mayagues : [s.n.], 2012.

Webb Andrew R. Statistical Pattern Recognition [Book]. - Malvern, UK : John Wiley & Sons Ltd,, 2002. - Second.

APPENDIX

7.1 Algorithm setup bubble generating system

The program is as follows:

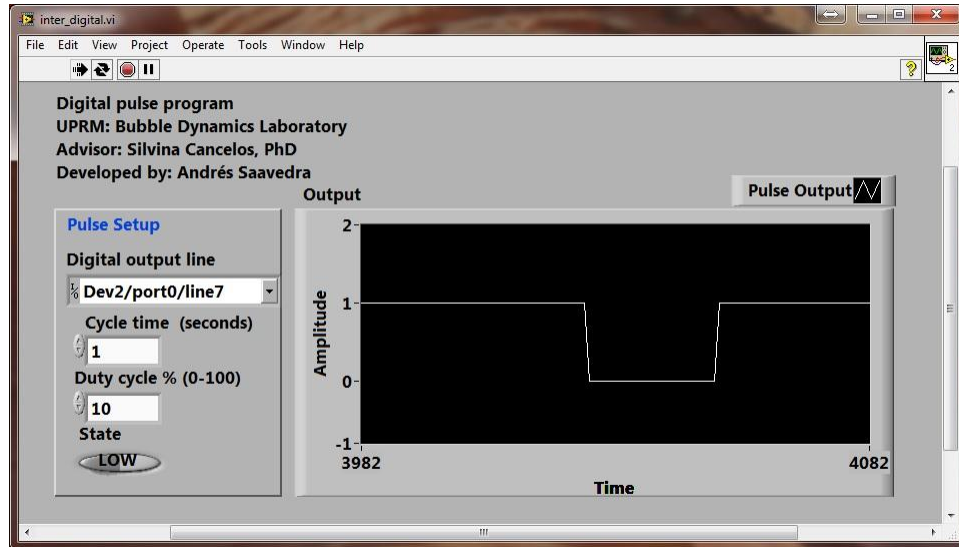


Figure 63: Pulse with modulator program in Labview.

This program determines the pulse time, the duty cycle and the state. The *duty cycle* is given by the relationship:

$$Duty\ cycle = \frac{\tau}{T} \quad (3.8)$$

where “ τ ” is the time, and the period of the signal is “ T ” (pulse time in our case). The *state* indicated when working with “ τ ” in low or high. Because the NI6356 card always broadcasts a high pulse on digital port, this condition maintains activation of the electro valve at all times, so

the state will work on low pulse (actuates the solenoid when the pulse goes down to a 10% duty cycle as shown in Figure 63).

7.2 Algorithm setup frequency response

The algorithm to detect the frequency response is shown in Figure 64.

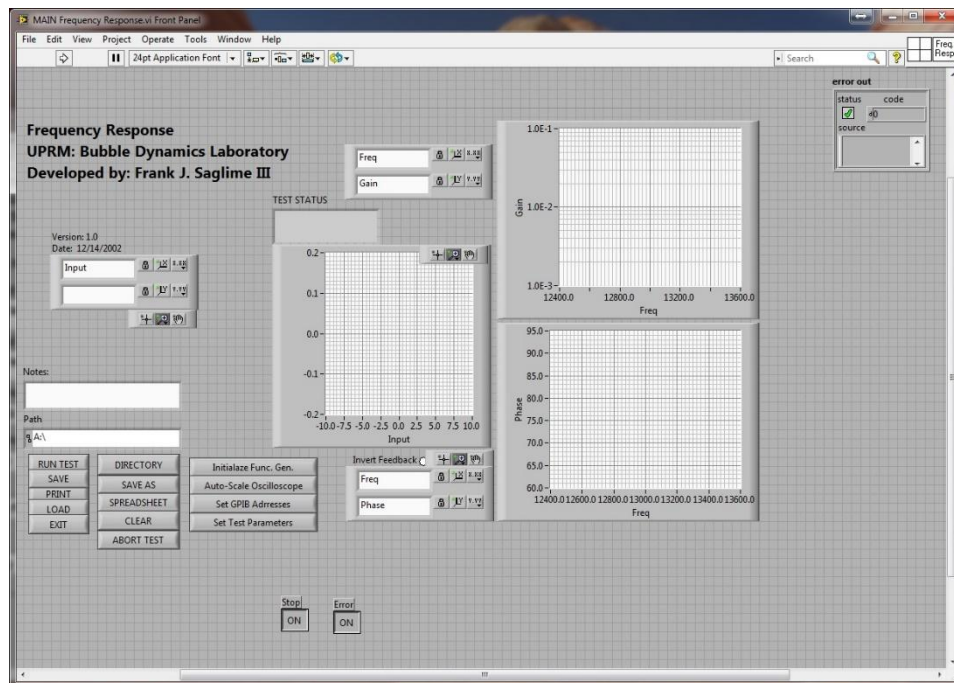


Figure 64: Frequency response algorithm

For the first step is necessary select the GPIB address. Each device, like the waveform generator and the oscilloscope, have addresses, therefore must be selected indicating the device. In our case, the oscilloscope address is 7 and the waveform generator is 11. The next step is to

select “set test parameters”, here the number of points, the range and breadth of the sweep frequency are chosen.

7.3 Algorithm setup acquisition signals

The front panel of the Labview program used with the data acquisition card is shown in Figure 65.



Figure 65: Data acquisition program (Front Panel)

Details of the configuration of the program are shown in Table 22:

Regions	Specifications
CHANNEL PARAMETERS	Establishes the channel parameters such as the amplitude level to be received in each channel.

TIMING PARAMETERS	Specifies the value for the sample rate, for example 1.0 MHz
SAVE OPTIONS	Select options for saving data, such as location and size of each file. The bottom "Split data file", when clicked, generates the partition size that was set.

Table 22: Data acquisition program settings.

7.4 Algorithms current drop detecting

7.4.1 Method 1

The following algorithm can detect the maximum amplitude of each semi cycle:

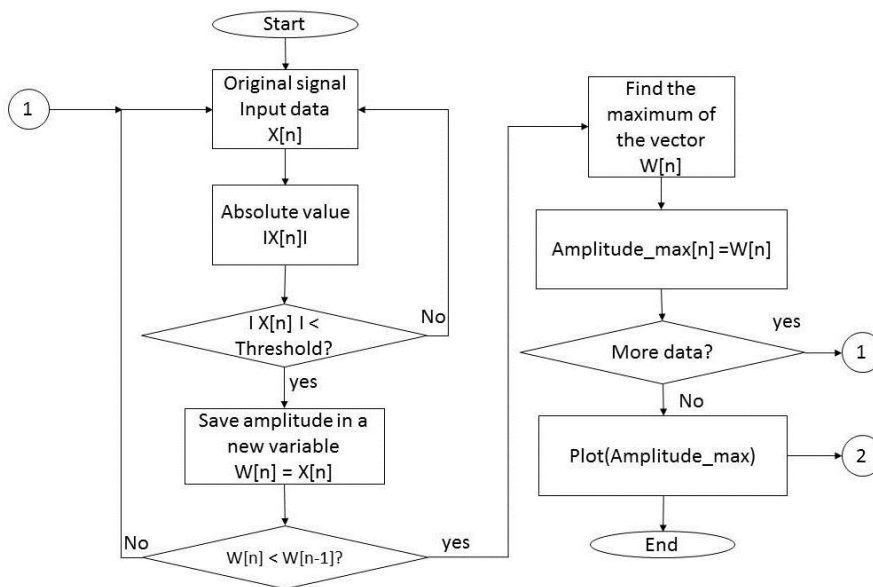


Figure 66: Block diagram for amplitude peaks detection. This algorithm was developed in MATLAB 2013.

The algorithm developed to find the current drop was:

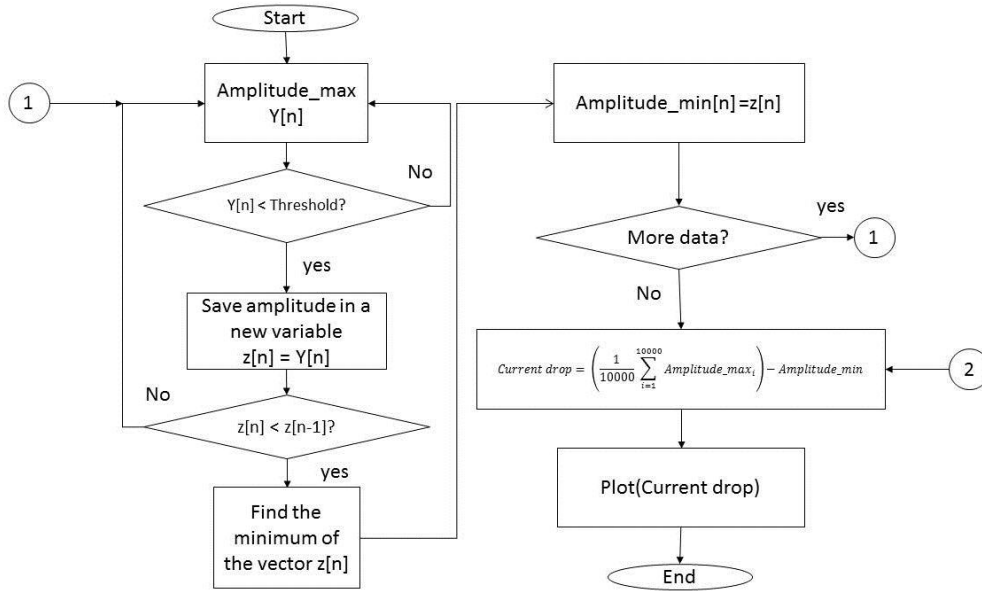


Figure 67: Block diagram for current drop detection. This algorithm was developed in MATLAB 2013.

7.4.2 Method 2

The following algorithm was implemented to detect the differential between reference signal “ $x_{nb[n]}$ ” and bubble signal “ $x_b[n]$ ”:

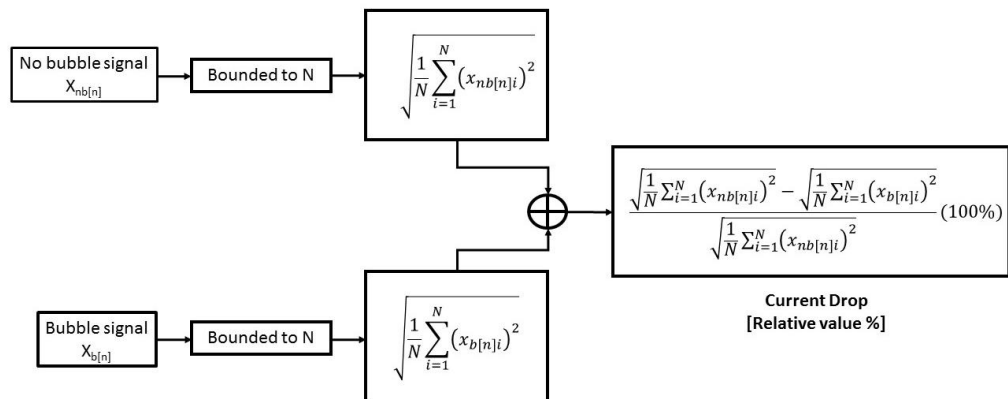


Figure 68: Algorithm to detect Current drop in relative value using "method 2"

7.5 K-mean Algorithm and STD predictor

```

%Universidad de Puerto Rico
%K-mean y STD predictor
%Elaborado por: Andrés Saavedra Ruiz
%2012-2015
clc
clear all
close all
%-----
% Datos con las características extraídas
%-----
A = xlsread('C:\Users\Andres Saavedra\Documents\MATLAB\work\Thesis\Algoritmos
finales\Data entrenamiento\Data_input_2_features.xlsx');
Bubble_size1 = A(:,4);%columna con los tamaños de burbuja en micro-metros
Curren_drop = A(:,3);%columna con las caídas en corriente en mili-amperios
MP1 = A(:,5);
MP2 = A(:,6);
%-----
% Clasificación
%-----
tic%Inicio conteo de tiempo de ejecución
% MP3 = A(:,7);
% X = [Bubble_size1 Curren_drop];% 2 features
X = [Bubble_size1 Curren_drop MP1 MP2];% 4 features
Grupos = 5;%Cantidad de clases
rng('default') % For reproducibility
opts = statset('Display','final');tic

```

```

[idx, ctrs] =
kmeans(X, Grupos, 'Distance', 'city', 'Replicates', 15, 'Options', opts);
toc%Finaliza conteo tiempo de ejecucion
plot(X(idx==1,1),X(idx==1,2), 'r.', 'MarkerSize', 12)
hold on
plot(X(idx==2,1),X(idx==2,2), 'b.', 'MarkerSize', 12)
plot(ctrs(:,1), ctrs(:,2), 'kx', 'MarkerSize', 12, 'LineWidth', 2)
plot(ctrs(:,1), ctrs(:,2), 'ko', 'MarkerSize', 12, 'LineWidth', 2)
legend('Cluster 1', 'Cluster 2', 'Centroids', 'Location', 'NW')
hold off
Resultado = [X, idx];
toc
gscatter(Bubble_size, X(:,2), idx, 'br', 'xo')%2 clases color, simbolo
% gscatter(Bubble_size, X(:,2), idx, 'brkgm', 'xov*+')%5 clases
% xlswrite('kmean_prediccion_4features_2clases', Resultado);%
% xlswrite('kmean_clasificacion_4features_2clases', Resultado);%
% -----
% Inicializacion de grupos STD predictor
% -----
for j=1:length(Curren_drop)-1
    bd = Resultado(:,1);
    cd = Resultado(:,2);
    if Resultado(j,6) == 1
        Grupo1(j) = [bd(j) cd(j)];
        Grupo1(j) = Resultado(j,2);
    else
        Grupo1(j) = 0;
    end
    if Resultado(j,6) == 2
        Grupo2(j) = Resultado(j,2);
    else
        Grupo2(j) = 0;
    end
end
% -----
% Decision: adiccion de nuevo sample de corriente a los grupos ya
% clasificados, determina cual presenta menor desviacion estandar,
% prediciendo a cual intervalo de tamaños de burbuja pertenece esa caida de
% corriente.
% -----
for l=1:length(Curren_drop)

Nuevo_dato = Curren_drop(l);
rms1 = std(Grupo1); Grupo1_1 = Grupo1;
Grupo1_1(end+1) = Nuevo_dato;
rms1_1 = std(Grupo1_1);
error1 = abs(rms1-rms1_1);

rms2 = std(Grupo2); Grupo2_2 = Grupo2;
Grupo2_2(end+1) = Nuevo_dato;
rms2_2 = std(Grupo2_2);
error2 = abs(rms2-rms2_2);

```

```

if error1 > error2
    salidapredictor(1) = 1;
    % display('Burbuja mayor a 500 um')
else
    % display('Burbuja menor a 500um')
    salidapredictor(1) = 0;
end
end
end

```

7.6 SVM Algorithm

The SVM function in MATLAB, for more than 2 classes, cannot be implemented. Thus, two algorithms were developed. The first shown below, it detects two bubble sizes:

```

%Universidad de Puerto Rico
%SVM predictor solo para dos clases
%Elaborado por: Andrés Saavedra Ruiz
%2012-2015
close all
clear all
clc
% -----
% Definicion de variables
% -----
A = xlsread('C:\Users\Andres Saavedra\Documents\MATLAB\work\Thesis\Algoritmos
finales\Data entrenamiento\Data_input_3_features.xlsx');
Current_drop = A(:,3);
MP1 = A(:,5);
MP2 = A(:,6);
X = [Current_drop];
X = [Current_drop MP1 MP2]
XTest = Current_drop;
Y = A(:,7);
% -----
% Aplicacion de SVM
% -----
tic
CVSVMModel = fitcsvm(X,Y)
[label,score] = predict(CVSVMModel,XTest);toc
Resultado = [XTest label];
% xlswrite('svm_prediccion_1feature_2classes',Resultado);
% xlswrite('svm_prediccion_3feature_2classes',Resultado);

```

In order to determine 5 classes, the next algorithm with one vs all methodology, was implemented:

```

%Universidad de Puerto Rico
%SVM predictor mas de dos clases
% Metodologia: 1 contra todos
%Elaborado por: Andrés Saavedra Ruiz
%2012-2015
close all
clear all
clc
% -----
% Definicion de variables
% -----
A = xlsread('C:\Users\Andres Saavedra\Documents\MATLAB\work\Thesis\Algoritmos
finales\Data entrenamiento\Data_input_3_features.xlsx');
Current_drop = A(:,3);
MP1 = A(:,5);
MP2 = A(:,6);
X = [Current_drop];
Y = A(:,7);
XTest = Current_drop;
% -----
% SVM multi clase, utilizando la funcion multisvm
% Funcion desarrollada por Anand Mishra 2015 obtenida como solucion por
% medio de Mathworks.com
% -----
tic
results = multisvm(TrainingSet, GroupTrain, TestSet);
toc
% xlswrite('svm_prediccion_1feature_5class',Resultado);
% xlswrite('svm_prediccion_3feature_5class',Resultado);

```

7.7 Neural Network Algorithm

```

%Universidad de Puerto Rico
%SVM predictor mas de dos clases
% Metodologia: 1 contra todos
%Elaborado por: Andrés Saavedra Ruiz
%2012-2015
close all
clear all
clc
A = xlsread('C:\Users\Andres Saavedra\Documents\MATLAB\work\Thesis\Algoritmos
finales\Data entrenamiento\Data_input_3_features.xlsx');
Bubble_size = A(:,2);
Current_drop = A(:,3);
MP1 = A(:,5);
MP2 = A(:,6);
subg1 = A(:,10);subg2 = A(:,11);subg3 = A(:,12);subg4 = A(:,13);subg5 =
A(:,14);
group = [subg1 subg2 subg3 subg4 subg5];
% x = [Current_drop MP1 MP2]; 3 Features

```

```

x = Current_drop;%1 feature
x = x';
t = group';
tic
% Create a Pattern Recognition Network
hiddenLayerSize = 6;
net = patternnet(hiddenLayerSize);
% Setup Division of Data for Training, Validation, Testing
net.divideParam.trainRatio = 70/100;
net.divideParam.valRatio = 15/100;
net.divideParam.testRatio = 15/100;
% Train the Network
[net,tr] = train(net,x,t);
% Test the Network
y = net(x);%Resultado de las redes al probarlo con toda la data de entrada
e = gsubtract(t,y);
tind = vec2ind(t);
yind = vec2ind(y);
percentErrors = sum(tind ~= yind)/numel(tind);
performance = perform(net,t,y);
toc
figure, plotconfusion(t,y)
% xlswrite('NN_prediccion_5clases_3features',y');

```

7.8 Rate of convergence

The "TASKLIST" command was used to detect the processes used by the computer constantly. The next table shows the running process in the computer when prediction algorithm was computed.

Image Name	CPU Process	Session Name	Session#	Mem Usage
System Idle Process	0	Services	0	24 K
System	4	Services	0	3,580 K
smss.exe	500	Services	0	1,384 K
csrss.exe	656	Services	0	6,696 K
wininit.exe	792	Services	0	5,188 K
csrss.exe	812	Console	1	12,724 K
services.exe	848	Services	0	11,968 K
lsass.exe	876	Services	0	14,640 K
lsm.exe	884	Services	0	4,964 K
winlogon.exe	972	Console	1	8,692 K
svchost.exe	380	Services	0	12,216 K
nvsvsc.exe	464	Services	0	8,632 K
	114			

nvSCPAPISvr.exe	524	Services	0	6,136 K
svchost.exe	700	Services	0	11,420 K
svchost.exe	804	Services	0	22,612 K
svchost.exe	1036	Services	0	161,904 K
svchost.exe	1076	Services	0	44,300 K
svchost.exe	1200	Services	0	13,768 K
svchost.exe	1364	Services	0	20,224 K
NvXDSSync.exe	1428	Console	1	22,724 K
nvsvcs.exe	1440	Console	1	15,888 K
AvastSvc.exe	1640	Services	0	41,412 K
wlanext.exe	1648	Services	0	19,828 K
conhost.exe	1656	Services	0	3,552 K
spoolsv.exe	1832	Services	0	18,156 K
svchost.exe	1868	Services	0	14,568 K
armsvc.exe	1956	Services	0	4,192 K
AERTSr64.exe	1980	Services	0	3,444 K
AgentHost.Service.exe	2004	Services	0	17,500 K
AppleMobileDeviceService.exe	2388	Services	0	9,856 K
Agent.AgentHost.exe	2408	Services	0	27,460 K
devmonsrv.exe	2540	Services	0	7,088 K
svchost.exe	2576	Services	0	5,852 K
EvtEng.exe	2652	Services	0	17,352 K
hasplms.exe	2704	Services	0	21,708 K
lkads.exe	2876	Services	0	9,100 K
nidmsrv.exe	2916	Services	0	9,496 K
SystemWebServer.exe	2960	Services	0	10,616 K
rndlresolversvc.exe	3024	Services	0	4,204 K
RegSvc.exe	2136	Services	0	9,088 K
SftService.exe	2696	Services	0	10,032 K
taskhost.exe	2712	Console	1	9,920 K
svchost.exe	3124	Services	0	6,840 K
dwm.exe	3200	Console	1	10,624 K
SupportAssistAgent.exe	3208	Services	0	42,360 K
explorer.exe	3232	Console	1	93,368 K
Toaster.exe	3456	Console	1	52,056 K
TeamViewer_Service.exe	4080	Services	0	14,436 K
WLIDSVC.EXE	2284	Services	0	12,532 K
ZeroConfigService.exe	4128	Services	0	17,840 K
RtkNGUI64.exe	4324	Console	1	13,276 K
obexsrv.exe	4384	Services	0	7,512 K
nvtray.exe	4400	Console	1	35,472 K
hkcmd.exe	4436	Console	1	8,828 K

igfxpers.exe	4452	Console	1	12,804 K
lkcidl.exe	4572	Services	0	9,812 K
Apoint.exe	4632	Console	1	12,896 K
rundll32.exe	4724	Console	1	11,180 K
quickset.exe	4924	Console	1	14,560 K
WLIDSVCM.EXE	5056	Services	0	4,756 K
lktsrv.exe	4424	Services	0	9,716 K
unsecapp.exe	4660	Services	0	6,788 K
ApplicationWebServer.exe	4824	Services	0	9,108 K
WmiPrvSE.exe	1348	Services	0	14,644 K
nmsrv.exe	5424	Services	0	8,492 K
WmiPrvSE.exe	5956	Services	0	27,532 K
GoogleUpdate.exe	5488	Console	1	528 K
ISUSPM.exe	5548	Console	1	7,964 K
SearchIndexer.exe	3108	Services	0	59,772 K
WebcamDell2.exe	6192	Console	1	9,836 K
ApMsgFwd.exe	6388	Console	1	8,616 K
mediasrv.exe	6456	Services	0	8,600 K
AvastVBoxSVC.exe	6604	Services	0	12,276 K
btplayerctrl.exe	6684	Console	1	7,004 K
ApntEx.exe	6748	Console	1	8,120 K
hidfind.exe	6764	Console	1	7,192 K
conhost.exe	6824	Console	1	5,668 K
SweetPacksUpdateManager.exe	6856	Console	1	10,280 K
nmctxth.exe	6892	Console	1	15,276 K
realsched.exe	7036	Console	1	412 K
AgentHost.UI.exe	7052	Console	1	42,000 K
svchost.exe	7096	Services	0	6,632 K
svchost.exe	6320	Services	0	45,132 K
avastui.exe	1380	Console	1	25,660 K
ngservice.exe	6536	Services	0	4,592 K
unsecapp.exe	3652	Console	1	8,692 K
SearchProtocolHost.exe	5596	Services	0	8,984 K
BTHSAmpPalService.exe	3112	Services	0	6,048 K
BTHSSecurityMgr.exe	2804	Services	0	10,652 K
DellDataVaultWiz.exe	5552	Services	0	12,152 K
MATLAB.exe	6172	Console	1	465,244 K
LMS.exe	6408	Services	0	5,272 K
NASvc.exe	6704	Services	0	6,928 K
svchost.exe	6300	Services	0	23,748 K
wmpnetwk.exe	6156	Services	0	9,960 K
DellDataVault.exe	5876	Services	0	11,740 K

UNS.exe	4184	Services	0	8,068 K
WmiApSrv.exe	1132	Services	0	7,636 K
cmd.exe	6888	Console	1	4,488 K
conhost.exe	4244	Console	1	6,720 K
SearchFilterHost.exe	4300	Services	0	6,664 K
tasklist.exe	7956	Console	1	8,860 K

Considering the hardware devices currently in the order to make the portable system, you must consider the following:

Algorithm	Features	Classes	Iterations	Time of convergence [sec]			
				PC	PIC	DSP	FPGA
K-mean	1	2	4	0.14	449.1	2.0	18.0
SVM	1	2	14	1.20	3849.0	17.5	154.0
NN	1	2	22	1.76	5645.2	25.7	225.0
K-mean	1	5	5	0.16	513.2	2.3	20.5
SVM	1	5	29	1.84	5901.8	26.8	236.1
NN	1	5	19	1.78	5709.4	26.0	228.4
K-mean	3	2	8	0.15	481.1	2.2	19.2
SVM	3	2	21	1.34	4298.1	19.5	171.9
NN	3	2	34	1.83	5869.7	26.7	234.8
K-mean	3	5	7	0.16	513.2	2.3	20.5
SVM	3	5	27	1.84	5901.8	26.8	236.1
NN	3	5	133	2.03	6511.2	29.6	260.4

Table 23: Comparison of the time of convergence to classifiers in different hardware devices.

Table 23 used the following technical specifications: PIC “18F452” with 40 MIPS (Microchip, 2002). DSP “TMS320DM647” with 8800 MIPS (TI, 2012). FPGA Stratix 10 with 1000 MIPS (Altera, 2015).